Synthesis of Yttrium Iron Garnet based ferrofluids and study of their colloidal, magnetic and optical properties

Simon P. Gihozo (7548508)

Master's thesis, Nanomaterials Science program

May 31, 2024

Supervisors: Dr. Alex M. van Silfhout
Dr. Ben H. Erné

Examiner: Dr. Andrei V. Petukhov

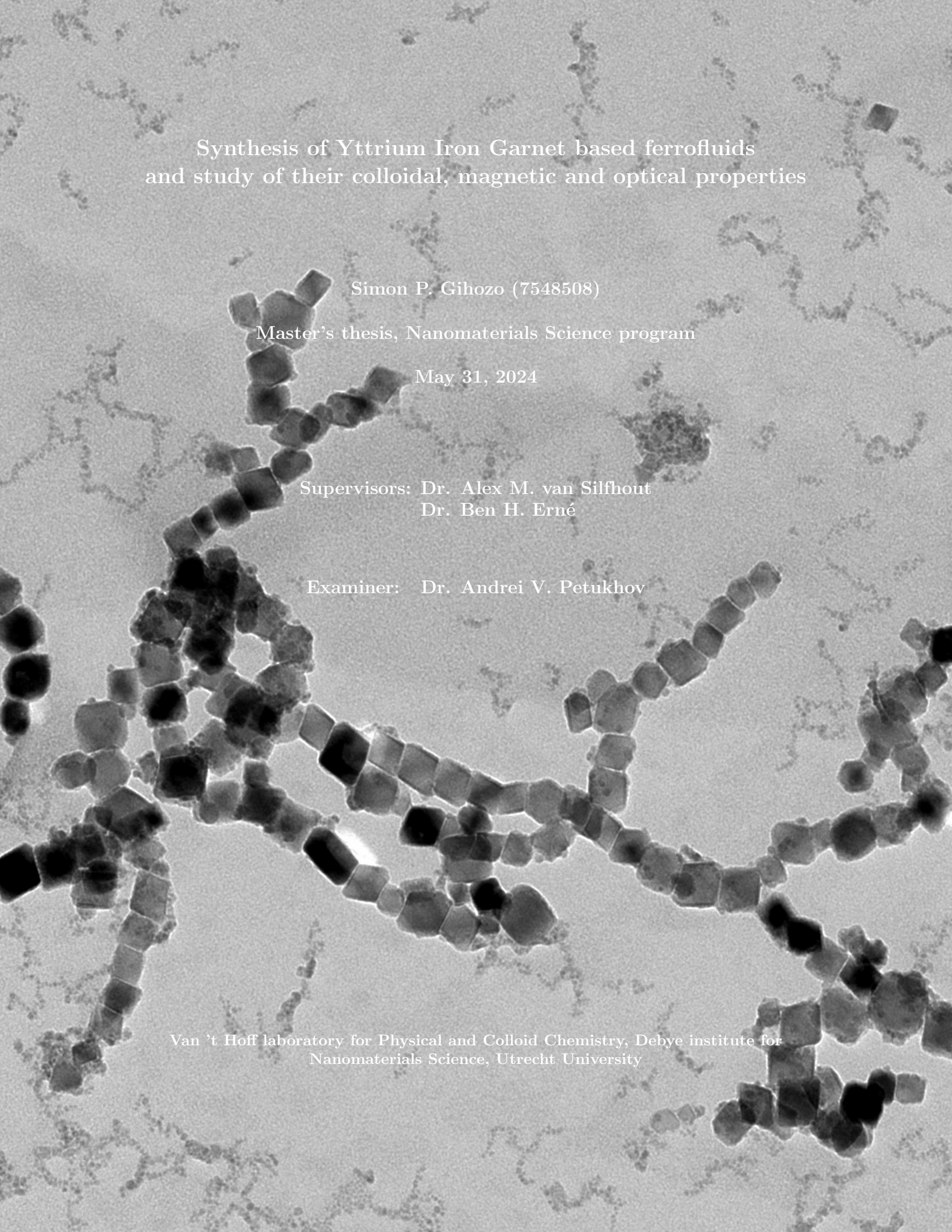

Van 't Hoff laboratory for Physical and Colloid Chemistry, Debye institute for Nanomaterials Science, Utrecht University

Synthesis of Yttrium Iron Garnet based ferrofluids and study of their colloidal, magnetic and optical properties

Simon P. Gihozo (7548508)

Master's thesis, Nanomaterials Science program

May 31, 2024

Supervisors: Dr. Alex M. van Silfhout
Dr. Ben H. Erné

Examiner: Dr. Andrei V. Petukhov

Van 't Hoff laboratory for Physical and Colloid Chemistry, Debye institute for Nanomaterials Science, Utrecht University

Abstract

Ferrofluids are colloidal systems of superparamagnetic nanoparticles suspended in a carrier liquid and coated with a stabilizing agent. The presence of an external magnetic field gradient affects the direction of the magnetic nanoparticles. Ferrofluids are applied for the separation of waste plastics via magnetic density separation but the black appearance of the ferrofluids makes it difficult to observe the processes due to the strong optical absorption from UV to NIR region. Ferrofluids based on Yttrium Iron Garnet nanoparticles (YIG-NPs) were synthesized due to the bulk properties of YIG considered to be lower in optical absorbance than magnetite and maghemite, where it is expected YIG ferrofluids to be more transparent than conventional ferrofluids based on magnetite and maghemite. Maghemite nanoparticles were formed from magnetite nanoparticles by refluxing in acidic environment to promote the ion exchange of Fe^{2+} and Fe^{3+}. The stabilization part to obtain stable maghemite nanoparticles in a carrier liquid was not applicable to obtain stable YIG-NPs and stable magnetite nanoparticles in a carrier liquid. Magnetite nanoparticles were synthesized by co-precipitation and coated by adsorbing citrate molecules as a result of transferring the magnetite nanoparticles in acidic environment. YIG dispersions were formed via solvothermal synthesis by heterogeneous seeded growth of YIG-NPs on Yttrium Aluminium Garnet (YAG) seeds. The coating was executed with oleic acid as the stabilizing agent dispersed in cyclohexane. The coating in the oil phase showed improvement in the ferrofluid behaviour, flow of magnetic dispersion towards higher magnetic field gradient, compared to the stabilization method of maghemite and magnetite nanoparticles in the water phase.
The ferrofluids were analyzed to study the colloidal, magnetic and optical properties. The colloidal properties were observed from DLS and TEM measurements. Magnetic sedimentation experiments were done to study the colloidal properties in magnetic field. Magnetometry was applied to study the magnetic properties. For the optical properties, UV-Vis measurements were done to observe the wavelength-dependent optical density profiles. Size control of the YIG-NPs was not achieved due to the inconsistency of the formed YAG seeds. YIG-on-YAG nanoparticles were formed but showed aggregation. Optical transmission of the YIG ferrofluids was affected by the optical scattering of the aggregates. The aggregates were detected by DLS and magnetic sedimentation. The characterization techniques indicated that the presence of aggregates affected the ferrofluid stability and explained the rapid sedimentation of the magnetic colloids.

Contents

1 Introduction

Ferrofluids behave like liquid magnets in external magnetic field.[1] An application to focus on is the separation of waste plastics via magnetic density separation. The combination of magnetic field and ferrofluid is used to continuously separate waste plastics by gravity and buoyancy forces that act on the plastics.[2] By applying a magnetic field, the magnetic field gradient affects the direction of the plastics towards decreasing field and separates the plastic by the density difference between the plastic and the liquid. The process is illustrated in Figure 1. In practice, the black appearance of the ferrofluids makes it difficult to observe the magnetic density separation (MDS) process macroscopically since ferrofluids strongly affect the polarization of transmitted light and strongly absorb visible light.

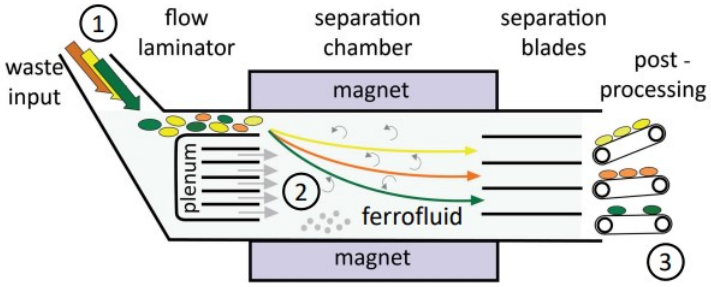

Figure 1: Schematic representation of an industrial MDS setup. (1) Nonmagnetic particles are brought into a flow of ferrofluid, after which the mix flows into a separation chamber (2), where particles flow towards an equilibrium height which depends on their density. At the end of the separation chamber, particles are collected in a number of fractions (3) and removed from the liquid, which is reused in a continuous process. Figure copied from Ref.[2].

These limitations of the ferrofluids are addressed by creating a novel type of ferrofluids based on Yttrium Iron Garnet nanoparticles (YIG-NPs). Bulk YIG has a lower optical absorbance than magnetite and maghemite, where it was expected YIG ferrofluids to be more transparent than conventional ferrofluids based on magnetite and maghemite.[3, 4, 5] A single-step synthesis of YIG-NPs is difficult due to the high required activation energy of the homogeneous nucleation. Previous research has shown that seed crystals of Yttrium Aluminum Garnet (YAG) can be used as substrate to grow YIG-NPs.[6] Seeded growth is a method of depositing crystalline layers on a mono-crystalline substrate to obtain YIG-NPs.
Colloidal dispersions of YIG-NPs were prepared by solvothermal reactions in a stainless-steel autoclave and compared with conventional ferrofluids. Colloidal stability was necessary, so that the dispersions behaved like liquid magnets instead of losing stability in an external field. Besides chemical synthesis and colloidal stabilization of ferrofluids, the optical properties of the ferrofluids were studied. Characterization techniques to study the colloidal properties included magnetometry, magnetic sedimentation, DLS, and TEM imaging. For the optical properties, UV-Vis spectroscopy was done to observe the wavelength-dependent extinction coefficient of ferrofluids over a broad wavelength range. The objective was therefore to synthesize YIG, maghemite and magnetite ferrofluids and study how the colloidal, magnetic and optical properties differ from each other.

2 Theory

In this section, the magnetism of a material is explained by classifying different types of magnetic behaviour. These types are listed as diamagnetism, paramagenetism, ferromagnetism, antiferromagnetism and ferrimagnetism. The knowledge is then used to explain compounds maghemite, magnetite and Yttrium Iron Garnet (YIG). Differences between the materials are investigated in their magnetic, colloidal and optical properties. The behaviour of a ferrofluid is explained due to the superparamagnetism. The synthesis of the magnetic materials is discussed by considering the main and parameters for comprehending the concept to form a ferrofluid.

2.1 Concept of magnetism

Magnetism can be defined as a physical phenomenon that is mediated by magnetic fields.[7, 8] The source of magnetism however can be caused by the movement of charged particles such as electrons or ions.[7, 8] The movement of the charged particles creates a magnetic field that can interact with other charged particles and their magnetic fields. The interactions between the charged particles generates electromagnetic induction and forms the basis of electrical devices.
[7, 8]
The angular momentum of elementary particles is an important contribution to magnetism and determines on the intrinsic magnetic properties of the electrons and the way these charged particles interact with the nuclei of the atoms.[8] Two main distinctions can be made when considering the electron as the main source of magnetic moment.

1. Orbital motion of the electron around the nucleus.
2. The spin of the electron.

To clarify magnetism, an atomic model is illustrated in Figure 2. The model represents a model of atoms that consists of a positively charged nucleus at its center, composed of protons and neutrons, surrounded by negatively charged electrons. The electrons move in circular orbits around the nucleus. The orbital motion of the electrons causes the circulating electron currents from which the magnetic moment arises. The different types of magnetism can be explained by the spin moment of the elementary particles since the spin is a form of intrinsic angular momentum that electrons particles possess.[8] Since an electron only has discrete values of +1/2 and -1/2, the spin is quantized. The sign of the spin can be denoted as 'spin-up' and 'spin down', respectively and indicates the opposite orientations of the magnetic moment.
The spin affects the intrinsic magnetic moment associated with the particle due to the formed magnetic field of the electron. The electron possesses a tiny magnetic dipole moment and has therefore a spin magnetic moment.[8]

The contribution of the spin momentum and orbital momentum forms the spin-orbit coupling to generate a total electronic angular momentum that generates the magnetic moment.[8] When a particle with spin is placed in a magnetic field, its magnetic moment tends to align with the field direction. In materials with heavy elements or strong spin–orbit coupling, the modification of magnetic moments can lead to various magnetic phenomena.[8] The strong spin-orbit coupling influences the magnetic properties, such as the distinction between types of materials when applying a magnetic field with the result that magnetism is induced by the attractive or repulsive forces of the applied magnetic field. These forces indicate the magnetic behaviour of materials in response to an external magnetic field and therefore the magnetism of the material.

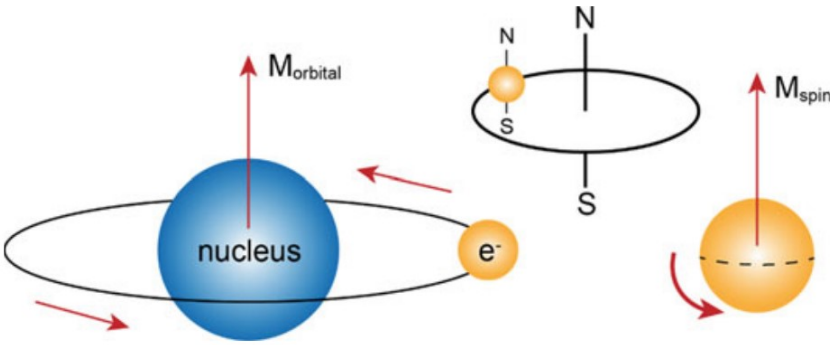

Figure 2: Atomic model of orbital and spin moment. Figure copied from Ref.[8].

2.1.1 Diamagnetism

Materials such as glass, water and plastic are known for their diamagnetism due to the absence of a net magnetic moment. The reason for the non-magnetic behaviour is the revolving of the electrons in the orbits of atoms.[9, 10] For magnetism to occur, atoms need to represent unpaired spins, i.e., the unpaired electrons. In the case of diamagnetism, the atoms do not have unpaired spins. In Figure 3, the atoms are illustrated without the presence of and external magnetic field, H. When an external magnetic field is applied, the material opposes the external magnetic field. This phenomenon is denoted as red arrows in opposite direction to the external magnetic field to indicate that the atoms and therefore the material do not show any form of magnetism.

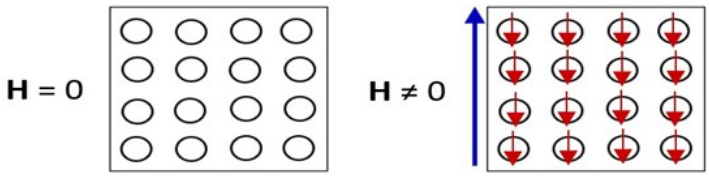

Figure 3: Diamagnetic arrangement of atomic spins without (left) and with (right) the presence of an external magnetic field, H. Figure adapted from Ref.[10].

2.1.2 Paramagnetism

Materials such as copper, aluminium and iron(III) chloride are known for their paramagnetism. When the net magnetic moment of a material is not equal to zero, the material can be denoted as paramagnetism. However, the material needs a stimulant to induce a magnetic moment due to the randomly oriented unpaired spins without the present of an external magnetic field as presented in Figure 4. The stimulant is the external magnetic field, H, that reacts with the magnetic dipole moments of the atoms. The magnetic dipoles of the atoms are weakly aligned with an external field so that the total magnetic dipole moment is enhanced with the result a magnetic moment of the material.[9, 11]

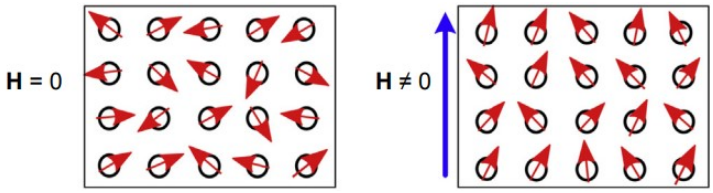

Figure 4: Paramagnetic arrangement of atomic spins without (left) and with (right) the presence of an external magnetic field, H. Figure adapted from Ref.[10].

2.1.3 Ferromagnetism

The type of magnetism covered in this chapter is ferromagnetism due to the already aligned magnetic dipole moments of the unpaired spins without an external magnetic field. However, the net magnetic moment is zero when observing the material macroscopically.[10] The zero magnetism on a macroscopic scale is explained by the atomic model of a ferromagnetic material in Figure 5. The Figure denotes the spins of the unpaired electrons but by interpreting the model, it can be observed that all spins do not indicate the same direction. The spins align when involving magnetic domains. The magnetic domains are the regions where the spins align in the same direction and therefore makes the domain exhibit a magnetic moment. When a ferromagnetic material is subjected to an external magnetic field, the spins of the atoms start to align themselves in the field direction and at full saturation of the magnetic field, almost all the magnetic domains are pointed in the direction of the magnetic field.[10, 11] Examples of ferromagnetic materials are metallic iron, nickel and neodymium.

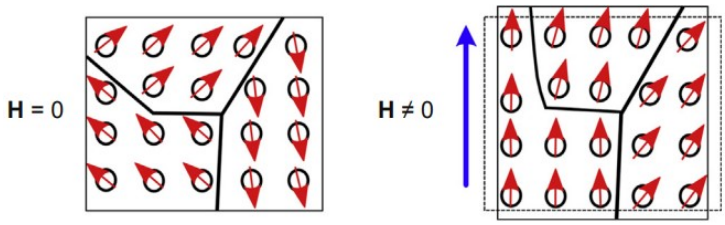

Figure 5: Ferromagnetic arrangement of atomic spins without (left) and with (right) the presence of an external magnetic field, H. Figure adapted from Ref.[10].

2.1.4 Antiferromagnetism

When comparing ferromagnetism with antiferromagnetism, the features of exhibiting magnetic domains and the arising of a strong magnetic moment upon applied magnetic field are comparable. Although, the difference between the two forms of magnetism can be explained by considering an ionic material consist of cations and anions. For better understanding, the anions are excluded. The magnetic moments of the cations are similar but the spins of the electrons are antiparallel, i.e., the spins are ordered but in a way that the spins of neighboring atoms are in opposite directions.[10] This appearance makes an antiferromagnetic material show paramagnetism when considering an additional parameter: the temperature. The permanent dipole moment of the atoms is zero when the temperature is below the critical value.[9, 10] This critical value is indicated as the Néel temperature, T_N. When the Néel temperature is exceeded, the spins in the atoms cant. By also applying a magnetic field, a weak alignment of the spins is obtained. As a result of the weak alignment, the antiferromagnetism resembles that of paramagnetism as shown in Figure 6. Examples of antiferromagnetic materials are hematite (α-Fe_2O_3), chromium and manganese(II) oxide.

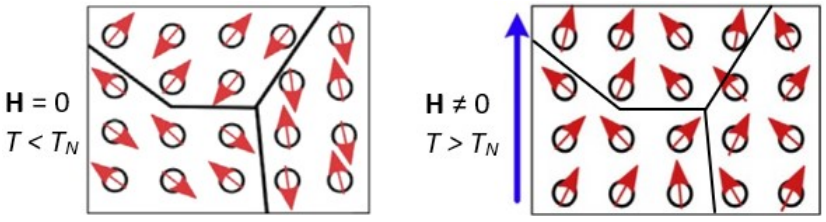

Figure 6: Antiferromagnetic arrangement of atomic spins without (left) and with (right) the presence of an external magnetic field, H, and with the consideration of the Néel temperature, T_N. Figure adapted from Ref.[10].

2.1.5 Ferrimagnetism

Materials consisting of iron-metal oxide are known for their ferrimagnetism and can be denoted as the so called ferrites.[10] Examples of ferrimagnetic materials are maghemite, magnetite and yttrium iron garnet.

The magnetic behavior of ferrimagnetic materials is similar to that of ferromagnetic materials, however, a distinction can be made between the types of magnetic materials on the atomic scale, as illustrated in Figure 7. The atomic model of a ferrimagnetic material shows that the dipole moments are organized in domains but the dipole moments are a mixture of unequal antiparallel aligned moments. Since the dipole moments are antiparallel, the magnetic moment of the material should be equal to zero but the difference in magnitude of the dipole moments makes the antiparallel moments not cancel each other and results in a net magnetic moment. This effect remains strongly magnetic, albeit less than a ferromagnetic material.[9] Another factor to consider is the temperature as discussed for a ferromagnetic material but in this case the critical temperature is denoted as the Curie temperature, T_C. The Curie temperature is the temperature at which the ferro- or ferrimagnetic material material undergoes the phase transition from a low-temperature ferro- or ferrimagnetic phase to a high-temperature paramagnetic phase upon heating.[12] When exceeding T_C, the ferroelectricity and piezoelectricity disappear with the result of paramagnetic behaviour of the material like with the Néel temperature.[12] The difference between the Néel temperature and the Curie temperature is the effect of the ferro- or ferrimagnetic material when cooling down below the critical value. When $T_{material} < T_N$, the type of magnetism remains, i.e., the material keeps the ferro- or ferrimagnetism. This phenomenon does not follow when the Curie temperature is brought to attention. When the temperature of the ferro- or ferrimagnetic material exceeds the Curie temperature ($T_{material} > T_C$), the magnetic material loses its permanent magnetic moment and is therefore not capable to obtain ferro- or ferrimagnetism.

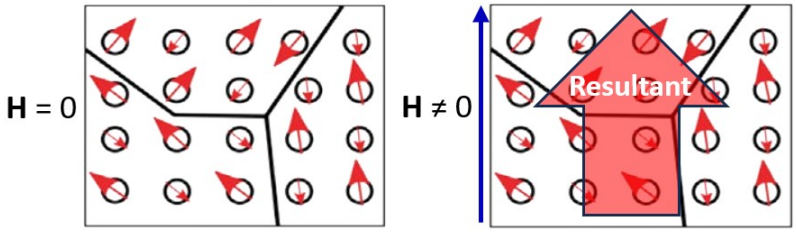

Figure 7: Ferrimagnetic arrangement of atomic spins without (left) and with (right) the presence of an external magnetic field, H. Figure adapted from Ref.[10].

2.1.5.1 Maghemite and magnetite

Both maghemite and magnetite are ferrimagnetic material but the solids differ in their magnetic behaviour due to their differences physical properties. These differences start with their molecular formula. The molecular formula of maghemite is $\gamma - Fe_2O_3$, whereas magnetite has Fe_3O_4. Because of the different molecular formula, the crystallographic structures are different which are represented in Figure 8.

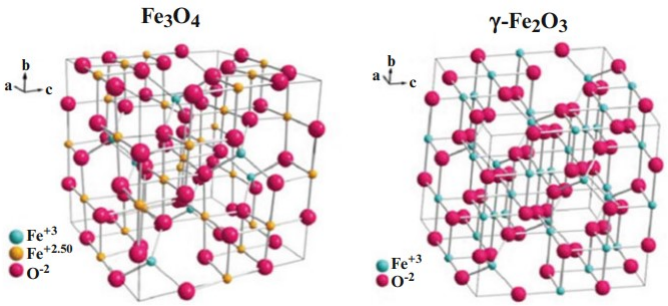

Figure 8: Crystal structure of maghemite and magnetite. Figure copied from Ref.[13].

In magnetite, the iron ions are located into the tetrahedral (T_d) and octahedral (O_h) sites of the face-centered cubic structure according to
($[Fe^{3+}]_{T_d}[Fe^{3+} + Fe^{2+}]_{O_h}O_4$) and contains 32 O^{2-} ions.[13] One half of the octahedral positions are filled with eight Fe^{3+} ions and eight Fe^{2+} ions.[13] In addition, eight of the tetrahedral positions are filled with Fe^{3+} ions.[13] Maghemite is similar to magnetite in its crystallographic structure. In the case of maghemite, the unit cell consists of 21 1/3 Fe^{3+} ions and 32 O^{2-} ions and forms a comparable crystalline structure as magnetite, but maghemite has a different crystal lattice of ($[Fe^{3+}]_{T_d}[Fe^{3+}_{5/3}X_{1/3}]_{O_h}O_4$ where X denotes a cationic vacancy).[13]

2.1.5.2 Yttrium Iron Garnet

Yttrium iron garnet (YIG) is a ferrite material and possess a cubic crystal structure with general garnet formula $A_3B_5O_{12}$ and specific formula $Y_3Fe_5O_{12}$.[14] The crystallographic structure of YIG is shown in Figure 9. The two metallic ions (Y^{3+} and Fe^{3+}) present in the sites are both trivalent and make YIG suitable for magnetic studies.

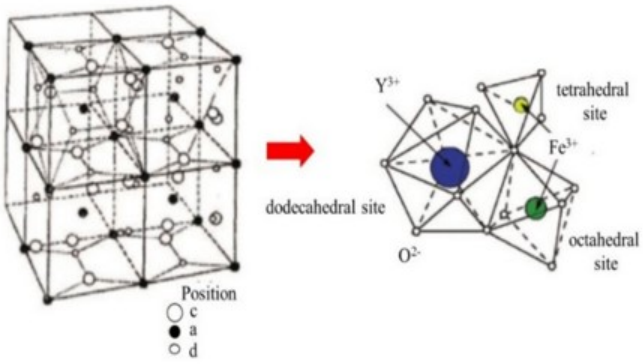

Figure 9: Crystal structure of Yttrium iron garnet. Figure copied from Ref.[15].

There are three sub-lattices in the garnet structure:

- The dodecahedral (c) site occupied by the three yttrium ions.
- The octahedral (a) site occupied by two iron ions.
- The tetrahedral (d) site occupied by three iron ions.

The structure of YIG and the position of the ions are explained by considering the mechanism. If the inorganic compounds iron oxide (Fe_2O_3) and yttrium oxide (Y_2O_3) are considered only and the conversion is 100%, the overall reaction to form YIG takes place at high temperature and pressure as follows:[16]

$$5\,Fe_2O_3(s) + 3\,Y_2O_3(s) \longrightarrow 2\,Y_3Fe_5O_{12}(s)$$

If the conversion is not 100%, secondary phases of Yttrium orthoferrite, YIP, ($YFeO_3$) appear. YIG is formed with an intermediate step:[16]

$$Fe_2O_3(s) + Y_2O_3(s) \longrightarrow 2\,YFeO_3(s)$$

$$Fe_2O_3(s) + 3\,YFeO_3(s) \longrightarrow 2\,Y_3Fe_5O_{12}(s)$$

The formed secondary phases suppress the formation of YIG crystals and therefore must be encountered. This can be achieved by the addition of excess of iron oxide. The excess of iron oxide reacts with the secondary phases to form YIG crystals and hematite. However, the amount of excess is determinative. According to the research, the addition of 8-10 wt% of excess Fe_2O_3 is sufficient to reduce the formation of $YFeO_3$ and increase the yield of the desired crystals.[16] Further increasing of excess Fe_2O_3 consumes YIP from which single phase YIG can be obtained. Luckily, time is also a crucial factor for the completion of single phase YIG as represented in Figure 10. The residence time of the reactants in a heat insulating and pressure resistant system shows the presence of the reactants, YIP and YIG. The Figure shows rapid formation of YIP (before 30 minutes) reaching a formation where the YIG phase covers nearly 60 % of the YIG product. After 30 minutes, the percentage of YIP gradually decreases and the YIG starts to form since the YIP is consumed by the reactants.

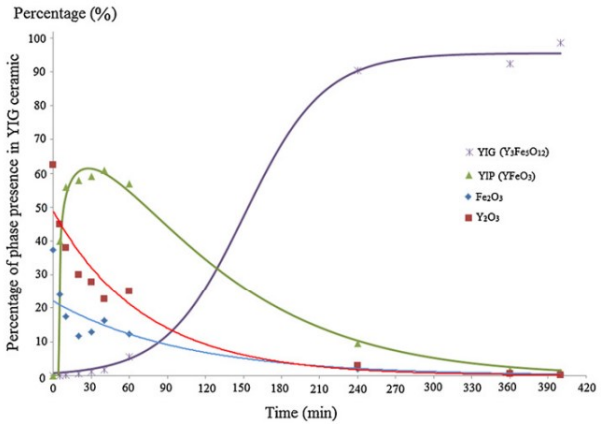

Figure 10: The percentage of phases present in YIG ceramics sintered at 1420 °C over time. Figure copied from Ref.[16].

The solid-state reactions depend on the mobility of the ions O^{2-}, Y^{3+}, and Fe^{3+}.[16] The ionic radius of the anion is larger and therefore has a lower mobility than the cations. This indicates the transport of cations through spaces that connects the- anions. Using the stoichiometry of the yttrium garnet structure, the diffusion requires three Y^{3+} and five Fe^{3+}.[16] For the iron oxide, cations Fe^{2+} and Fe^{3+} is formed according to the equation below.

$$3\,Fe_2O_3(s) \longrightarrow 2\,Fe^{2+}(s) + 2\,Fe_2^{3+}O_4(s) + \tfrac{1}{2}\,O_2(s)$$

The mobility of Fe^{3+} is higher in comparison with Y^{3+} and Fe^{2+}. This leads to the complete filling of the octahedral and tetrahedral interstices of O^{2-} by Fe^{3+}.[16] As a results, Y^{3+} fills the dodecahedral sites due to the higher ionic radius and therefore lower mobility than Fe^{3+} from which the crystal structure of YIG is obtained.

2.2 Magnetism and motion of ferrofluids

Ferrofluids are liquid dispersions of superparamagnetic colloidal particles, dispersions that combine properties of liquids and magnets.[2] Three types of magnetic colloidal particles can be mentioned:

(1) colloidal particles that incorporate paramagnetic ions.
(2) single-domain nanoparticles

(3) magnetic microbeads.

The focus for understanding magnetism of ferrofluids is on single-domain nanoparticles due to the interest for the ferrofluid behaviour of maghemite, magnetite, and YIG dispersion. The second type of magnetic dispersion is based on superparamagnetism and is a special feature of magnetism in comparison with the conventional types of magnetism discussed in the previous subsection. Superparamagnetism is a form of magnetism which appears in ferromagnetic or ferrimagnetic nanoparticles.[17] The principle lies in the size of the nanoparticles. In the previous subsection, atomic models were shown for a bulk material consisting of atoms that have their unpaired spins and because of the alignment experience a magnetic dipole moment in a certain direction. For ferromagnetic and ferrimagnetic materials, the atoms exhibit magnetic domains where the direction of the spins differ in each magnetic domain. Superparamagnetism arises when the magnetic dipole that corresponds to the single magnetic domain in a nanoparticle is free to rotate in an external magnetic field.[9, 17, 18] The magnetic dipole moment, m_d, is then given by,

$$m_d = V_{NP} \cdot m_b \tag{1}$$

where V_{NP} is the magnetic volume of the nanoparticle (m^3) and m_b is the bulk magnetization in Am^{-1} The nanoparticle dipoles react to an external field qualitatively in the same way as the dipolar atoms in a paramagnetic material, but the effect is stronger. This is because the dipole moment is no longer that of a single atom, but corresponds the number of atoms in the nanocrystal as shown in Figure 11.[9]

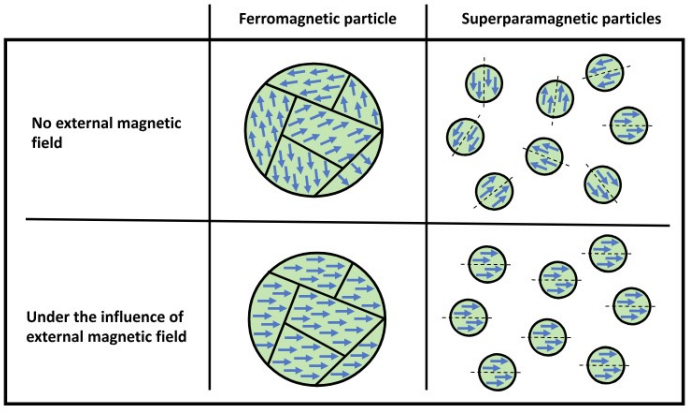

Figure 11: The appearance of superparamagnetic behaviour. Figure copied from Ref.[19].

The motion of ferrofluids can be induced by magnetophoresis. Magnetophoresis is the motion of magnetic-field-induced particles and takes place due to a gradient of the magnetic field.[9] If a magnetic field is the same in each direction, a magnetic particle will not displace by the external magnetic field because its magnetic energy is independent of position. This does not cause a magnetic driving force for motion. In a magnetic field gradient, however, the particle moves towards increasing field strength and the magnetic force on the particle is now due to the gradient of the magnetic field, **B**, in the direction of the dipole, **m**, by the following equation,[20]

$$F_{magnetic} = (\overrightarrow{m} \cdot \nabla)\overrightarrow{B} \tag{2}$$

or if we only consider the x direction,

$$F_{magnetic,x} = m_x \frac{dB_x}{dx} \tag{3}$$

In addition, the motion of ferrofluids in external magnetic fields can be discussed using the adjusted Bernoulli equation, with terms having units of energy density ($J \cdot m^{-3}$ = Pa)[21, 22]:

$$P + \frac{\rho v^2}{2} + \rho g h - \int_0^H M \, dH = C \tag{4}$$

P represents the hydrostatic pressure. The second term is the kinetic energy, with ρ and v as the mass density and velocity of the ferrofluid, respectively. The third term corresponds to the gravitational energy, with g and h as the acceleration due to normal gravity and the elevation, respectively. The last term denotes the amendment made by Rosensweig to account for the magnetic energy of ferrofluids.[21, 22] Adding the terms together yields the conservation energy that is represented with the constant C. When the total is not equal everywhere in the ferrofluid, the liquid flows from high to lower total energy per unit volume.

2.3 Ferrofluids and their colloidal stability

The colloidal stability of the ferrofluid can be observed with the naked eye as depicted in Figure 12.

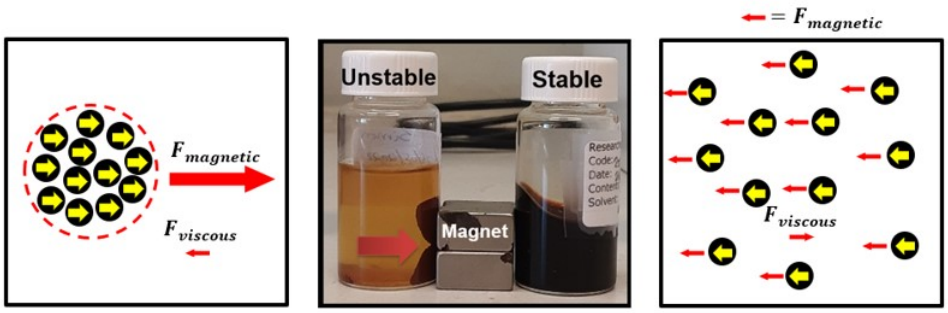

Figure 12: Colloidal stability of maghemite dispersion in the presence of an external field (neodymium magnet $\sim$ 0.5T) Figure adapted from Ref.[9].

For the magnetic dispersion that represents the unstable situation, the magnetic particles migrate to the magnet (red arrow) leaving the bulk solution motionless and therefore no ferrofluid behaviour is obtained. The ferrofluid behaviour does appear in the maghemite dispersion that represents the 'stable' situation since a flow of the dispersion towards the magnet is shown and therefore indicates a stable ferrofluid. This magnetophoretic phenomena of the magnetic fluid is the consequence of the separate magnetic nanoparticles that strongly affects the drag force of the bulk phase.[20, 23] The magnetic nanoparticles flow toward a magnet slowly with a magnetophoretic velocity in the order of 10^{-8} m/s. The slow migration causes the concentration of the magnetic nanoparticles to remain largely homogeneous for a long time. A ferrofluid behaviour is then observed on a macroscopic length scale. In addition, the colloidal stability can be explained by comparing the osmotic pressure of concentrated ferrofluids with diluted ferrofluids assuming that both ferrofluids have similar size distribution. The osmotic pressure, can then be expressed by Van 't Hoff law:

$$\Pi = \rho k_B T \tag{5}$$

- Π is the osmotic pressure (Pa).
- ρ is the number density of the particles (m^{-3}).

- k_B is the Boltzmann constant (JK^{-1}).
- T is the temperature (K).

Moreover, the diffusion is highlighted due to the relation between the Brownian motion and the viscous force according to the following equation,

$$D = \frac{k_B T}{6\pi\eta a_H} \tag{6}$$

- D is the diffusion coefficient ($m^2 s^{-1}$).
- η is the viscosity of the bulk ($Pa \cdot s$).
- k_B is the Boltzmann constant (JK^{-1}).
- T is the temperature (K).
- a_H is the hydrodynamic radius of the particles (m).

Combining the expressions yield,

$$\Pi = D \cdot \rho \cdot 6\pi\eta a_H \tag{7}$$

From the final expression can be confirmed that concentrated ferrofluids exert a high osmotic pressure due to the higher number density. The presence of a magnetic force causes migration of the particles from which an osmotic pressure gradient is established that counteracts magnetically induced motion, and the ferrofluid can remain stable and homogeneous. Diluted ferrofluids have a lower number density and results in an low osmotic pressure gradient. Diffusion of the magnetic particles in opposite direction of the magnetic migration is prevented due to the competition with the mutual magnetic interaction of the particles resulting in aggregation and loss of the colloidal stability. The aggregation of particles can be countered by the addition of a ligand. A ligand is a coating material that provide stability to the nanoparticles in a dispersion.[24, 25] The adsorption causes repulsion of the nanoparticles when the nanoparticles approach each other due to the magnetic interaction. In this way, the probability to obtain a ferrofluid enhances.

2.4 Synthesis of magnetite and maghemite by co-precipitation

The difficulty of obtaining stable magnetite dispersions lies in their susceptibility to air oxidation at low temperatures.[26] By heating the magnetite nanoparticles, the Fe^{2+} atoms oxidize to Fe^{3+}, which leads the formation of maghemite and even can become hematite at higher temperatures.[26] Factors to consider for optimizing the thermal stability of magnetite are the grain size, rate of oxidation and the procedure regarding the synthesis. The high energy penalty inhibits the full oxidation of magnetite to hematite in the bulk phase at room temperature. The mechanism of magnetite is shown below. It can be shown that magnetite is formed because of the dehydration reaction of ferrous hydroxide, $Fe(OH)_2$, and ferric oxy-hydroxide, $FeOOH$. The presence of ferric oxy-hydroxide in the sample obtained with $NaOH$ confirms this mechanism. 'Hydrolyzed' ferrous iron species are more readily oxidized than non-hydrolyzed ferrous species in the following order $Fe(OH)_2 > Fe(OH) > Fe^{2+}$ and explains that OH^- ligands donate electron density to the metal ion which increases the reducing power of the metal ion and stabilizes the formed Fe^{3+} during the oxidation.[26]

(1) $Fe^{2+}(aq) + 2\,OH^{-}(aq) \longrightarrow Fe(OH)_2(s)$

(2) $3\,Fe(OH)_2(s) + \frac{1}{2}O_2(g) \longrightarrow Fe(OH)_2(s) + 2\,FeOOH(s) + H_2O(l)$

(3) $Fe(OH)_2(s) + 2\,FeOOH(s) \longrightarrow Fe_3O_4(s) + 2\,H_2O(l)$

(Overall) $Fe^{2+}(aq) + 4\,OH^{-}(aq) + 4\,Fe(OH)_2(s) + O_2(g) \longrightarrow 2\,Fe_3O_4(s)\downarrow + 6\,H_2O(l)$

An alternative ferrofluid synthesis to study is the involvement of co-precipitation. The term implies the meaning of the synthesis since the reaction involves ferric and ferrous ions, such as iron(II) and iron(III) chloride in extremely basic solutions as shown in the equation below.[27, 28]

(1) $Fe^{2+}(aq) + 2\,Fe^{3+}(aq) + 8\,OH^{-}(aq) \longrightarrow Fe_3O_4(s)\downarrow + 4\,H_2O(l)$

The main steps of the mechanism consist of nucleation of iron oxide particles and post growth of the nuclei.[27] Factors that determine the completion of the reaction, i.e., the number density and the size of the nanoparticles, are the initial pH of the solution, the presence of oxygen and the molar ratio (Fe^{2+} : Fe^{3+} = 1 : 2). These factors are listed in Table 1 where the factors show which properties are affected and what the consequences.

Parameter	Property	Dependence
pH value (pH)	Iron oxide phase (ip)	Initial pH increases—formation of nonmagnetic impurities occurs
	Dimension (d)	*pH* increases—*d* decreases *pH* increases—*d* increases
	Shape (s)	acicular, round square
	Magnetism (M_s)	Initial *pH* increases—M_s decreases
Precipitating base agent (OH^-)	Iron oxide phase (ip)	Strong OH^- can cause formation of nonmagnetic iron components
	Dimension (d)	Strong OH^-—*d* increases; wide particle size distribution
Temperature (T)	Iron oxide phase (ip)	*T* decreases—magnetite content increases
	Dimension (d)	*T* increases—*d* increases little influence of *T*
	Magnetism	*T* increases—M_s increases Non-proportional
Fe^{3+}/Fe^{2+} ratio (r)	Iron oxide phase	*r* decreases—magnetite content increases
	Dimension	*r* decreases -*d* increases
	Magnetism	*r* increases -M_s decreases
Iron concentration (C_{Fe})	Dimension	C_{Fe} increases -*d* increases
	Magnetism	C_{Fe} increases -M_s increases
Stirring speed (v)	Dimension	*v* increases -*d* decrease *v* increases -*d* decreases
	Magnetism	-

Table 1: Influence of co-precipitation reaction parameters on the properties of magnetite nanoparticles. Table copied from Ref.[27].

For the pH, it is studied that the magnetic moment decreases as the initial pH increased at room temperature of 25 °C.[29] The increase in initial pH drives oxidation of the Fe^{2+} ions to the ferric state from which an excess of Fe^{3+} ions in the system arises but decreasing the initial pH narrows the size distribution since the precipitation to yield iron hydroxides is avoided. The change of initial pH using sodium carbonate, Na_2CO_3, as precipitation agent is shown in Table 2. Table 2 shows the different pH-conditions to achieve magnetite nanoparticles regarding the particle size, morphology and phase that involves the reaction environment.

pH	Particle size	Morphology	Phase
6	30 ± 4 nm long and 3.2 ± 0.4 nm wide	Homogeneous acicular shape	Goethite (a-FeOOH)
7	440 ± 65 nm 31 ± 1 nm and 4 ± 1 nm width	Nearly square nanoparticles Acicular nanoparticles	Siderite ($Fe(CO_3)$)-primary phase Goethite- secondary phase
8	6.9 ± 0.4 nm Forming aggregates of 50–70 nm	Nearly square nanoparticles Acicular particles	Magnetite-primary phase Goethite- secondary phase Siderite-tertiary phase
9	18 ± 3 nm Forming aggregates of 34 nm	Spheroidal nanoparticles	Magnetite
10	28 ± 5 nm without aggregates	Square nanoparticles Acicular particles	Magnetite-primary phase Goethite- secondary phase (low percentage)

Table 2: Iron oxides nanoparticles and their characteristics, obtained by co-precipitation method at different pH values, using Na_2CO_3 as precipitating agent. Table copied from Ref.[30].

Another crucial factor to consider is the kind of precursors since the precursors affect the mean size, shape and magnetic properties of the magnetic nanoparticles. Commonly, anions of iron salts consist of chloride, sulfate, and nitrate. The growth of oxide nanoparticles in aqueous solution can therefore be controlled by controlling the ionic strength of the reaction solution meaning that changing the iron salt, the ion strength of the solution changes.[27, 31, 32, 33] In Figure 13, various iron salts precursors are combined to obtain magnetite, using a $NaOH$ solution, at 25 °C and under a nitrogen atmosphere. The increase in ionic strength results in reducing the size of the magnetic nanoparticles. For the solutions with the same ionic strength but different mean size of the particles, the behavior was explained by the double layer theory and holds the difference in electrical screening length of the salts. As the anion size of the precursor salt decreases, the synthesized nanoparticles mean size increases.

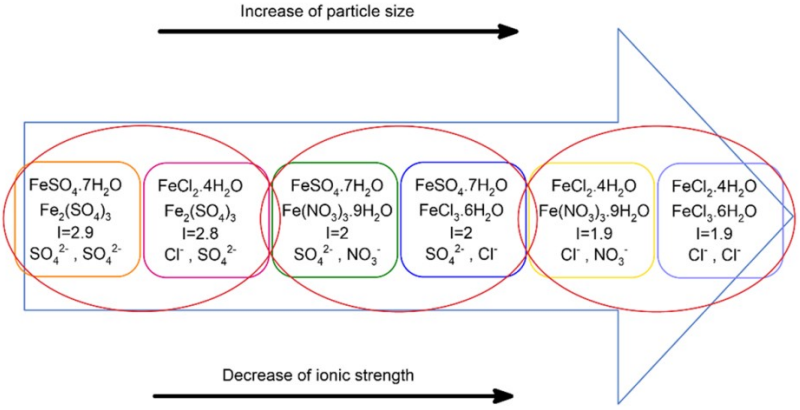

Figure 13: The variation of magnetite nanoparticles size with ionic size and strength, I, of the iron precursors. Figure copied from Ref.[32].

Maghemite ($\gamma - Fe_2O_3$) nanoparticles can be obtained from magnetite nanoparticles by exchanging electrons of Fe^{2+} to Fe^{3+} in acidity environment. The reaction is proposed from the co-precipitation reaction of magnetite but does not dominate the mechanism of the iron ions since the mechanism appears due to magnetic exchange that can occur between ions in different oxidation states, the double-exchange mechanism.[34] This mechanism is explained in section 2.6. In practise, the reaction can be proposed as,[28]

(1) $Fe_3O_4(s) + 2\,H^+(aq) \longrightarrow \gamma - Fe_2O_3(s)\downarrow + H_2O(l) + Fe^{2+}(aq)$

Like for magnetite, the completion of maghemite nanoparticles depends on the experimental conditions. The low pH promotes oxidation of magnetite nanoparticles to maghemite nanoparticles. In addition, the addition of salts in relation with the electrical screening length determines the size distribution of the maghemite nanoparticles as discussed for magnetite. Another parameter to consider is the temperature in which the reaction is executed regarding the dispersity. In Figure 14 and 15, thermograms from TGA analysis [35] and their related size distributions of maghemite nanoparticles are shown, respectively, at different reaction temperatures.[36] The polydispersity of the ferrofluid decreases when increasing the reaction temperature which is denoted since the size distribution becomes smaller at higher reaction temperature. Explanation of the appearance is the diffusion in which the kinetic energy of maghemite nanoparticles increases at higher temperature. The high kinetic energy results in frequent collisions and therefore narrows the size distribution. For the thermograms, the curves exhibit similar weight loss behavior and display two weight losses steps. The initial weight loss starts from the ambient temperature to 200 °C and the final weight loss is within the temperature range of 210 to 450 °C.[36] The initial weight loss is associated with the evaporation of absorbed water and crystalline water from the sample. The final weight loss might be attributed to the evaporation of the remainder bonding water in the sample which will evaporate at water critical temperature of 374 °C.[36] No further significant weight loss or gain is found in the temperature range of 450 °C to 1000 °C, indicating crystalline of maghemite has been formed entirely.[36] Thermal stability (flat line) is achieved faster when increasing the reaction temperature since the formed maghemite nanoparticles at lower reaction time exhibit remnants of crystalline water. Since crystalline water is evaporated as well, the weight percent yield of maghemite nanoparticles is reduced as shown in the Figure. Therefore, with the higher reaction of 90 °C, maghemite nanoparticles are stabilized faster, which increases the weight percent yield.

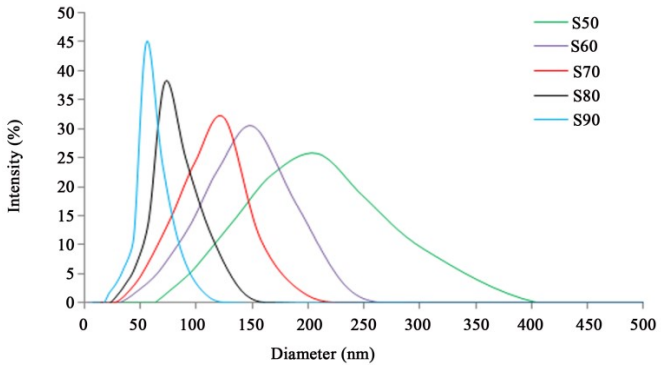

Figure 14: Size distributions of maghemite dispersions at reaction temperature of 50 °C (S50), 60 °C (S60), 70 °C (S70), 80 °C (S80) and 90 °C (S90). Figure copied from Ref.[36].

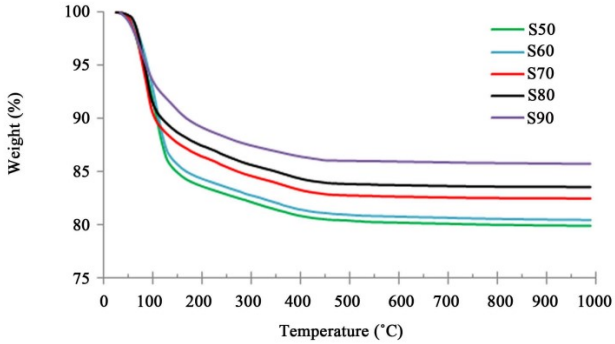

Figure 15: Thermograms of maghemite nanoparticles at reaction temperature of 50 °C (S50), 60 °C (S60), 70 °C (S70), 80 °C (S80) and 90 °C (S90). Figure copied from Ref.[36].

Furthermore, the order of magnitude regarding the size of the magnetic particles indicates the stability of ferrofluids. For ferro- and ferrimagnetic particles, the magnetic domain structure is affected when the sizes of the magnetic particles are reduced. Bulk ferro- and ferrimagnetic materials have multiple magnetic domains. By reducing the size to obtain magnetic nanoparticles, the multiple magnetic domains decreases to a single-domain as shown in Figure 16. Figure 16A shows the coercivity against the particle size. Coercivity is a measure of the ability of a ferromagnetic material to withstand an external magnetic field without becoming demagnetized.[37] Starting from the particle with multiple magnetic domains, a maximum coercivity is reached with decreasing particle size as shown in Figure 16A. The corresponding radius at this maximum coercivity is indicated as the first critical diameter, D_c. At D_c, the electron spins experience direct exchange coupling, causing the spins to become aligned. This leads to a similar behavior as a single magnetic domain. When reducing the particle size further, the coercivity decreases and reaches a second critical diameter that indicates the superparamagnetic size, D_{sp}. This critical diameter depends on the type of a ferri- or ferromagnetic material.[38, 39]
In Figure 16B, the width of the hysteris loop reduces due to the decrease in particle size from a multi to a single domain which alters the type of a ferri- or ferromagnetic material to a superparamagnetic material. Figure 16B shows that close to the first critical radius D_c, the coercivity is at maximum and therefore the width of the hysteresis loop of the magnetization curve will be broad, as denoted by the blue hysteresis curve. When the particles are smaller or larger than a size close to D_c, the coercivity decreases, leading to a narrowering of the hysteresis loop as denoted by the green hysteresis loop. When the particles become smaller than the second critical radius superparamagnetic size, the coercivity becomes zero and the hysteresis behavior disappears for superparamagnetic particles. The absence of a hysteresis loop shows that an external magnetic field is required for magnetization of superparamagnetic particles. Ferrofluids are superparamagnetic and must be magnetized when placing in an external magnetic field.

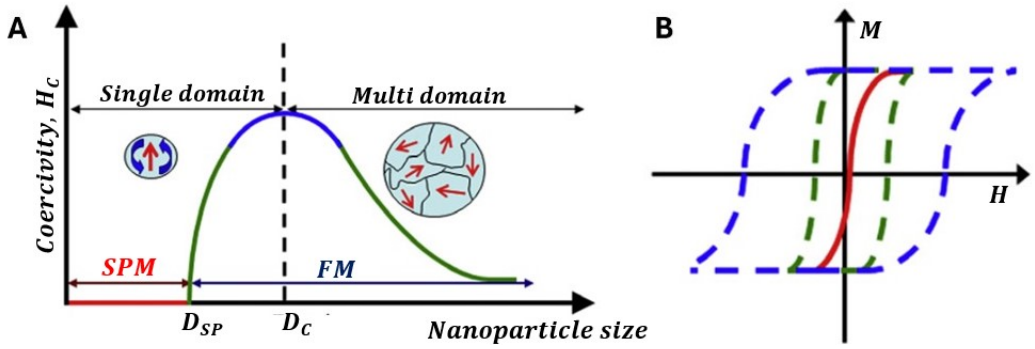

Figure 16: (A) The behaviour of the size-dependent coercivity of magnetic particles. The magnetic behaviour of superparamagnetic (SPM) nanoparticles is demonstrated by the solid line, while ferromagnetic (FM) particles are presented by dashed lines. (B) Here, H and M denote the applied magnetic field strength and the measured magnetization, respectively, with both in $A \cdot m^{-1}$ as unit. Superparamagnetism occurs in particles with sizes smaller than the superparamagnetic limit. Figures copied from Ref.[18].

The interaction energy for a magnetic particle is given below.[9]

$$U = -\mu_0 \cdot \overrightarrow{H} \cdot \overrightarrow{m}_d = -\mu_0 \cdot H \cdot m_d \cdot cos(\theta) \tag{8}$$

- U is the interaction energy (J).
- $\overrightarrow{m}_d$ is the magnetic dipole moment ($A \cdot m^2$).
- μ_0 is the magnetic permeability of vacuum ($4\pi \cdot 10^{-7} N \cdot A^{-2}$).
- H is applied magnetic field ($A \cdot m^{-1}$).
- θ is the angle between the magnetic dipole and the applied magnetic field (°).

The expression for the interaction energy shows that the energy is the lowest by orienting the dipole moment parallel to the direction of the applied magnetic field. When an inhomogeneous magnetic field is applied, the particles move to the higher magnetic field gradient since the interaction energy is the lowest there. With a gradient in the magnetic field, a flow of the magnetic particles can be induced.
The interaction energy between magnetic particles can lead to the formation of dipolar chains (or aggregates) as shown in Figure 17. The formation of dipolar chains depends whether the magnetic attraction between two particles that touch each other is weaker or stronger than thermal energy k_BT. If the magnetic attraction is weaker than the thermal motion of the colloidal particles, the colloidal particles easily breaks the magnetic contact and particles remain separate as shown in Figure 17A. If the magnetic attraction dominates the thermal motion, dipolar chains of particles are formed spontaneously as shown in Figure 17B. If dipolar chains already form without external magnetic field, the dipolar chains grow larger with magnetic field as shown in Figure 17C. These dipolar formations can be encountered by making particles sufficiently small or by increasing the distance between magnetic cores by applying surface modification. When the particle size is increased or the length of the ligands is decreased the cores can come closer to each other. The dipolar structural transformations depends therefore on several factors like the concentration of the particles, use of stabilizing agents, the magnetic moments of the particles, the thickness of the surface layers on the particles, the applied external magnetic field and the temperature.[40]

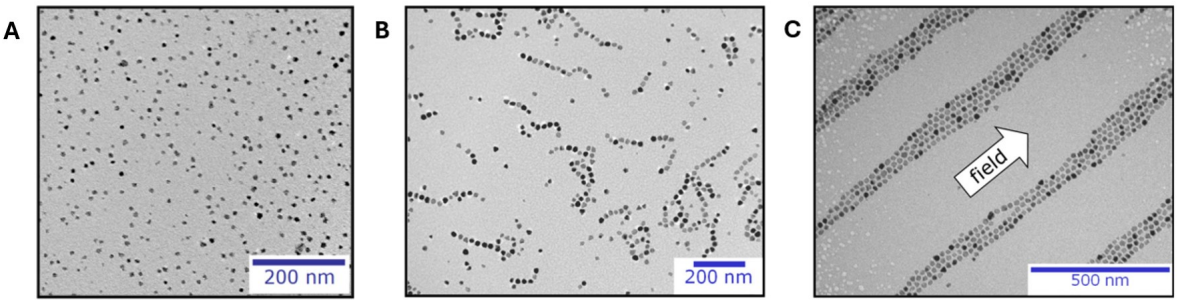

Figure 17: Cryogenic transmission electron microscopy of magnetic nanoparticles dispersed in an apolar liquid. Figure copied from Ref.[9]. The particles in (A) have a magnetic contact interaction below k_BT and therefore do not form dipolar structures, with or without external field. The particles in (B) and (C) have a contact interaction of -10 k_BT, sufficient for spontaneous dipolar chain formation in zero external field (B).[41] In an external magnetic field, the chains grow into bands (C).[42]

Figure 18 shows the dipolar spheres and Eq. 9 expresses the corresponding interaction energy at distance a (m) between the magnetic particles. The interaction energy is maximal since the magnetic particles touch and the dipoles point in the same direction, the so-called head-to-tail configuration, with all the angles equal to zero.[9]

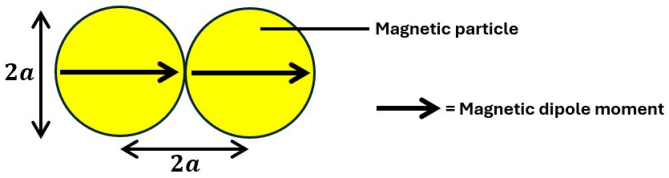

Figure 18: Dipolar spheres of radius a. Figure is adapted from Ref.[9].

$$U_{max} = \frac{\mu_0 \cdot (m_d)^2}{2\pi(2a)^3} \tag{9}$$

where m_d and μ_0 are the magnetic dipole moment $(A{\cdot}m^2)$ and permeability of vacuum $(N{\cdot}A^{-2})$, respectively.

Dipolar structure formation must thus be avoided in order to make stable ferrofluids. This implies using magnetic nanoparticles that are sufficiently small, typically 10 nm in the case of magnetic iron oxides, and providing the particles with effective colloidal stabilization (steric and/or charge stabilization).[9] Figure 19 shows the interaction energy by steric stabilization. The addition of adsorbed molecules increases the distance between the magnetic particles and therefore reduces the interaction energy, $U_{stabilization}$, as given in Eq. 10.

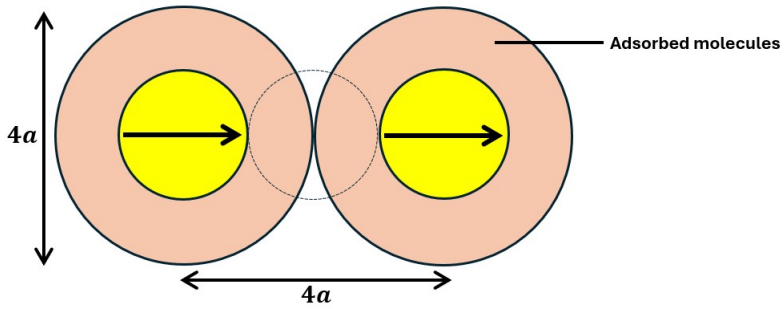

Figure 19: Dipolar spheres (surface modified) of radius a. The interaction energy decreases since the attractive force between the spheres is limited by an adsorbed layer of molecules on each sphere. Figure is adapted from Ref.[9].

$$U_{stabilization} = \frac{\mu_0 \cdot (m_d)^2}{2\pi(4a)^3} \tag{10}$$

where $U_{stabilization} < U_{max}$

2.5 Solvothermal synthesis of YAG and YIG nanoparticles

The process of solvothermal synthesis of YIG-on-YAG particles can be divided into nucleation and seeded growth. Nucleation theory is discussed first before the seeded growth process of YAG and YIG nanoparticles is explained.

2.5.1 Nucleation theory

The principle of solvothermal synthesis begins by considering the nucleation theory. Nucleation theory involves dispersing of precursors in a solvent using external conditions, such as temperature, to produce nuclei or clusters.[43, 44] Nucleation is difficult to control in particle size due the rapid cluster formation. This makes the process challenging in understanding the behaviour. Theoretically, the nucleation process can be related with the Gibbs free energy which is given for a spherical shape nuclei by considering the volume energy, ΔG_V and the surface energy, ΔG_s [43, 44]:

$$\Delta G = \Delta G_V + \Delta G_{surf} = -\frac{4}{3}\pi a^3 \frac{k_B T}{V} \ln(S) + 4\pi a^2 \gamma \tag{11}$$

with $S = \frac{c_s}{c_{sat}}$

where V is the bulk volume (m^3), a the radius of the nuclei (m), k_B is the Boltzmann constant (J/K), T is the temperature of the system (K), γ is the surface free energy (N/m), and S is the saturation ratio. The saturation ratio contains the solute concentration, c_s, with respect to the saturation concentration, c_{sat}, the concentration at which the solution is in thermo-dynamic equilibrium with the bulk. Supersaturation can

be indicated when $c_s > c_{sat}$ and yields a decrease in the Gibbs free energy.
By setting $\frac{d\Delta G}{da} = 0$, the critical radius of the nuclei, a^*, is then expressed as,

$$a^* = -\frac{2V\gamma}{k_B T \ln(S)} \tag{12}$$

The equation indicates the formation of smaller nuclei when enhancing the saturate of the solution. It is easy to find that the more saturate the solution is, the smaller the nucleus is, which is also beneficial for the nucleation process. Figure 20a shows the time-dependent nucleation process by considering the concentration of the solute particles as the atomic concentration including the growth part. In addition, the Gibbs free energy is plot by altering the particle radius in Figure 20b.

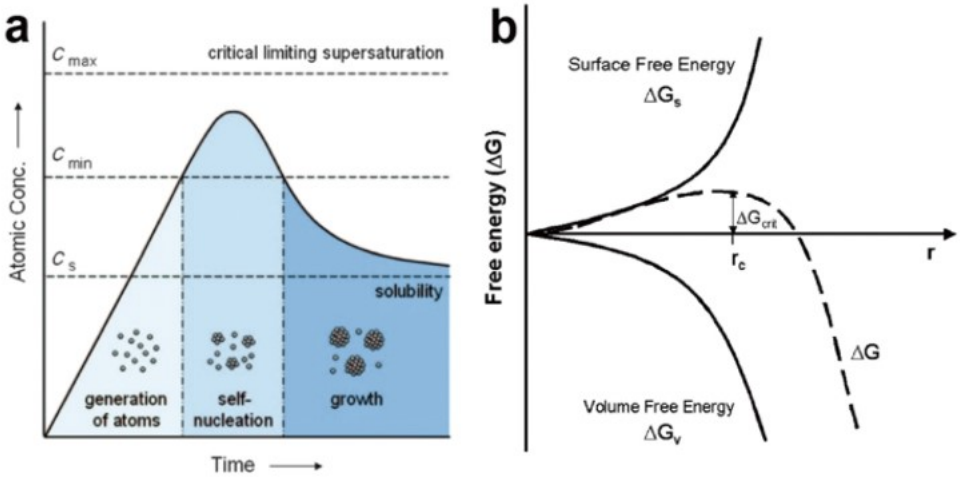

Figure 20: (a) Atomic concentration profile against time, illustrating the nucleation process and subsequent growth. (b) Free energy diagram for nucleation process. Figure copied from Ref.[43].

Figure 18*a* shows once the concentration of atoms exceeds the point of supersaturation at c_{min}, the atoms start to aggregate into small clusters. The nucleation process will not stop until the equilibrium of generating metal atoms from decomposition of metal salts is reached. If the concentration of atoms drops quickly below the level of minimum supersaturation, no additional nucleation occurs.[43, 45] When the concentration of metal atoms is below the minimum supersaturation, the metal atoms cannot be supplied by the decomposition of metal salts and the nuclei will readily grow to form nanocrystals, which can be defined as the growth step.[43, 45]
Figure 18*b* illustrates the competition between the decrease in ΔG_V and increase in ΔG_s. As the liquid phase is less stable than the solid phase, ΔG_V has a negative sign and therefore facilitates the nucleation, while ΔG_s has a positive sign due to the new interface of solid/liquid and therefore benefits the dissolution of the metal salts.[43] The generation rate of nuclei from each unit volume, J, can then be expressed as in the Arrhenius reaction rate equation[43]:

$$J = A \cdot e^{-\frac{\Delta G_{crit}}{k_b \cdot T}} \tag{13}$$

where A is the pre-exponential factor which is strictly related to the molecular mobility and temperature.

The nucleation process can be divided into homogeneous and heterogeneous nucleation. The explanation can also be interpreted for homogeneous and heterogeneous seeded growth. The basic difference between homogeneous and heterogeneous nucleation is the required activation energy to initiate nucleation. From Figure 21, it can be denoted that heterogeneous nucleation has a lower activation energy than homogeneous nucleation.

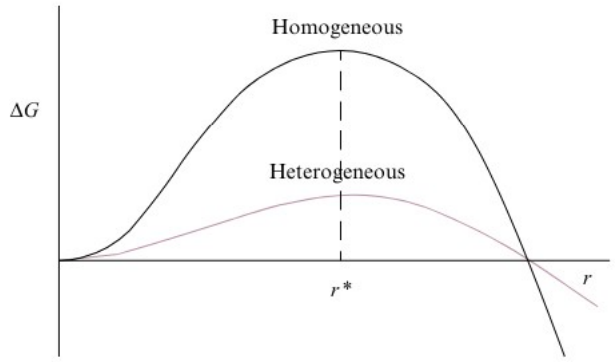

Figure 21: Difference in free energy of nucleation for homogeneous and heterogeneous nucleation where the radius a is denoted as r. Figure copied from Ref.[46].

The activation energy for heterogeneous nucleation is proportional to that of homogeneous nucleation by a factor of $S(\theta)$. The relation between homogeneous nucleation, ΔG_{hom}, and heterogeneous nucleation, ΔG_{het}, is expressed as follows[46]:

$$\Delta G_{het} = \Delta G_{hom} \cdot S(\theta) \tag{14}$$

where $S(\theta) = (1/4)(2 + cos\theta)(1 - cos\theta)^2$ with the contact angle, $0° < \theta < 180°$
If $\theta = 0°$, the nuclei fully adsorb on each other due to their low surface energy.
If $\theta = 180°$, the nuclei do not adsorb on each other due to their high surface energy.
Heterogeneous nucleation considers the presence of nucleation sites whereas homogeneous nucleation needs to form nucleation sites to promote nucleation. The nucleation density, that considers the number of nucleation sites, is higher for heterogeneous than homogeneous nucleation. The presence of nucleation sites decreases the contact angle ($\theta < 180°$) and results in $S(\theta) < 1$. This condition yields a free energy of nucleation where $\Delta G_{het} < \Delta G_{hom}$ as shown in Figure 21.

2.5.2 Seeded growth of YAG and YIG nanoparticles

To obtain YIG, the type of synthesis needs to be studied since the nucleation barrier to form single phase YIG is too high for a single-step synthesis and can therefore be interpreted as not feasible. According to Rongjin, YIG particles can be synthesize via solvothermal reaction that involves seeded growth.[6] Solvothermal synthesis involves the formation of nanoparticles of metal oxides dispersed in various organic solvents.[47]
The additional method of seeded growth is to counter the nucleation barrier by heterogeneous seeded growth and makes the synthesis of YIG particles efficient to implement in terms of energy input (i.e., at elevated temperatures of 200 to 300 °C).[47] This brings the synthesis of a substrate that supports and stimulates the growth of YIG particles. According to Rongjin, seed crystals of Yttrium Aluminum Garnet (YAG) can be used to execute seeded growth.[47] YAG is a garnet crystal like YIG with the molecular formula $Y_3Al_5O_{12}$ and has a similar crystal structure as YIG as shown in Figure 22. From the Figure, it can be shown that the position of Y^{3+} corresponds with the position of Y^{3+} for YIG. The difference is the occupation of Al^{3+} in both tetrahedral and octahedral site and not like for YIG where the sites are occupied with Fe^{3+} ions. The symmetry makes YAG therefore an ideal compound for the synthesis of YIG.

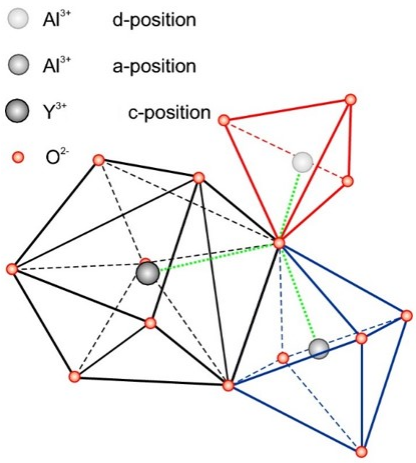

Figure 22: Crystal structure of Yttrium aluminium garnet. Figure copied from Ref.[48].

In addition, the type of seeded growth is considered due to the difference in the synthesis of YAG and YIG. Seeded growth of YAG nanoparticles is denoted as homogeneous seeded growth due to the adsorption of the same nuclei to form the same type of nanoparticles that do not differ in chemical composition. For the seeded growth of YIG, the formed YAG nanoparticles are used to adsorb YIG nuclei for growing YIG nanoparticles. This process alters the chemical composition since the formed YIG nanoparticles contain a core with a certain mass fraction fused YAG nanoparticles. Therefore, the synthesis of YIG nanoparticles is denoted as heterogeneous seeded growth. The heterogeneous seeded growth of YIG nanoparticles is illustrated in the adapted Figure 23.

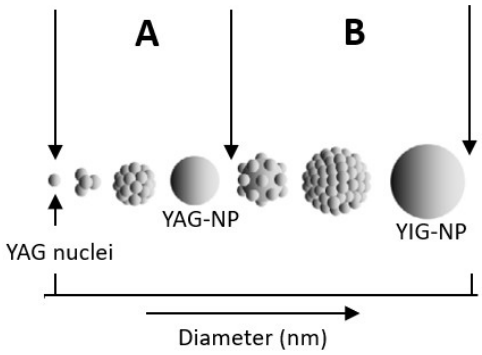

Figure 23: Principle of seeded growth. Figure adapted from Ref.[49]. *A: homogeneous seeded growth of YAG nanoparticle (YAG-NP), B: heterogeneous seeded growth of YIG nanoparticle (YIG-NP).*

Reactants that involve the solvothermal reactions to obtain YAG are aluminium compounds like aluminium hydroxides, aluminium alkoxides, and various organic solvents alcohols, glycols, and inert organic solvents.[47] The compound that is investigated for understanding the formation of YAG and as follow-up YIG is the presence of aluminium alkoxide in organic environment. Therefore, the influence of aluminium alkoxide is reviewed only. Since the thermal reaction is carried out in the bulk phase of glycol molecules, the solvothermal reaction is termed 'glycothermal reaction'.[47]

The reaction of aluminium alkoxides in glycol forms the glycol derivative of boehmite.[47, 50] However, the size of the crystal structure can be influenced by adding a particular glycol molecule that differs in chain length. The following glycol molecules are constructed in Figure 24.

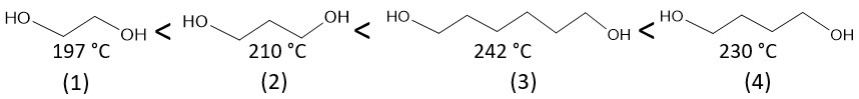

Figure 24: Structural formula of glycol molecules ordered upon increasing crystallite size.[50] [constructed with Chemsketch]

It is noted that the glycol structure containing 5 carbon atoms is not included in the reference, but is assumed that the glycol structure lies between (3) and (4) since the glycol structure (4) is the most suitable for YAG synthesis but has one carbon atom less than (3) which contradicts the relation that the increase in carbon atoms of glycols improves the completion of YAG. This appearance is explained by the intermolecular product of the glycol molecules during the synthesis. The relation between the intermolecular product of the glycol molecules and the completion of the YAG synthesis is explained with the reaction mechanism below (Figure 25). The mechanism only shows the structure for one carbon chain, but the mechanism also applies to the other carbon chains and is denoted with the rest group, R. The growth of the crystallite size is controlled by the heterolytic cleavage of O-C bonds where the glycoxide intermediate, $(R)_2 - Al - O - (CH_2)_n OH$, is formed by alkoxyl exchange between aluminium alkoxide and the glycol used as reaction medium.[51]

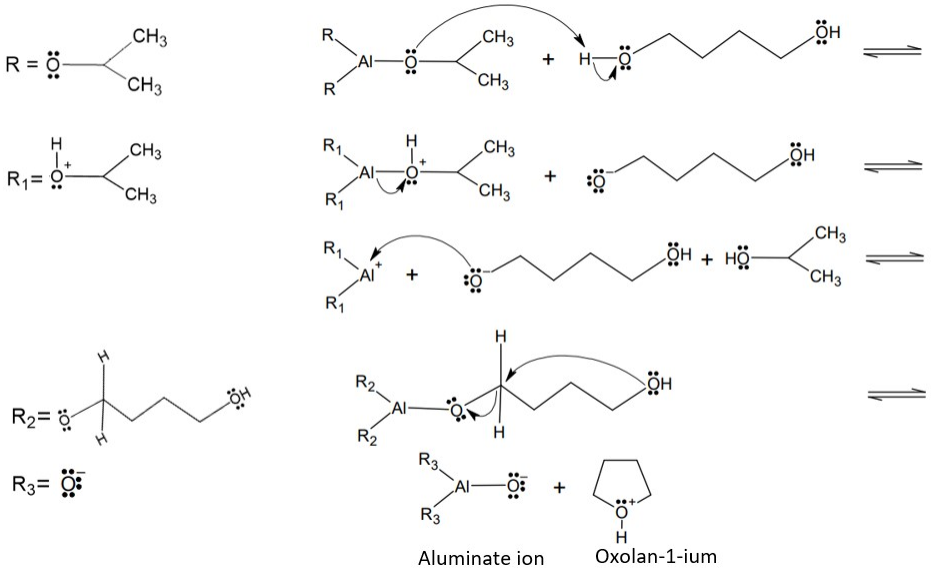

Figure 25: Proposed reaction mechanism of alkoxide with the glycol molecule containing four carbon atoms (1,4-butyleenglycol also known as 1,4-butanediol). [constructed with Chemsketch]

The main product of the reaction is aluminate ion and the by-product is oxolan-1-ium when implementing a glycol molecule with four carbon atoms. Figure 26 shows by-products when glycol molecules with different number of carbon atoms is used.

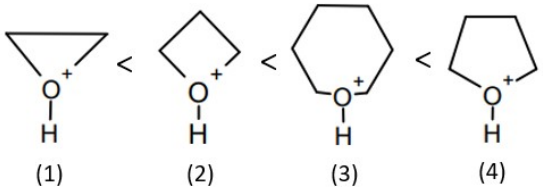

Figure 26: Structural formulas of by-products when glycol molecules contain 2, 3, 6, and 4 carbon atoms, respectively, ordered in increasing yield of YAG crystallite. [constructed with Chemsketch]

The tendency to form a cyclic structure increases with the chain length of the primary alcohol group that performs the intramolecular interaction. From Figure 26, the probability to achieve the structures (1) and (2) is minuscule due to the small bond angle and therefore the high reactivity to be decomposed with the result that the bond re-forms between the glycol molecule and the aluminate ion. The choice of the glycol molecules that form the byproducts (3) and (4) and its relation with the yield of garnet crystals can be explained by the steric hindrance. From Figure 24, the crystallite yield is higher for glycol molecule (4) due to the lower steric hindrance of the hydrocarbon atoms and therefore the higher probability of intramolecular interaction (reaction step before aluminate ion is formed).
A similar reaction mechanism follows when using yttrium acetate as starting material to form yttriuminate ion as shown in Figure 27. By compressing the proposed aluminate ion and yttriuminate ion at high pressure, a YAG nucleus is obtained. To obtain a YIG nucleus, a similar reaction takes place as shown in Figure 25, but instead of aluminum isopropoxide, a precursor containing Fe atoms such as iron(III) acetylacetonate is used. The reaction decomposes the target iron oxide part of the ester compound to then be compressed with the proposed yttriuminate ion.

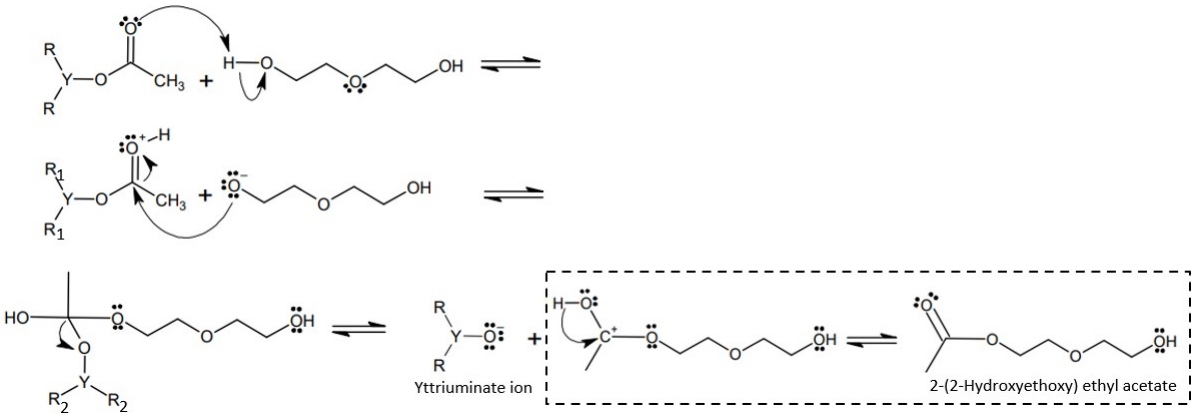

Figure 27: Proposed reaction mechanism of yttrium acetate with the glycol molecule containing four carbon atoms (diethylene glycol). [constructed with Chemsketch]

The YIG mass fraction of formed nanocrystals in the bulk phase, $wt\%_{YIG}$, can be determined based on the diameters before and after seeded growth knowing the densities of YAG and YIG,[6]

$$wt\%_{YIG} = \frac{wt\%_{YAG} \cdot \rho_{YIG}[(D_2)^3 - (D_1)^3]}{\rho_{YAG}(D_1)^3} \tag{15}$$

- D_1 and D_2 are the crystallite size before and after heterogeneous seeded growth respectively (m).
- ρ_X is the density of compound X $(kg \cdot m^{-3})$.
- $wt\%_X$ is the mass fraction of compound X (%).

By considering the equation proposed by Rongjin, the final YIG nanoparticle is illustrated in Figure 28.

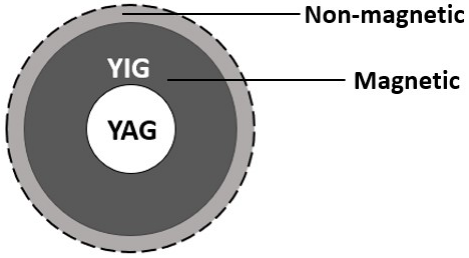

Figure 28: Particle structure of a YIG-on-YAG nanoparticle.

The particle structure shows the presence of a YAG core enclosed by YIG nanoparticles. The different layers can be indicated as the part that contributes for the magnetic behaviour but the magnetic behaviour does not occur over the entire nanoparticle since the the non-magnetic layer does not participate on the magnetic behaviour even though the layer represents the YIG layer as well. This phenomena is explained by the magnetic strength near the edge of the YAG core till the surface of the YIG nanoparticle. The region between the surface of the YIG layer and that of the YAG core has the optimal magnetic contribution from which the magnetic behaviour of the particle appears. Near the surface of the YIG layer, the magnetic nanoparticles are affected by the chemical interactions with the adsorbed ligand when the YIG-NPs are coated. The adsorption of ligands can be interpreted as an additional layer on the non-magnetic layer to counter aggregation for obtaining a ferrofluid. The adsorption of ligands is not due magnetic interaction but other types of chemical bonds. In addition, the adsorbed ligands are organic molecules and can be indicated as diamagnetic. The diamagnetism of the adsorbed ligands limits the magnetic moment of the YIG nanoparticle. A similar argument can be done near the surface of the YAG core where the YIG nanoparticles bonds with the YAG core. YAG is a diamagnetic material and therefore limits the magnetic behaviour of YIG nanoparticles as well.[52]

2.6 Optical absorbance of ferrofluids

The optical density of a ferrofluid is affected by the electronic band structure (ES) of the magnetic particles.[53] This consists of filled and completely empty electronic bands, or it includes a partially completed filled band, depending on the presence of Fe^{2+} and Fe^{3+} in tetrahedral and octahedral sites as shown in Figure 29. Yttrium Iron Garnet and maghemite have completely filled and completely empty electronic bands, while magnetite includes a partially filled band.[53] The addition of Y^{3+} alters the spectrum more in comparison with maghemite. The difference in ES between the iron ions and their occupation in the tetrahedral and octahedral sites is explained by crystal field splitting and the different types of charge transfers transitions that occur in the visible region.

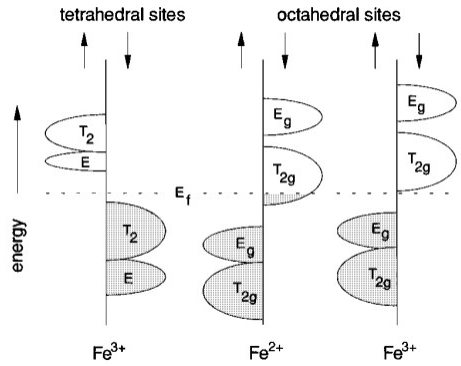

Figure 29: Electronic band structure of iron ion at tetrahedral and octahedral sites. Figure copied from Ref.[53].

In Figure 30, the absorption coefficient per volume fraction is given for maghemite and YIG and shows high absorption coefficients of maghemite compared to YIG. Maghemite absorbs all wavelengths in the visible region of the electromagnetic spectrum, whereas the absorpbtion of YIG is one order of magnitude lower At 780 nm than for maghemite, and at 1100 nm, it is two orders of magnitude lower. YIG has therefore a lower optical absorption and can be proposed as a transparent ferrofluid on macro scale.

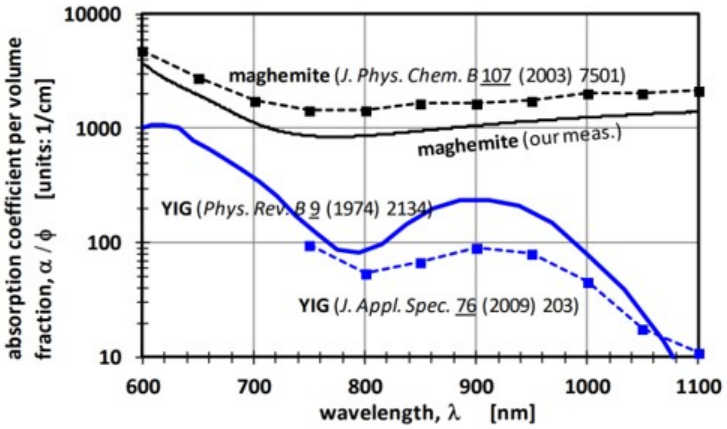

Figure 30: The absorption coefficient per volume fraction of maghemite and yttrium iron garnet in wavelength range from near infrared (NIR) to ultraviolet.[3, 4, 5, 54]. Figure is created by B. H. Erné (supervisor) and 'Our meas.' refers to measurements carried out by A.M. van Silfhout (supervisor).

The electron configurations of Fe^{3+} and Fe^{2+} are $[Ar]3d^5$ and $[Ar]3d^6$, respectively. In a free ion, the d-orbitals degenerate but the occupation of the ions in sites causes the ions to have a crystal field splitting and coulombic interaction with O^{2-} ions. The splitting of the d-orbitals due to the coulombric interaction is given in Figure 31a. The d-orbitals in an octahedron configuration and in a tetrahedron configuration are illustrated in figures 31b and 31c, respectively where the black dots represents the anions.

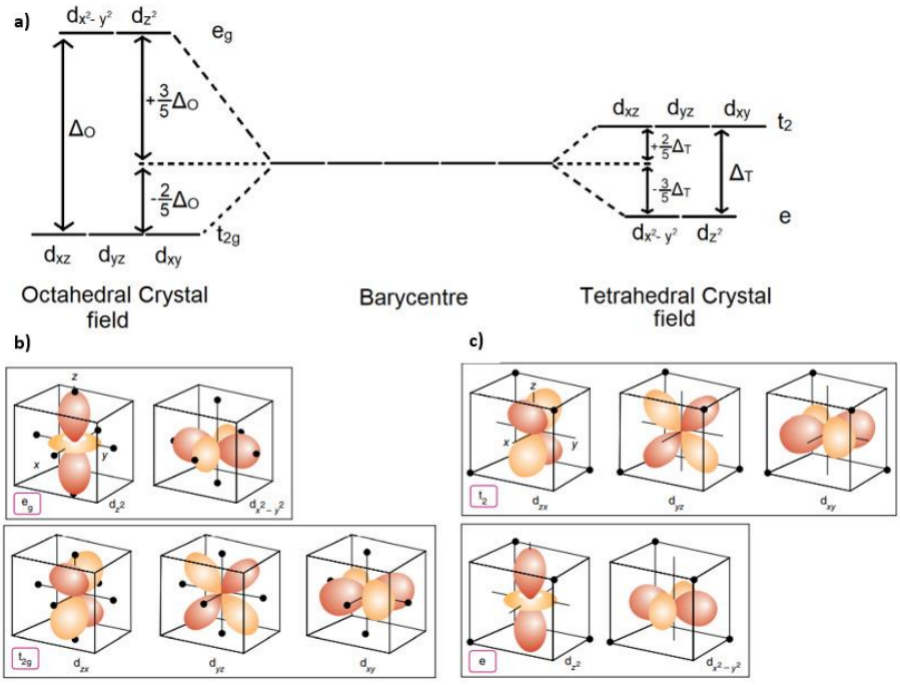

Figure 31: Octahedral and tetrahedral crystal-field splitting. a) Splitting of the d-orbitals in an octahedron (left) and a tetrahedron (right), b) Representation of the d-orbitals in an octahedron, c) Representation of the d-orbitals in a tetrahedron. Figure copied from Ref.[55].

The repulsion of the d-orbital increases when the lobes of the d-orbitals approach the negative point charges (anions). In Figure 31b, it is shown that the d-orbitals corresponding to the d_{z^2} and $d_{x^2-y^2}$ in an octahedral configuration have their lobes pointing in the direction of the negative point charges of the ligand, whereas the d_{xz}, d_{yz} and d_{xy} have their lobes pointing in between the point charges due to the stronger repulsion and therefore higher energy than the d_{xz}, d_{yz} and d_{xy} orbitals. The crystal field splitting is given by the octahedral crystal-field parameter Δ_O.
For the d-orbitals in a tetrahedron in Figure 31c the situation is the opposite. The d_{xz}, d_{yz} and d_{xy} orbitals are located closer to the negative point charges than the d_{z^2} and $d_{x^2-y^2}$. The splitting of the d-orbitals is because of that indicated with e-orbitals for d_{z^2} and $d_{x^2-y^2}$ and t_{2g}-orbitals for d_{xz}, d_{yz} and d_{xy}. The crystal field splitting is given by the tetrahedral crystal-field parameter Δ_T. $\Delta_T < \Delta_O$ due to smaller repulsive interaction of the d-orbitals with the negative point charges when comparing the tetrahedron with the octahedron. This brings the relation $\Delta_T \approx \frac{4}{9}\Delta_O$.[55]

The occupation of the electrons in the d-orbitals depends on the crystal-field splitting parameter since the strength of this parameter depends the bond strength of the centered cations with the surrounding ligands. If the crystal-field splitting parameter is larger than the spin pairing energy, the electrons will remain paired as much as possible in the so-called low-spin complex. If the crystal-field parameter is small, the electrons want to adopt a configuration which contains as many unpaired spins as possible which is denoted as the high-spin complex.[55] This is the case for an octahedron. For a tetrahedron, the spins are ordered in a high-spin configuration due to the small Δ_T. O^{2-} is a weak-field ligand, causing the electrons to be in the high-spin configuration.[55] The high-spin configurations of Fe^{3+} in a tetrahedron and octahedron and Fe^{2+} in octahedron are given in Figure 32.

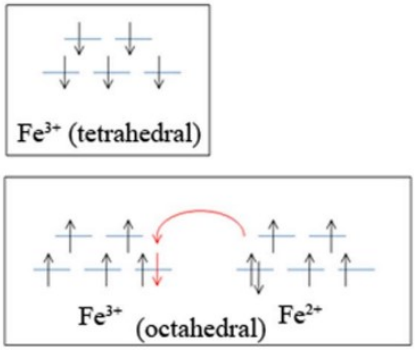

Figure 32: High-spin configurations of Fe^{3+} in a tetrahedron and an octahedron and of Fe^{2+} in an octahedron. Figure copied from Ref.[34].

Fe^{3+} and Fe^{2+} ions in an octahedral configuration are ferromagnetically coupled due to the parallel alignment of the spins via a double-exchange mechanism through oxygen.[34] The double-exchange mechanism holds the transfer of an electron from Fe^{2+} to Fe^{3+} in an octahedron via an O^{2-} ligand, so that a spin in a Fe^{2+} 'leaps' to a Fe^{2+} and therefore seems if Fe^{2+} and Fe^{3+} swap places as indicated by the red arrow in Figure 32. The Fe^{3+} ions located in an octahedron and tetrahedron are anti-ferromagnetically coupled through O^{2-} ligand.[34]

2.6.1 Intervalence and intersublattice charge transfer transitions

Optical transitions between the Fe ions can be explained by intervalence charge transfer (IVCT) transitions and intersublattice charge transfer (ISCT) transitions. In an IVCT transition an electron is promoted from an ion with lower oxidation number to an ion with higher oxidation number via optical excitation, i.e., an electron from Fe^{2+} in an octahedron is promoted to Fe^{3+} in an octahedron or tetrahedron.[56]
IVCT transitions from Fe^{2+} in an octahedron to Fe^{3+} in an octahedron is indicated as[56]:

$$[Fe^{2+}]_{t_{2g}} \longrightarrow [Fe^{3+}]_{t_{2g}}$$
$$[Fe^{2+}]_{t_{2g}} \longrightarrow [Fe^{3+}]_{e_g}$$

The IVCT transitions from Fe^{2+} in an octahedron to Fe^{3+} in a tetrahedron is indicated as[56]:

$$[Fe^{2+}]_{t_{2g}} \longrightarrow [Fe^{3+}]_{e}$$
$$[Fe^{2+}]_{t_{2g}} \longrightarrow [Fe^{3+}]_{t_2}$$

An ISCT transition between Fe ions is an IVCT transition between the trivalent Fe^{3+} ions in an octahedron and tetrahedron.[56] ISCT transitions from Fe^{3+} in an octahedron to Fe^{3+} in a tetrahedron are indicated as[56]:

$$[Fe^{3+}]_{e_g} \longrightarrow (Fe^{3+})_{e}$$
$$[Fe^{3+}]_{e_g} \longrightarrow (Fe^{3+})_{t_2}$$

ISCT transitions from Fe^{3+} in a tetrahedron to Fe^{3+} in an octahedron is indicated as[56]:

$$[Fe^{3+}]_{t_2} \longrightarrow [Fe^{3+}]_{t_{2g}}$$
$$[Fe^{3+}]_{t_2} \longrightarrow (Fe^{3+})_{e_g}$$

IVCT and ISCT dominant transitions occur between the range of 2 and 6 eV (between 620 nm and 206 nm) and therefore causes the visible spectrum to be absorbed strongly.[57] There must be noted that the given energies at which these transitions occur, are for Fe_3O_4. Since maghemite consist of Fe^{3+} ions, ISCT transitions are involved only which lowers the optical absorpbtion in comparison to magnetite. Yttrium iron garnet has additional Fe^{3+} and Y^{3+} ions. The presence of Y^{3+} creates a band gap with an band gap energy of 2.6 eV from which YIG is capable to absorb wavelengths in the visible region.[58, 59, 60]

2.7 Characterization techniques

2.7.1 TEM

Transmission Electron Microscopy (TEM) is a high-resolution microscopic technique in which a beam of electrons is transmitted through a specimen to form an image.[61, 62] The technique is shown in Figure 33.

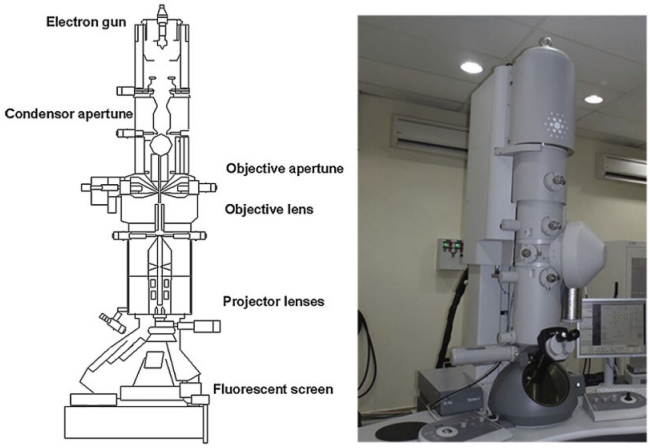

Figure 33: Schematic diagram of transmission electron microscope. Figure copied from Ref.[61].

Electron beams are generated from an electron gun and focused by metal apertures and electromagnetic lenses in the column of a TEM.[61] The mechanism is based on the wavelike character of electrons and the deflection of the electrons by magnetic and electrical fields.[61] The transmitted electrons are applied to the specimen in the column and irradiated through the TEM grid as well as the sample that is mounted on the TEM grid. The thickness of a TEM specimen must be within 100 nm for electrons to pass through.[61] Factors of the specimens that influence the impact on the transmission of electron beam are the density and composition of the specimen.[61] Highly dense material are less observable through TEM due to the low transmission. The condenser lens can then be applied to obtain an TEM image by focussing the electrons beams and therefore increasing the intensity. The transmitted electrons are refocused and then magnified by an electromagnetic lens system consisting of two lenses after they pass through the specimen. Subsequently, the transmitted electrons are projected on a phosphor screen to convert the electron image.[61] TEM could obtain high resolution in nano-scale for the extremely shorter wavelength when applied electron beams are accelerated at several hundred kilovolts. Based on this knowledge, the following relation can be applied, where λ is the wavelength and V is the acceleration voltage[61],

$$\lambda \sim \frac{1.23}{\sqrt{V}}(nm) \tag{16}$$

For the electrons to displace through the column, the mean free path is enhanced by placing the column under high vacuum.[61] The improvement in the mean free path enhances the resolution and therefore enables the recording of crystal structures using electrons with short wavelength.

2.7.2 DLS

Dynamic Light Scattering (DLS) is a characterization technique for determining the colloidal object size distribution of a colloidal system.[63, 64, 65] The colloids move due to their kinetic energy (Brownian motion) and arises due to the collision with solvent molecules. The hydrodynamic size can be determined due to the relation between the Brownian motion and viscous force as already mentioned in section 1.3. The movement of colloids are monitored over a time range. The displacement of larger colloids is nearly similar as the initial position due to the low diffusion, whereas smaller colloids diffuse faster without a specific position. The difference in diffusion rate can be displayed as a difference in fluctuations between large and small colloids as shown in Figure 34a. The time-dependent intensity fluctuation of the scattered light at a particular angle can then be characterized by plotting the auto-correlation function (correlogram) as illustrated in Figure 34b. The function $C(q, \tau)$ is then obtained for a series of delay time, τ, and represents the correlation between the intensity at t_1 ($I(q, t_1)$) and the intensity after a time delay of τ ($I(q, t_1 + \tau)$).[64] The variable q represents the magnitude of the scattering wave vector (m^{-1}) and is given by:[64]

$$q = \frac{4\pi \cdot n}{\lambda} \cdot sin\left(\frac{\theta}{2}\right) \tag{17}$$

where n is the dimensionless refractive index of the solution, λ is the wavelength in vacuum of the incident light intensity and θ is the scattering angle.
The auto-correlation function decays more rapidly for small particles than for the large particles.

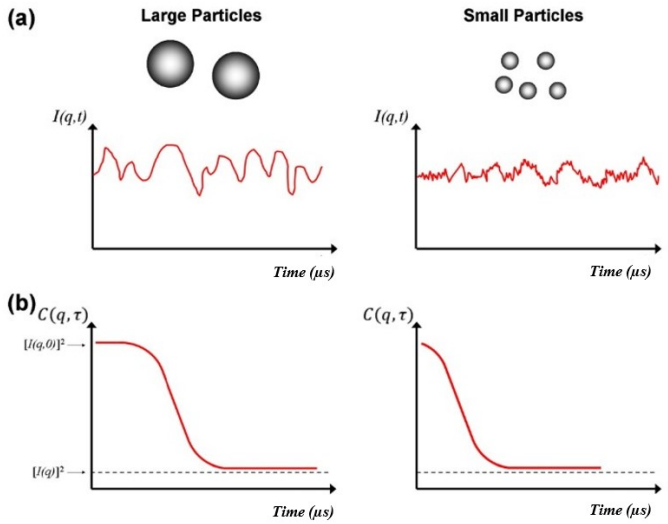

Figure 34: Schematic illustration of intensity measurement and the corresponding auto-correlation function (correlogram) in dynamic light scattering. (a) Intensity fluctuation of scattered light with time, and (b) the variation of auto-correlation function with delay time (logarithmic scaled). Figure copied from Ref.[64].

The DLS setup consist of a monochromatic laser that encounters a colloidal system. The incident light scatters in all directions. The scattering intensity is recorded by a detector as shown in Figure 35. The monochromatic incident light will undergo a phenomenon called Doppler broadening as the colloids are in continuous motion in the dispersion.[63] It is therefore important that the dispersion is translucent with no dust particles since these points of interest predominates the measurements. The measurements of the colloidal object size can be distinguished in data that informs the number, volume and intensity distribution. In Figure 36, measurements of a colloidal system with two distributions for the number, volume and intensity distribution. The distributions correspond to a mean particle size of 5 and 50 nm. The number distributions of 5 and 50 nm are similar. The similar distributions indicate an equal number of 5 nm and 50 nm particles in the colloidal system. The volume distributions are affected by the size of the nanoparticles since larger

nanoparticles have a larger volume. Since the mean size of the nanoparticles differ with a factor 10, the volume distribution is affected to the third power indicating that the volume distribution of 50 nm is 10^3 higher than 5 nm. For the distributions that considers the intensity, the two particle sizes are separated with a factor of 10^6 due to the difference in scattering intensity. The scattering intensity increases with increasing colloidal size indicating that the mean size of 50 nm shows a larger scattering intensity than the mean size of 5 nm. The choice of the type of distributions therefore depends on the analysis of the colloidal system. A dispersion containing large aggregates is suitable for measuring the intensity distribution, whereas for the focus of small nanoparticles the number distribution is applied when the presence of large aggregates interfere the detection of small nanoparticles.

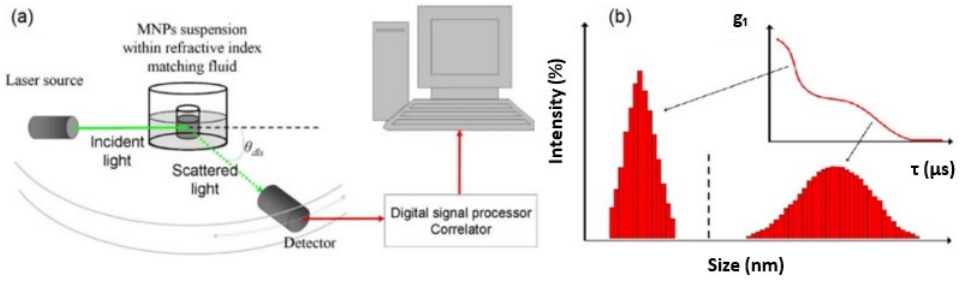

Figure 35: A schematic of the DLS setup (a) and the acquired results (b). Figure copied from Ref.[64, 66].

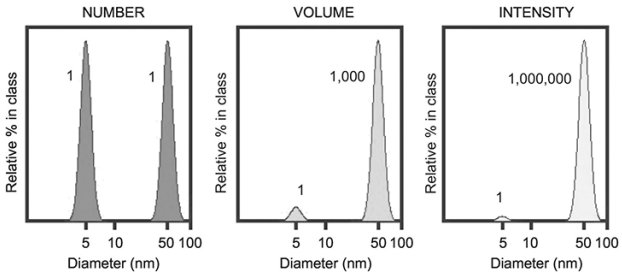

Figure 36: Number, volume and intensity distributions of a bimodal mixture of mean particle size 5 and 50 nm in equal number density. Figure copied from Ref.[67].

2.7.3 Magnetometry: electromagnetism

The movement of the charged particles and interactions with mutual charged particles is related to Ampere's law from which is stated that the magnetic field is proportional to the current and inversely proportional to the distance.[8, 10] The magnetic field is generated by a closed loop of current-carrying wire passing through the loop. The appearance of a closed loop indicates a contour integral and can therefore be expressed as:

$$\oint \boldsymbol{HdL} = \sum_{i=1}^{N} I_i \tag{18}$$

- H is the applied magnetic field ($A \cdot m^{-1}$).
- I is the current of the flowing electrical field (A).
- L is the length of the coil (m).

The concept can be simplified by inducing a magnetic field by passing an electric field a number of turns through a coil of metal wire in a single direction. The magnitude of the magnetic field can then be expressed as[8]:

$$H = \frac{NI}{L} \tag{19}$$

where N is the number of turns (AU).

The response of the material is the magnetic induction by applying a magnetic field. In vacuum, the magnetic induction and applied magnetic field differ by the permeability constant from which the following equation holds[8]:

$$\mathbf{B}_{ext} = \mu_0 \mathbf{H} \tag{20}$$

- $\mathbf{B}_{ext}$ is the magnetic induction ($Tesla = N \cdot A^{-1} \cdot m^{-1}$).
- H is the applied magnetic field strength ($A \cdot m^{-1}$).
- μ_0 is the permeability of vacuum ($4\pi \cdot 10^{-7} N \cdot A^{-2}$).

The types of magnetism can be distinguished from each other by the dimensionless, magnetic susceptibility of the compound, χ. The change in magnetic field due to the material is denoted as the magnetic induction of the material, B_{sample}.

$$\mathbf{B}_{sample} = \mu_0 \chi \mathbf{H} \tag{21}$$

where the magnetization, $\mathbf{M} = \chi \mathbf{H}$, is the change in magnetic field due to the sample in $A \cdot m^{-1}$. When applying and altering the magnetic field, the response of the material comes on top of the external field from which the expression below follows,

$$\mathbf{B}_{tot} = \mathbf{B}_{ext} + \mathbf{B}_{sample} = \mu_0(\mathbf{H} + \mathbf{M}) \tag{22}$$

From this relation, magnetization curves are obtained. The type of magnetism can be extracted from the magnetization curves that are illustrated in Figure 37.

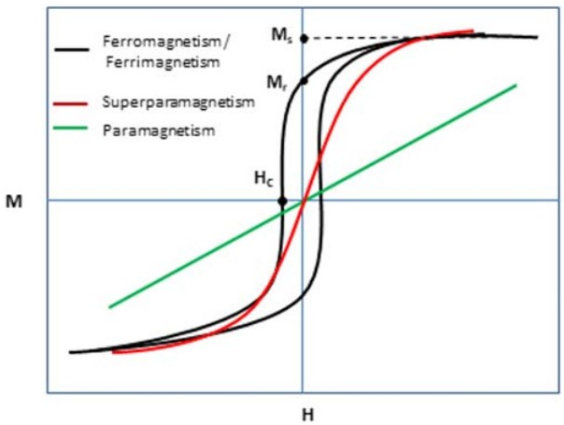

Figure 37: Schematic representation of magnetization curves of different types of magnetic materials. The values of saturation magnetization (M_s), retentivity (M_r), and coercivity (M_c) vary with the type of the material. Figure copied from Ref.[68].

The differences in the curves are the consequence of the magnetic alignment of the magnetic dipole moment, i.e., the spins. The stronger the alignment of the spins, the stronger the magnetization and therefore the magnetism. In addition, the magnetic susceptibility can be indicated as the slope of the magnetization curve. The larger the magnetic susceptibility, the steeper the slope and therefore the stronger magnetism as well.[68, 69] Ferro- and ferrimagnetic materials are considered as the strongest which is shown by the black magnetization curve. Ferro- and ferrimagnetic materials also have the property to have a hysteresis since the alignment is retained even when the applied field is removed and therefore the magnetic material remain to have a magnetic moment. A paramagnetic material shows a linear curve indicating a weak, magnetic field dependent magnetization. Diamagnetic material can be proposed to have a magnetization curve like paramagnetic materials but the curve reflects in the y-axis indicating a negative slope, $\chi < 0$, due to the alignment of the spins in opposite direction to the applied magnetic field.

2.7.3.1 Vibrating-sample magnetometry

Vibrating-sample magnetometry (VSM) is a versatile technique for measuring the magnetic moment of a sample when it is vibrated perpendicularly to a uniform magnetizing field.[70] The VSM technique is used to obtain the magnetic moment information of samples based on Faraday's law of magnetic induction. Faraday's law describes the electromotive force. The produced electrical potential when altering the magnetic field.[71, 72, 73] The difference in potential tends to give rise to an electric current and is measured in volts.

$$\varepsilon = -N\frac{d\overrightarrow{\phi_B}}{dt} \tag{23}$$

- ε is the electromotive force ($V = J \cdot C^{-1}$).
- N is the number of turns of the coil (AU).
- ϕ_B is the change in magnetic flux ($Tesla \cdot m^2$).
- t is the change in time (s).

A magnetic sample is mounted on the sample holder and placed between two electromagnet poles as shown in Figure 38. The position of the sample holder can be altered to its equilibrium position where the output signal is independent of small displacements of the sample in any direction.[74] This equilibrium position is called the "saddle point," which is determined by positioning calibration prior to the measurements.[75, 70]

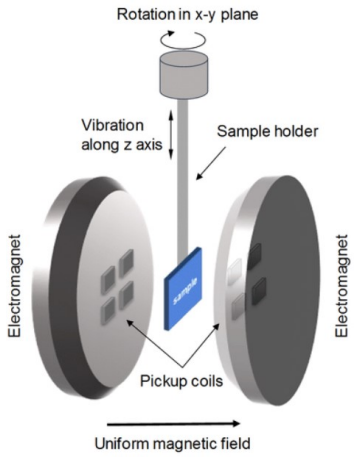

Figure 38: Schematic representation of VSM system. Figure copied from Ref.[75].

During measurement, the sample is subjected to a constant vibration vertically at a fixed frequency. The

changing magnetic induction, which is proportional to the magnetic moment in the sample, causes an AC voltage induction to be detected by a set of pickup coils placed near the electromagnetic poles.[75, 70] A magnetic induction change is detected when the applied magnetic field, coil position, or sample position is changed. The induced voltage is then fed into a lock-in amplifier to obtain the magnetic moment information of the sample.[75, 70]

2.7.4 UV-Vis spectroscopy

The absorption of light is an interaction that takes place on the atomic or molecular scale. During the absorption process, a photon is absorbed by the atom or molecule meaning that a fraction of light from the source is 'lost'. A light bundle of a certain wavelength passes through a substance that absorbs radiation of this wavelength will therefore decrease in strength.

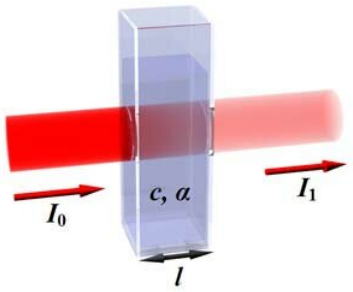

Figure 39: Diagram of Beer–Lambert absorption of a beam of light as it travels through a cuvette of width l. Figure copied from Ref.[76].

The law of Lambert-Beer is a relationship between the attenuation of light through a substance and the properties of that substance.[77] This relation explains the phenomena and is illustrated in Figure 39. From the left side, a light bundle with an initial intensity, I_0, enters a liquid containing a concentration, c, of an absorbing substance. The absorption ensures that the intensity at the spot, I, decreases. This quantity is proportional to the concentration of the absorbing substance and involves that an increase in present absorbing molecules increases the absorption decay. The absorbance is proportional to the molar absorpbtion coefficient of the substance, α, and the path length, l, over which the beam travels. This yields the expression,

$$A = -\log\left(\frac{I}{I_0}\right) = \alpha \cdot c \cdot l \tag{24}$$

- A is optical density (*dimensionless*).
- α is molar extinction coefficient of the compound ($L \cdot mol^{-1} \cdot cm^{-1}$).
- c is concentration of the compound ($mol \cdot L^{-1}$)
- l is optical path length (cm).
- I_0 and I are incident and transmitted light intensity ($J \cdot m^{-2} \cdot s^{-1}$).

Since magnetic fluids are concentrated colloidal solutions consisting of magnetic nanoparticles in water or organic liquids, the stability of the system and its aggregation stability are important to take into account. The aggregation stability can be provoked by changing the concentration of the fluids at their dilution that in turn can involve the change of the absorption spectra of the investigated magnetic dispersions.[78] A

similar expression can be maintained of Lambert-Beer when incident light depends on the spectral absorption coefficient (or index)[78, 79],

$$I(l) = I_0 e^{-k_\lambda \cdot l} \tag{25}$$

- I_0 and I are incident and transmitted light intensity ($J \cdot m^{-2} \cdot s^{-1}$).
- k_λ is spectral absorption coefficient (or index) of the wavelength, λ (cm^{-1}).
- l is optical path length (cm).

The spectral absorption index depends on the wavelength (in m) of light and is equal to [78, 79],

$$k_\lambda = \frac{4\pi \cdot k}{\lambda} \tag{26}$$

where k denotes the dimensionless absorption factor.

By enhancing the wavelength, the spectral absorption index decreases and the value of transmitted light approaches the value of incident light indicating that the light fully passes through the sample, i.e., absorption decreases. By lowering the wavelength, the spectral absorption index increases and the value of transmitted light approaches zero indicating that the light does not pass through the sample, i.e., absorption increases.
Furthermore, the light attenuation cross section is an individual constant characteristic of a particle, showing the light attenuation introduced by one particle which represents the extinction, σ_{ext}. It consists of the scattering cross section, σ_{sca}, and absorption cross section σ_{abs} [78, 79],

$$\sigma_{ext} = \sigma_{sca} + \sigma_{abs} \tag{27}$$

For dispersions with small particle size compared to the wavelength of light, the Rayleigh approximation is applicable and the cross sections can be described by the following equations [78, 79],

$$\sigma_{sca} = \frac{8}{3}\left(\frac{2\pi a}{\lambda}\right)^4 \left|\frac{(\tilde{m}^2 - 1)}{(\tilde{m}^2 + 2)}\right| \tag{28}$$

$$\sigma_{abs} = \frac{8\pi a}{\lambda} Im\left(\frac{(\tilde{m}^2 - 1)}{(\tilde{m}^2 + 2)}\right) \tag{29}$$

where a is the particle radius, m is the refractive index of the particle and $\tilde{m}$ is the relative complex refractive index of particles with respect to the liquid phase,

$$\tilde{m} = m + ik \tag{30}$$

$$k = \frac{\varepsilon''}{2m} \tag{31}$$

$$\tilde{\varepsilon} = \varepsilon' + i\varepsilon'' \tag{32}$$

where $\tilde{\varepsilon}$ is the effective dielectric constant. The real part (ε') represents how much energy is stored (absorption of light in a particle, described by the refractive index), while the imaginary part (ε'') is a measure of how dissipative or lossy a particle is to absorption of light (loss of absorption, described by the absorption coefficient in the Lambert-Beer law).[80, 81, 82]
The expression for σ_{abs} shows that the absorption is proportional to the size of the particles in the dispersion: the larger the size, the greater the absorption but the scattering of light by a particle also increases with increasing size of the particle.
Based on the extinction efficiency of nanoparticles, the extinction coefficient of a nanoparticle can be determined using the following equation[79, 82],

$$\sigma_{ext,NP} = \frac{3\pi\phi_v}{4a} \cdot \sigma_{ext} \tag{33}$$

with ϕ_v and a as the volume fraction (%) and size (m) of the nanoparticle, respectively.

For dispersions, scattering is usually insignificantly small if the particles are uniformly small. In practice, dispersions are polydisperse and contain aggregated as well as agglomerated particles. If scattering is ignored, the attenuated light is assumed to be absorbed and thus the spectral absorption coefficient is simply the absorption coefficient. The total extinction coefficient of the dispersion can be determined by combining the extinction coefficient of the nanoparticle and the spectral absorption coefficient [79],

$$\sigma_{ext,disperion} = \frac{3\pi\phi_v}{4a} \cdot \sigma_{ext} + \frac{4\pi \cdot k}{\lambda} \tag{34}$$

Therefore, dispersions are independent of the extinction in the presence of distributed particles at nano-size if scattering is not considered ($\sigma_{ext} = \sigma_{abs}$). If aggregates and agglomerates are present, the scattering affects the extinction. The extinction of the dispersion is then proportional to the particle size and increases due the increase in particle size according to Eq. 34 where $\sigma_{ext} = \sigma_{sca} + \sigma_{abs}$.

2.8 Magnetic sedimentation

The concentration of ferrofluids remains relatively homogeneous in external fields because magnetic sedimentation is rapidly balanced by a friction force of the particles.[2] The interactions between particles are neglected due to the assumption of ideal particles. That being the case, a steady state can be set up by enumerating the involved forces regarding gravity, frictional, osmosis, and magnetophoresis. In the case of stationary state, the following equation holds:

$$F_{mag} + F_g = F_{osm} + F_{fric} \tag{35}$$

with

Magnetic force: $F_{mag} = m_d \cdot L(\boldsymbol{B}(h)) \cdot \frac{d\vec{B}(h)}{dh}$
Gravitational force: $F_g = -\Delta\delta \cdot V_{NP} \cdot g$ (with the mass density, $\Delta\delta = \Delta\delta_{NP} - \Delta\delta_{dispersant}$)
Osmotic force: $F_{osm} = \frac{dc(h)}{dh}\frac{k_B T}{c(h)}$
Frictional force: $F_{fric} = 6\pi\eta a_H \upsilon$

For the expression of the magnetic force, the dipole moment of the nanoparticles, m_d, is the same variable as described in Eq. 1 since the dipole moment considers the multiplication of the magnetic volume for a spherical particle with the bulk magnetization. Furthermore, $\frac{dB(h)}{dh}$ represents the magnetic field gradient at height, h. $L(B(h))$ describes the average degree of magnetic alignment of magnetic particles and can be

formulated as the ratio of average magnetization in the field direction x to the magnetic dipole moment is indicated as $\frac{<m_x>}{m_d}$. Expanding the expression gives the additional variables[2],

$$L(B(h)) = \frac{< m_x >}{m_d} = coth\left(\frac{m_d \cdot B_x(h)}{k_B T}\right) - \frac{k_B T}{\mu_d \cdot B_x(h)} \tag{36}$$

The gravitational force can be neglected, since it is smaller than the magnetic force by 2 orders of magnitude ($F_{mag} >> F_g$) when considering the customized set-up when considering magnetophoresis of a ferrofluid in a closed cuvette. The osmotic force counteracts magnetophoresis. The expression for the osmotic force consist of the particle number concentration, $c(h)$, and considers the concentration gradient, $\frac{dc(h)}{dH}$, since the particles tend to restore a uniform concentration during the sedimentation process. If this backflow (back-diffusion) effect is strongly dominated by the magnetic force ($F_{mag} >> F_{osm}$) due to the presence of aggregation, then the osmotic force can be neglected as well.[2, 83] The frictional force opposes the magnetic force due to the Stokes drag of the viscosity, η, on the particle with hydrodynamic radius, a_H that also affects the average magnetophoretic velocity, v.
The expressions for the magnetic, osmotic and frictional force can be combined to obtain an expression for the average magnetophoretic velocity of the magnetic particles.

$$v(h) = \frac{m_d \cdot L(B(h)) \cdot \frac{d\vec{B}(h)}{dh} - k_B T \frac{dc(h)}{dh} \frac{1}{c(h)}}{6\pi\eta a_H} \tag{37}$$

Theoretically, the expression can be applied to compute time-dependent concentration profiles numerically by starting from a homogeneous concentration profile and computing the number particles transferred between neighboring segments, $n(h)$, in discrete time steps dt[2]:

$$n(h) = \frac{v(h) \cdot c(h)}{dh} \tag{38}$$

Since the closed system and the position of the external magnetic field steer the magnetic particles in a single direction, the particles cannot flow out of the system and the total number of particles is retained throughout the simulation.[2] Alternatively, the average magnetophoretic velocity by considering the concentration-weighted average particle height, $< h >$, for the obtained concentration profiles at the maximal and minimal height, h_{max} and h_{min}, respectively[2]:

$$< h > = \frac{\int_{h_{min}}^{h_{max}} c(h) \cdot h \cdot dh}{\int_{h_{min}}^{h_{max}} c(h) dh} dt \tag{39}$$

Subsequently, time steps can be taken to monitor the rate that the average particle height alters to obtain the average magnetophoretic velocity by interpreting the following.
The time derivative of $< h >$, the absorbance-weighted or concentration-weighted average height, is equal to the average sedimentation rate at the start of the experiment[2]. This average velocity starts at the initial position with height h_0. As time, t, progresses, $d < h > /dt$ decreases in magnitude due to a fraction ft of particles of a given size accumulating in the sediment, so that a fraction $(1 - ft)$ of particles remains in a column of height $(1 - ft)h_0$ above the sediment. The concentration-weighted average height of this column is $(1 - ft)h_0/2$. The concentration-weighted average height of the entire sample, including sediment, is thus given by $(1 - ft)^2 h_0/2 = [1 - 2ft + (ft)^2]h_0/2$, which evolves with sedimentation rate fh_0 in the limit of small ft. The bottom is reached when $ft = 1$ but the presence of back-diffusion causes the system to reach a magnetophoretic-diffusion equilibrium.
When the concentration profile is far from equilibrium and back-diffusion can be neglected, the magnitude of the particle hydrodynamic size can be determined by balancing the magnetic and frictional force[2]:

$$F_{mag} = F_{fric} \tag{40}$$

$$\mu_0 m_d \frac{dH}{dh} = 6\pi\eta a_H v \tag{41}$$

$$a_H \cong \sqrt{\frac{9\eta\overline{v}}{2m_{bulk}\mu_0 \frac{dH}{dh}}} \tag{42}$$

with $m_d = V_{NP} \cdot m_{bulk} = \frac{4}{3}\pi(a_{NP})^3 \cdot m_{bulk}$, for a spherical nanoparticle

Note that this expression for the magnetic force represents full magnetic alignment of nanoparticle dipoles with an external field gradient on a nanoparticle and the assumption that the size of the magnetic nanoparticle equals the hydrodynamic size ($a_{NP} = a_H$).

3 Materials and methods

3.1 Chemicals

For the preparation of YAG seeds and YIG-NPs, yttrium acetate (Batch no: MKCJ7210, Prod. no.: 1003051841) and aluminium isopropoxide (Batch no: MKCM4214, Prod. no.: 102301548) were purchased from Sigma-Aldrich. In addition, iron (III) acetylacetone (Batch no.: A0265578, Prod. no.: 119131000) was purchased from Acros Organics. For the reaction medium, 1,4-butanediol was purchased from Acros Organics (Batch no: A0429753, Prod. no.: 107630010) and diethylene glycol from Sigma-Aldrich (Batch no.: BCBF4248V, Prod. no.: 101132297). For surface modification of the YIG-NPs, oleic acid was purchased from Aldrich (Batch no.: MKBG6040V, Prod. no.: 364525). Cyclohexane (Batch no.: 1551740, Prod. no.: 176810025) and n-dodecane (Batch no.: 1551740, Prod. no.: 176810025) were purchased from Arcros organics and Thermo scientific, respectively. Ethanol was purchased from VWR chemicals (Batch no.: Z3K244006, Prod. no.: 83813.360).

For the preparation of maghemite ferrofluid, iron (II) chloride tetrahydrate (Batch no.: BCBX4953, Prod. no.: 44939-250G) and iron (III) chloride hexahydrate (Batch no.: BCCB8808, Prod. no.: 44944-250G) were purchased from Sigma Aldrich sodium hydroxide (Batch no.: B1317998645, Prod. no.: 1.06498.1000) was purchased from Merck KGaA and citric acid (Batch no.: BCBF5362V, Prod. no.: 27487-250G-F) was purchased from Sigma Aldrich. For this experiment, MilliQ water was used (18.2 $M\Omega \cdot cm$ at 20 °C).

For the preparation of maghemite ferrofluid, nitric acid (Batch no.: K48570356650, Prod. no.: 1.00456.1010) was purchased from Merck KGaA, Iron(III) nitrate nonahydrate (Batch no.: A0381122, Prod. no.: 202492500) was purchased from Acros organics. Trisodium citrate (Batch no.: AM1413148014, Prod. no.: 1.06448.0500) and sodium chloride (Batch no.: K52782804134, Prod. no.: 1.06404.1000) were purchased from Sigma Aldrich. For this experiment, MilliQ water was used (18.2 $M\Omega \cdot cm$ at 20 °C).

3.2 Methods

3.3 Preparation of magnetite and maghemite ferrofuid

Magnetite dispersion was prepared by co-precipition in basic environment. Maghemite ferrofluid was prepared from magnetite dispersion. For magnetite ferrofluid, 0.1 M Fe ion solution was prepared by dissolving 674.5 mg of $FeCl_2.4H_2O$ and 1811.9 mg of $FeCl_3.6H_2O$ in 100.51 mL of MilliQ water while stirred. Next, a 0.57 M NaOH (aq) stock solution was prepared by dissolving 2.44 g of NaOH in 107.05 mL of MilliQ water. Eleven batches were prepared containing 500 µL Fe ion solution and 500 µL of 0.57 M NaOH solution. A 0.32 M citric acid stock solution was prepared by dissolving 4.95 g of citric acid in 80.10 mL of DI. Different fractions of 0.32 M citric acid were added to the series of batches with increasing citric acid concentration. These fractions were series of 0, 100, 130, 150 - 310 μL (steps of 20 μL). The magnetic and colloidal properties were observed regarding the stability and magnetic behaviour of the series of batches.

For maghemite ferrofluid, 1.28 g of $FeCl_2.4H_2O$ and 3.46 g of $FeCl_3.6H_2O$ were prepared in 80.23 mL of MilliQ water. Another NaOH (aq) solution was prepared containing 2.11 g of NaOH in 20.12 mL of DI and added to the prepared iron chloride solution under magnetic stirring for 15 minutes. The obtained sediment was gathered using a hand-held magnet and the supernatant was poured off. Subsequently, 16 mL of 2M HNO_3 solution was added to the magneic sediment. In addition, a solution containing 3.46 g of iron(III) nitrate nonahydrate in 24.35 ml of DI was added to the dispersion. The dispersion was placed in an oil batch and refluxed under stirring at 96 °C for 45 minutes. After refluxing, the formed magnetic particles were gathered using a hand-held magnet and the supernatant was poured off. The magnetic sediment was washed three times with 2M nitric acid (aq). After washing, the sediment was redispersed in 10 of mL DI. In addition, 6 mL of 1M trisodium citrate was added to the dispersion and the dispersion was refluxed again under stirring at 96 °C for 20 minutes. After refluxing, the formed magnetic particles were gathered using a hand-held magnet and the supernatant was poured off. The sediment was redispersed in acetone. Again, the magnetic particles were collected using a hand-held magnet and the acetone was poured off. The sediment was redispersed in 10 mM NaCl (aq) and again, the supernatant was poured off after the magnetic particles

were collected using a hand-held magnet. The washing procedure of redisersing in acetone and 10 mM NaCl (aq) was repeated two more times. After washing the magnetic particles, the magnetic particles were purged with nitrogen gas for 30 minutes. The the dried, magnetic particles were redispered by adding 10 mL of 10 mM NaCl (aq) in batches of 1 mL using a glass Pasteur pipette under controlled agitation in a 20 mL glass bottle.

3.4 Synthesis of YAG seeds and YIG-NPs

For the synthesis of YAG seeds, the precursors consist of 672.3 mg (= 2.5269 mmol) anhydrous yttrium acetate and 860.2 mg (= 4.2115 mmol) of vacuum destillated aluminium isopropoxide were mixed using a mortar in the stoichiometric ratio of $Y/Al = 3/5$. The solid mixture was added to 18 mL of reaction medium containing 16.2 mL of 1,4-butanediol (1,4-BD) and 1.8 mL of diethylene glycol (DEG). The obtained reaction mixture was stirred while purging with nitrogen gas for 15 minutes. The reaction mixture in the glass tube was placed in a preheated stainless steel autoclave system (Carl Roth®).
The preheat temperature was 100 °C for 30 minutes and was set to 300 °C for 3 hours. After the solvothermal treatment, the system was cooled by immediately transferring the metal autoclave tube into an ice-bath until atmospheric pressure was reached. The formed YAG dispersion was subjected to an ultrasonic treatment for 10 min and centrifuged at 3750 rpm (3270g) for 30 min. The obtained YAG seed dispersion was collected by carefully transferring the supernatant in another centrifugal tube.

By determining the YAG seeds concentration, seeded growth of YIG-NPs was executed. The precursors consist of 1197 mg (= 3.3880 mmol) of iron acetylacetone and 540.8 mg (= 2.0328 mmol) of dried yttrium acetate were mixed in stoichiometric ratio of $Y/Fe = 3/5$. The solid mixture was dissolved into a solvent containing 36 mL of 1,4-butanediol and was purged with nitrogen gas for 15 minutes. The reaction mixture in the glass tube was placed in the preheated autoclave tube (same condition used as for YAG seeds) and closed after the reaction mixture was purged with nitrogen. The temperature was set for 300 °C for 7 hours and afterwards cooled down at room temperature. The obtained YIG dispersion was transferred into a 50 mL centrifuge tube (Brand: VWR) and subjected to an ultrasonic treatment for 10 min. Centrifuge was applied at 3750 rpm (3270g) for 10 min and obtain the YIG dispersion by carefully collecting the supernatant in another 50 mL centrifugal tube.

3.5 Preparation of YIG ferrofluid by surface modification

Surface modification was done in a 20 mL glass bottle by pipetting 5 mL of the sample in in 10 mL of MilliQ water and one droplet concentrated ammonia was added using a glass Pasteur pipette. The glass bottle containing the dispersion was placed on a hand-held magnet for 1 hour to collect the YIG-NPs. The supernatant containing the impurities was poured off and the magnetic sediment was redispersed in 10 mL of MilliQ water and again placed on a hand-held magnet for 15 minutes. The separation of the YIG-NPs from the supernatant and redispersion in 10 mL of MilliQ water with 15 minutes of collecting the YIG-NPs in magnetic field was repeated one more time. Subsequently, the magnetic sediment was redispersed in 10 mL of MilliQ water and 1 mL of oleic acid was added to the dispersion to obtain two liquid phases with the magnetic particles in the water phase. The sample was rotated for one hour using a roller bank to migrate the YIG-NPs to the oil phase. The oil phase that contained the YIG-NPs was separated from the water phase. Subsequently, 10 mL of ethanol was added to execute a wash step with a handheld magnet. The magnetic sediment was separated from the supernatant and redispersed in 5 mL of ethanol to perform a second wash step. The supernatant was discarded so that the magnetic sediment was dried by purging with nitrogen gas gently. The magnetic sediment was redispersed in cyclohexane to observe ferrofluid behaviour using a magnet.

3.6 Imaging and analyzing size distribution YAG seeds and YIG-NPs

TEM preparations were done by mounting a single droplet of the sample on a coated copper substrate and dry the samples for 1 day under a IR lamp. For the YIG dispersion, the samples were diluted with a factor of 10^3 and 10^5 in MilliQ water (18.2 $M\Omega \cdot cm$ at 20 °C). For the YAG seeds, 5 mL of YAG dispersion was added

to 35 mL ethanol and centrifuge at 25,000 RPM (75,600g) for 2 hours. The YAG sediment was separated from the supernatant, followed by redispersion in 5 mL of ethanol and sonication for 15 minutes. Samples were mounted on the coated substrate where the YAG dispersions were diluted with a factor of 50 and 500. The particle sizes were determined using transmission electron microscopy (Tecnai10, 100 kV).
In addition, Dynamic light scattering (DLS) was used to determine the size distribution with Zetasizer (Malvern Zetasizer Nano ZS). The dispersions were diluted such to observe transparency on macro scale and to reduce influence of scattering which was checked by an attached laser setup.

3.7 Magnetization of the ferrofluids

Magnetization curves were measured using a vibrating sample magnetometer (EZ-9 from Microsense). For the measurements of liquid samples, magnetic dispersions were placed in a vessel until the vessel was filled entirely (no presence of air bubbles) and placed on a holder by wrapping with PTFE Thread Seal tape. Calibration steps were executed with Nickel (s) as the calibration sample to ensure accuracy of the results. The steps of the calibration are shown in Appendix 9.3.1. In particular, the calibration step regarding the sample position was done before each measurement. For measurements of solids, the dispersions were dried by pipetting 1 mL on an aluminium cup from which the solid compound was obtained. A piece of scotch tape was used to mount the solids knowing the mass of the solids and wrapped the sample with that piece of tape. The taped solids were placed on holders and wrapped with tread seal tape to execute the measurement.

3.8 Magnetophoretic ability of ferrofluids

The ferrofluids were diluted to ensure an observable concentration gradient. A neodymium magnet of 30 mm thickness and 45 mm diameter (Supermagnete GmbH) was placed in front of the camera (Nikon D7500 connected with a photographic objective (AF-S DX Micro Nikkor 85mm f/3.5G ED VB). An empty cuvette was placed on top of the magnet and snapshots were capture to determine the optimal position where the sample is fully focused. When the optimal position was determined, five snap shots were captured without the presence of the cuvette that denoted the blanks. The cuvette was taken off from the magnet and filled with 1 mL diluted ferrofluid. Depending on the stability of the ferrofluid, a timelaps was set with a certain capture time. The timelaps and capture time increases in the stability of the ferrofluid which were a maximum of 11 hours with a capture time of 7 minutes per snap shot.
The data was computed by executing and organizing as the following. The measurements of the sample were stored in a specified 'measurement' folder that consisted of three subfolders: 'blanks', 'graphs' and text file documents as 'txt files'. The blank (or background) images were saved as Nikon Electronic Formats (NEF files) in the 'blanks' folder and consisted of pictures without sample. The pictures of the sample in the cuvette were saved as NEF files as well in the measurement folder and not in one of the subfolders. Since the picture of the sample in the cuvette contained a large data capacity, the data of the images were reduced to obtain the relevant part by inserting the region of interest (ROI) which also took up less space in the computer memory. The ROI was determined from the crop of the images. The information from the crops of the images considered the average pixel intensity for each height, for the red, green and blue channels (line color corresponds to pixel channel). The determined average pixel intensity values were implemented to obtain numerical absorbance values over time. These numerical values were saved in '.txt' files which were used for the analysis and visualization of the time-dependent absorbance profiles. The time-dependent absorbance profiles were saved automatically in the 'graphs' subfolder as .SVG (vector-based) image. From the time-dependent absorbance profiles, the concentration-weighted average height was plotted against time using Eq. 39 indicating a linear fit and a set value for the height of the image crop in mm that corresponded to the height of the dispersion in the cuvette without the meniscus. The height for all measurements of the ferrofluids was set to 8 mm. The obtained slope of the plot was denoted as the the magnetohoretic velocity and applied to determine the order of magnitude regarding the average particle size using Eq. 42. Assumed bulk magnetization values of magnetite, maghemite and YIG corresponded to 480 kA/m, 430 kA/m and 170 kA/m, respectively. The viscosity value of 1 $mPa \cdot s$ was applied for the ferrofluids in MilliQ water and cyclohexane. A viscosity value of 2.35 $mPa \cdot s$ was applied for the YIG ferrofluid in n-dodecane.

3.9 Optical density of the ferrofluids

The optical density was measured with the UV/Vis spectrometer (PerkinElmer, Lambda 365+). Ferrofluids were placed in a 10 mm quartz cuvette (Hellma analytics). The measurements were taken between 200 and 1000 nm with a scan speed of 480 nm/min and a data interval of 1 nm. The number of cycles was 1 with a cycle time of 1 second. The lamp change took place at 400 nm. The ferrofluids were measured at different dilution to observe the stability. After each measurement, the quartz cuvette was flushed with MilliQ water and ethanol followed by drying with pressurized nitrogen gas.

4 Results & Discussions

4.1 Synthesis

4.1.1 YAG seeds

For the synthesis of YAG seeds, several conditions were taken into account for finalizing the product. The difficulty for this synthesis was to obtain nanoparticles small in size due to the low stability of the dispersion. A particle with a high surface/volume ratio was required for promoting the size control regarding the synthesis of YIG-NPs. This means that the YAG seeds needed to be small YAG-NPs. In the beginning, the method of Rongjin[6] was applied. The method did yield the YAG seeds but not the desired particle size. Therefore, adjustments were done by performing additional steps. According to Odziomek[84], strongly dispersing the precursors was required for obtaining small YAG-NPs. An Ultra Turrax disperser (Figure 40 C) was applied for 15 minutes to executed the provided procedure. In addition, the amount of precursors were altered by considering 94% of the reaction medium compared to the volume Rongjin applied. The reaction medium was a composition of 90% 1,4-BD and 10% DEG. Of the reaction medium, 2 mL was used for grinding the precursors in a mortar. The mixture was transferred to the glass autoclave tube for purging with nitrogen gas under magnetic stirring before the mixture had been placed in the autoclave chamber. The residence time of the obtained reaction mixture in the autoclave system was 7 hours to ensure nucleation at 300 °C compared to the suggestion of 3 hours by Rongjin.

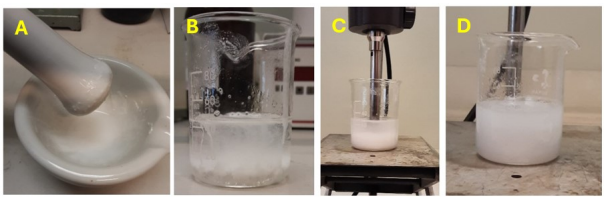

Figure 40: Steps considering dispersing the precursors in reaction medium. (A) Grinding the precursors with 2 mL DEG/1,4-BD (1:9); (B) Addition of the precursor mixture to the the remaining reaction medium. (C) Dispersing the reaction medium by using a disperser. (D) Reaction mixture after being dispersed by the disperser.

The formed YAG seeds are shown in Figure 41 including the steps considering sonication and centrifuging. The opacity of the dispersion indicated the presence of aggregated seeds. An explanation for the appearance was the residence time of the reaction mixture in the autoclave system which was extended. The increased residence time promoted the seeded growth of the seeds which resulted in large-sided, aggregated dispersion.

Figure 41: Obtained dispersion of YAG seeds by the adjusted method of Odziomek.

Therefore, the residence time was shortened to 2 hours. In addition, the stronger sonication probe system (Q500 SONICATER (Qsonica)) was applied instead of the Ultra Turrax disperser to improve the distribution of the YAG seeds. In addition, the amount of precursors and reaction medium was changed back to Rongjin's method. Figure 42 shows the formed YAG seeds. The appearance of a more transparent dispersion compared to the previous condition, assumed the presence of less aggregated YAG seeds. This can be explained by the residence time the seeds needed to execute seeded growth after nucleation. By ceasing the process in the autoclave system on time, the YAG seeds are prevented from growing further.

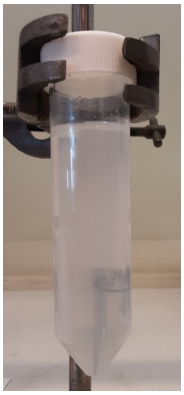

Figure 42: Obtained dispersion of YAG seeds by adjusting the residence time to 2 hours.

The observation led to further shortening of the residence time to 1 hour and 0.5 hour. The formed YAG seeds that belong to the mentioned residence time are shown in Figure 43. Figure 43 did not show improvement regarding the transparency of the dispersion and indicated that the residence times were not sufficient to induce seeded growth. It should be noted that the bulk volume of the reaction medium were different due to the low stock when executing the synthesis but must be considered as well when involving the equation for the critical radius. The critical radius to initiate nucleation is related to the bulk volume and therefore affected the product formation besides the residence time.

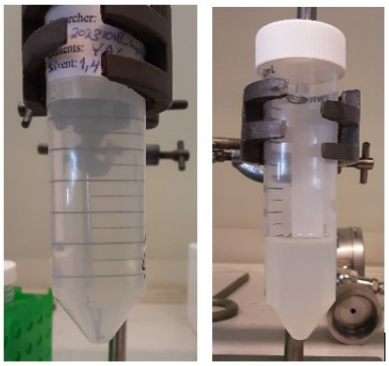

Figure 43: Obtained dispersion of YAG seeds at different residence time of 1 hour (left) and 0.5 hour (right) in the autoclave system.

In addition, the preheat step was implemented which considered the preheat temperature and the time of the autoclave system before placing the reaction mixture from the start. The applied conditions were a preheat temperature of 100 °C and 200 °C at a similar preheat time of 0.5 hour with a residence time of 2 hours after preheating (Figure 44). The corresponding Figure showed any difference between the different preheat temperatures and implied that the preheat temperature did not affect the synthesis on macro scale.

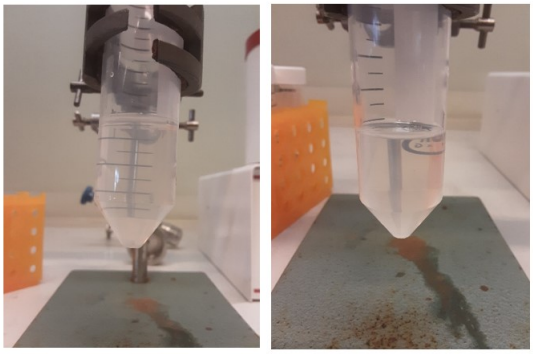

Figure 44: Obtained dispersion of YAG seeds at different preheat temperature of 100 °C (left) and 200 °C (right) in the autoclave system.

However, the presented results did not meet the expectations when the YAG dispersions were analyzed microscopically. The assumptions were that the autoclave system had not closed properly, which indicated no homogeneous temperature distribution and therefore a reduction in pressure build-up, resulting in no seeded growth. In addition, it was assumed that moisture (water content) had entered the system and affected the synthesis. The moisture could also come from the reaction medium itself, which was frequently used. The reaction medium is hygroscopic[85] and therefore could absorb moisture when used.
This brought the observation of the time-dependent temperature profile. The temperature values were obtained by setting the temperature to 0 °C and kept the pressure gauge attached to the autoclave without removing the reaction mixture. The decrease of the temperature could then be observed when the pressure was decreasing as well. Since the decrease in pressure was observed after long time intervals, three data points were managed as shown in 45A. The pressure values were captured including the times to indicate a decrease that ensures the decrease in temperature. From the captured values, an initial time and continued times were used to calculate the time differences at the corresponding temperature difference. By taking the natural logarithmic of the temperature differences against the corresponding time differences, a linear relation was plotted. The obtained slope was used to fit a time-dependent profile and was compared with the experimental

data (Figure 45B). The fit was plotted with the formula $T_{final}(time) = T_{ambient} + T_{initial} \cdot e^{(time \cdot slope)}$. The time-dependent profiles showed an overlap which indicated that the presence of moisture was not the case as well as the properly close of the autoclave system.

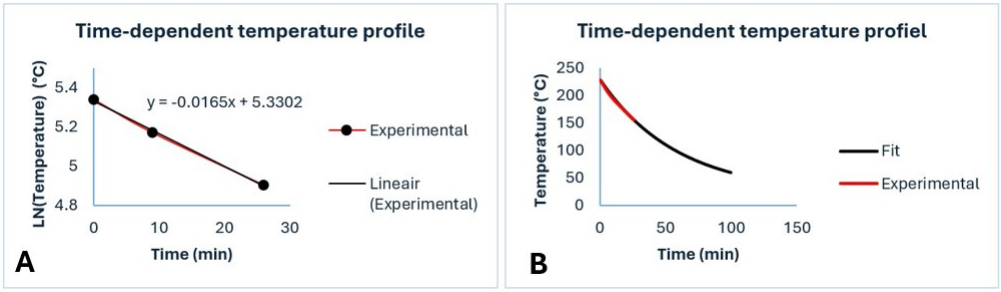

Figure 45: Time-dependent temperature profiles during cooling of the autoclave system.

In addition, IR-measurements of the reaction medium, 1,4-butanediol and diethylene glycol, were taken to ensure no presence of moisture by comparing the used compounds with the freshly bought. Figure 46 and 47 show the IR-measurements from which was observed that no moisture was present due to the overlapping peaks considering the measurements of 1,4-butanediol in Figure 46. For the used diethylene glycol in Figure 47 a small peak was present at wavenumber around 1600 cm^{-1} (denoted with a red arrow) compared to the other not used DEG that did not possess the small peak. According to the literature[86], the small peak represents the H-O-H peak and identified that there was moisture in the system. However, the peak is questionable due to its size as the peak could also indicate noise.

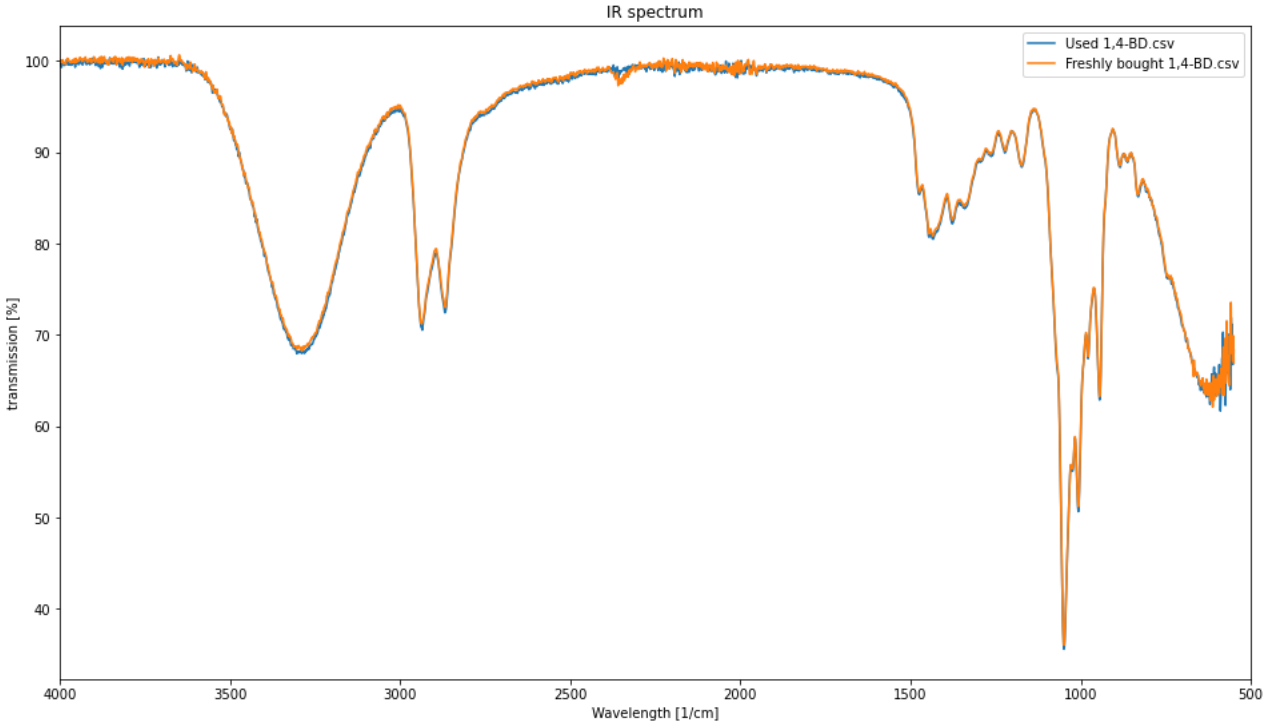

Figure 46: IR measurements of 1,4-butanediol.

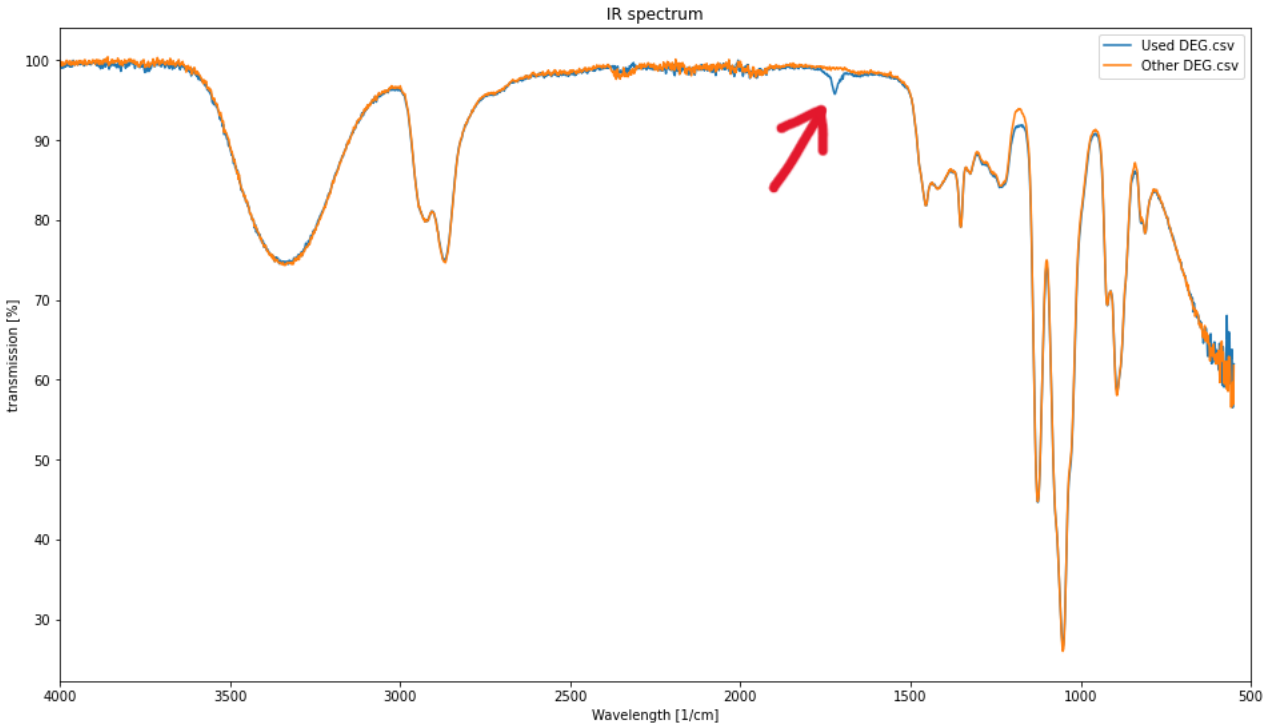

Figure 47: IR measurements of diethylene glycol.

The precursor aluminium isopropoxide was also taken into account due to the possible water content as well. That's why a simplified vacuum distillation was executed for water extraction.[87] Figure 39 shows IR-measurements of the precursor before and after the distillation process. There were several differences observed but the peaks in particular were between 1550 and 1300 cm^{-1} since these peaks identified OH bending and the peak between at 3050 and 2800 cm^{-1} identified OH stretching. A peak reduction was observed after vacuum distillation which indicated the dissolution of the precursor with moisture.

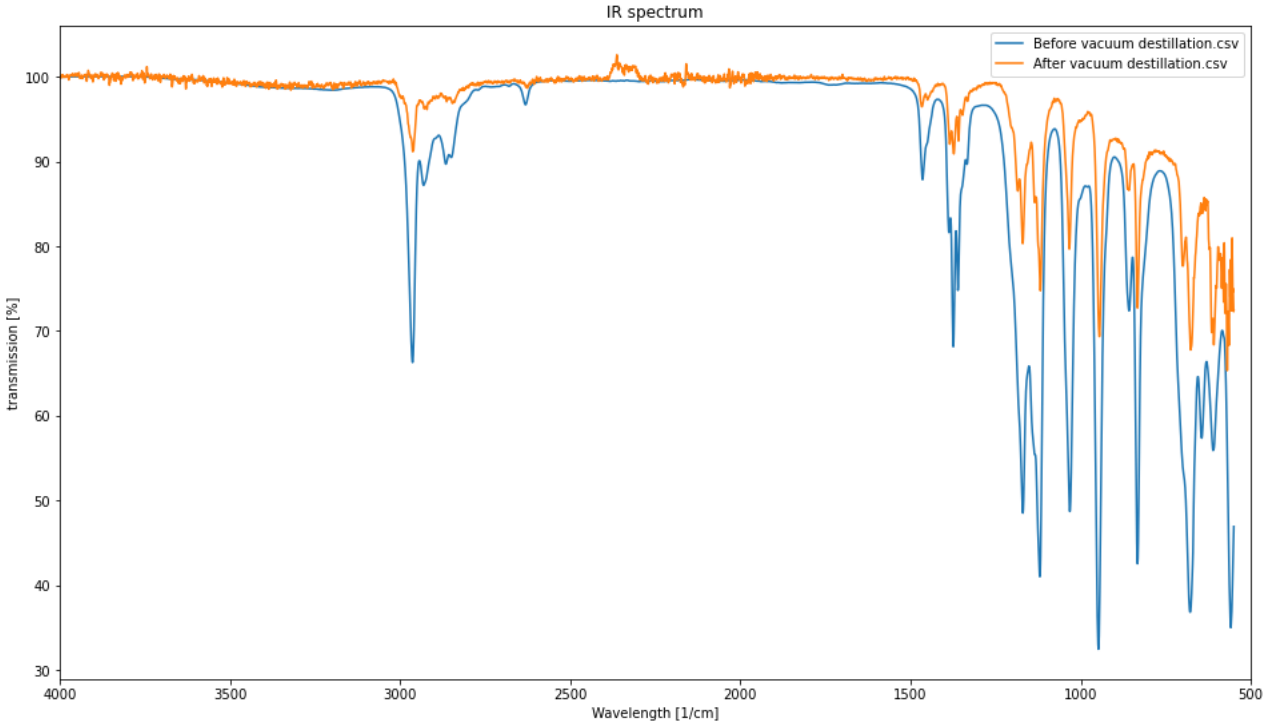

Figure 48: IR measurements of aluminium isopropoxide before and after vacuum distillation.

Furthermore, the crystallization rate was considered. This involves the time the autoclave system needed to take for cooling to room temperature. From the time-dependent temperature profile, it was assumed that the time difference between the final temperature and room temperature was sufficient to continue seeded growth of the YAG seeds. The autoclave was placed in an ice-bath to promote the crystallization rate of the YAG seeds and as a consequence interrupted further seeded growth to obtain small YAG seeds. The ice-bath is shown in Figure 49. The ice-bath step showed a decrease in particle size when considering the analyses microscopically and was for that reason included in the procedure although the dispersion showed less transparency than the previous products macroscopically. This indicated that the presence of aggregates was not excluded.

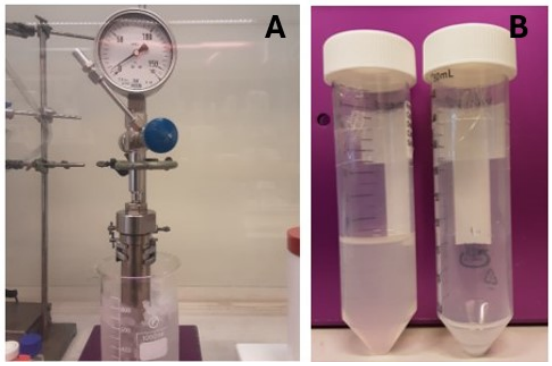

Figure 49: (A) Autoclave system in ice-bath regarding crystallization rate. (B) Product (left) is shown with the sediment (right) after centrifuging.

4.1.2 YIG nanoparticles to YIG ferrofluid

For the synthesis of YIG-NPs, a known fraction of the formed YAG seeds was added to promote seeded growth of the YIG-NPs. First, the residence time in the autoclave system was considered to ensure seeded growth of YIG onto the YAG seeds. Rongjin suggested a residence time of 3 hours but the synthesis was executed at a residence time of 7 hours and yielded to the dispersion in Figure 50. A low reaction medium volume was used due to low stock and is half of the suggested volume of Rongjin. The dispersion did not show magnetic behaviour when a handheld magnet was placed near the centrifugal tube. Since a leakage of the autoclave system was detected, no pressure build-up was observed which interrupted the heterogeneous seeded growth of YIG-NPs.

Figure 50: Obtained dispersion of YIG-NPs.

The concentration of YAG seeds was altered to observe the difference in magnetic behaviour macroscopically and yielded the dispersions in Figure 51. The Figure showed no clear color difference except for dispersion D which showed more turbidity. Dispersion B and C, corresponding to 1% and 2%, respectively, indicated strongly presence of magnetic particles whereas dispersions A and D, corresponding to 0.5% and 2% with more reaction did not show any magnetic behaviour when placing a handheld magnet. This was argued due to Rongjin's relation in Eq. 15 when considering the centrifuge procedure. Lowering the concentration of YAG seeds increased the crystallite size of the YIG-NPs. Since the YIG-NPs became heavier, the centrifuge condition forced the larger YIG-NPs to be affected by the centrifugal force and as result sedimented. When separating the sediment from the supernatant, the supernatant showed less magnetic behaviour as for dispersion A. The centrifuge condition did not affect dispersion B and C due to the formation of smaller particles that induced magnetic behaviour in large number when holding a handheld magnet. Dispersion D appeared to be green to the naked eye containing more reaction medium. The appearance was explained by the increase in reaction medium volume that promoted the seeded growth. As a result, the YIG-NPs aggregated that denoted the green color of bulk YIG which can be confirmed according to Mallmann.[88]

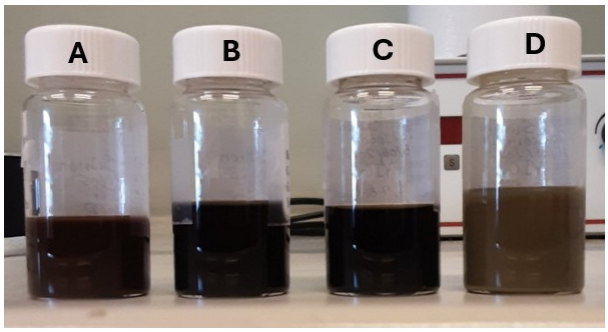

Figure 51: YIG Dispersions with different thickness YIG-on-YAG particle. (A): 0.5% YAG; (B): 1% YAG; (C): 2% YAG and (D): 2% YAG with more reaction medium.

The next step was the adsorption of ligands as stabilizing agent to obtain a YIG ferrofluid. The YIG-NPs dispersed in the water or oil phase was considered for the optimal ferrofluid behaviour. A YIG ferrofluid in the water phase was difficult due to the unstable behaviour of the YIG-NPs. The YIG-NPs were aggregated in the water phase. The addition of a stabilizing agent did not lessen the aggregates and led to phase separation. In Figure 52, fractions of citric acid were added to the dispersions in basic environment to observe the transfer to acid environment and the adsorption of citrate ligands. Figure 52 showed that after time, the particles sedimented.

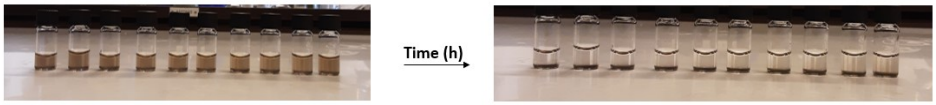

Figure 52: Coating procedure of YIG dispersions with citric acid. The initial volume consisted 500 µL of YIG dispersion and 500 µL of 0.57 M NaOH solution. The addition of 0.32M citric acid (aq) was 120 - 300 µL in steps of 20 µL from left to right.

That's why the coating procedure was executed in the oil phase. The stabilizing agent was oleic acid from which the ferrofluids below were obtained. Ferrofluid behaviour was observed due to the magnetic flow towards the handheld magnet. An explanation for the ferrofluid behaviour was the choice of stabilizing agent that lessen the aggregates.

Figure 53: YIG ferrofluid in cyclohexane (left) and n-dodecane (right).

4.1.3 Magnetite ferrofluid

The synthesis of magnetite nanoparticles involved co-precipitation. As for the coating procedure of YIG-NP in water phase, the same was applied for magnetite dispersions since the procedure was applied for stabilizing magnetite dispersions by Besenhard.[89] Figure 54 showed the behaviour of magnetite dispersions when adding different fractions of 0.32 M citric acid (aq). The initial volume of the dispersions corresponded to 1 mL by precipitating 500 µL of 0.1 M Fe solution (Fe^{2+} : Fe^{3+} = 1 : 2) with 500 µL of 0.57 M NaOH. After 1 hour, the first four magnetite dispersions sedimented, whereas the last three dispersions changed colors. This phenomenon was explained by the low concentration of the first four with the result that aggregation dominated. For the last three dispersions, the magnetic nanoparticles were dissolved and the unreacted iron ions in the solutions caused the yellow color. The black dispersions showed ferrofluid behaviour from which the dispersion with the red arrow (190 µL of 0.32 M citric acid) was denoted the strongest ferrofluid behaviour and corresponded with a ferrofluid concentration of 0.9807 g/mL.

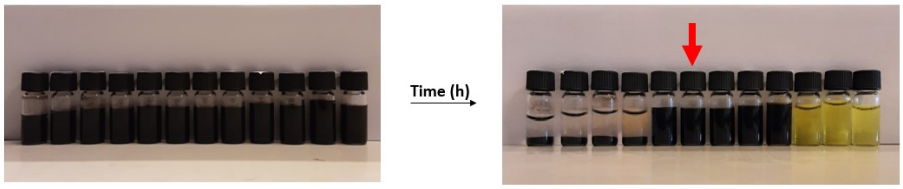

Figure 54: Coating procedure of magnetite dispersions with citric acid. The addition of citric acid was 0, 100, 130, 150 – 310 µL in steps of 20 µL from left to right.

4.1.4 Maghemite ferrofluid

From the co-precipitation to magnetite nanoparticles, the synthesis of maghemite nanoparticles was continued. The synthesis included iron ion exchange mechanism by refluxing at a 96 °C, the addition of 2 M nitric acid acid and 10 mM NaCl. The addition of the acid can be explained by the formation of positively charged maghemite nanoparticles which facilitated the adsorption of the stabilizing agent trisodium citrate. The maghemite dispersion was kept at 96 °C for 45 minutes in order to let the transformation to maghemite finish. The important part of the synthesis was the addition of NaCl (aq) during washing. Figure 55 shows the obtained maghemite ferrofluid with and without the addition of 10 mM NaCl (aq). This appearance was explained by the presence of electrical screening. The addition of NaCl (aq) created a short electrical screening that allowed large maghemite particles to approach closely where Van der Waals forces dominated and therefore resulted in aggregation. Due to the presence of the 10 mM NaCl (aq), the small particles were less affected by the aggregates to obtain a stable ferrofluid. In contrast, when 10 mM NaCl (aq) was not used, but MilliQ water was used instead, the aggregates dominated the behaviour of the magnetic dispersion. As a result, an unstable ferrofluid was formed due to the total migration of the magnetic particles to the magnet which is denoted with a red arrow in Figure 55.

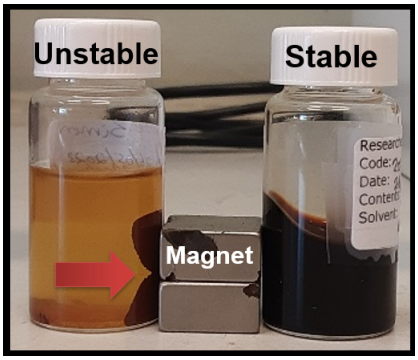

Figure 55: Obtained maghemite ferrofluids using MilliQ water (unstable ferrofluid) and 10 mM NaCl (aq) (stable ferrofluid).

4.2 Size distribution: TEM and DLS

4.2.1 YAG seeds

Besides the observation of the product macroscopically, the YAG seeds were analyzed using TEM and DLS. Difficulty was obtaining a distributed dispersion of YAG seeds with a small crystallite size of the YAG seeds. Figure 56 and 57 show the TEM and DLS analyses, respectively, of the obtained YAG seeds using method adjusted from Odziomek's method.[84] DLS analysis indicated the presence of large particles and aggregates but the problem was not observable from the TEM analysis. An explanation is the TEM preparation that needed to be adjusted.

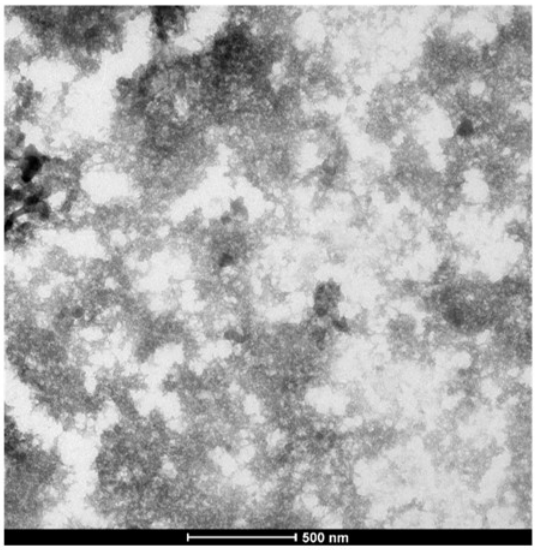

Figure 56: TEM analysis of YAG seeds using Odziomek method adjusted.

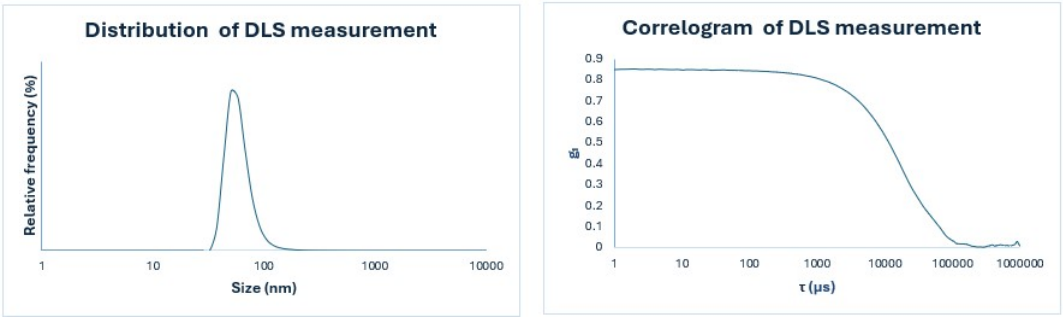

Figure 57: DLS analysis of YAG seeds (number distributed) using Odziomek method adjusted.

From the synthesis, the residence time was decreased to 2 hours and analyzed which resulted in the data below. Even though the dispersion of YAG seeds showed transparency on macro scale, the TEM and DLS analysis showed otherwise since the size distribution had a mean crystallite size of 100 nm. This indicated that the nucleation of the YAG nuclei was not finished after 2 hours. Therefore, the residence time of 1 hour and 0.5 hour did not show improvement of the nucleation process as well.

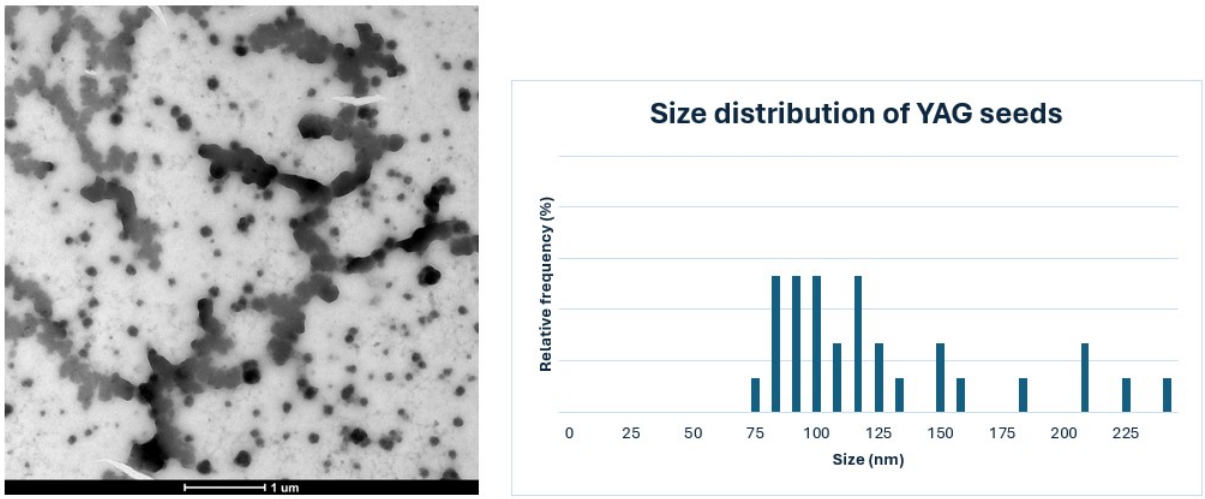

Figure 58: TEM analysis of YAG seeds using Odziomek method adjusted.

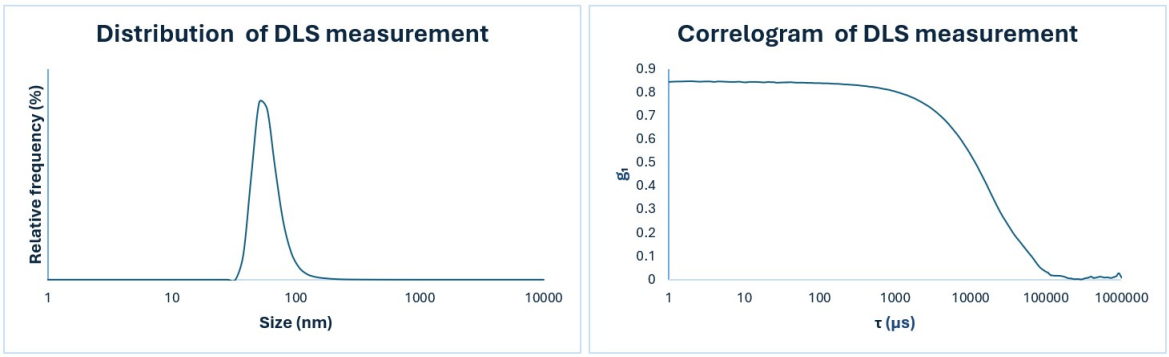

Figure 59: DLS analysis of YAG seeds (number distributed) using Odziomek method adjusted.

Since the the DLS analysis in Figure 60 did not correspond to the TEM analysis, the sonication probe was applied to reduce the polydispersity. For the use of the sonication probe, an amplitude value was chosen which denoted the vibrational energy to the system. In Figure 61. DLS was used to observe size distributions at different amplitude values of the sonication probe to obtain a comparable size distribution of the TEM analysis in Figure 60. The different amplitude power values did not change the size distribution due to the strongly bound aggregates.

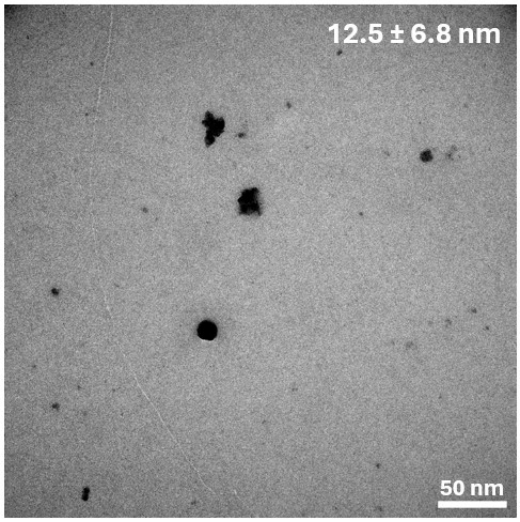

Figure 60: TEM analysis of YAG using washing agent ethanol. Since the number of particles was low, the addition of a histogram was unnecessary.

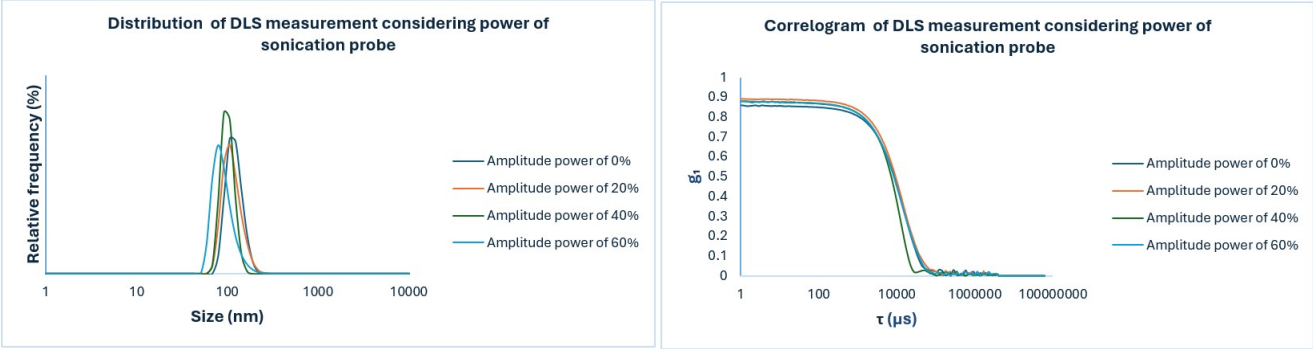

Figure 61: DLS analysis of YAG seeds (number distributed) by altering the amplitude value.

To come back on the TEM preparation, the procedure was adjusted by implementing a washing step. Washing agent of methanol was used but the use of methanol yielded in a one structured smear of presumably particles from which the methanol was not evaporated from the sample substrate. Alternatively, ethanol was used to observe a distribution of the YAG seeds and is shown. The washing procedure consisted of a two times wash with centrifuging at 20,000 RPM (60,480g) for 1 hour. In addition, several centrifuge conditions were done without applying ethanol as washing agent. These measurements were taken without transferring the sample into an different solvent meaning that the reaction medium 1,4-BD was the bulk phase. The size distribution seemed to be decreasing when increasing the residence time in the centrifuge but the decrease in size distribution deteriorated the correlogram which made the DLS measurement unreliable. The centrifugal condition is then optimal for a residence time of 30 minutes.

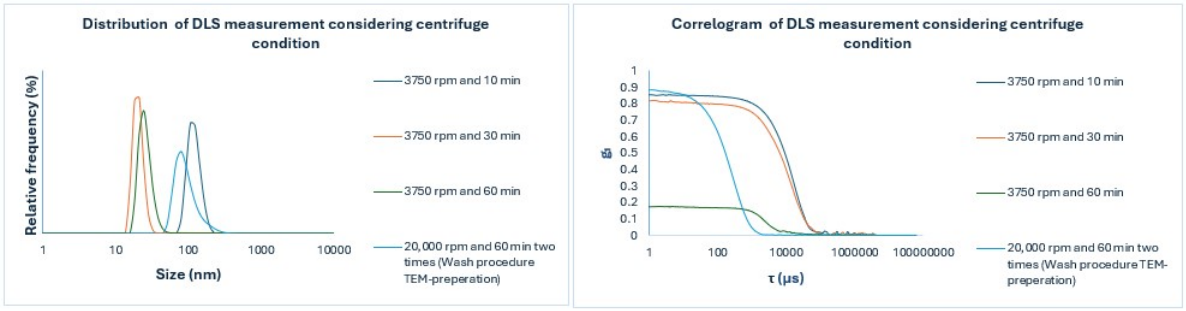

Figure 62: DLS analysis of YAG seeds (number distributed) using different centrifuge conditions including washing procedure with ethanol.

To acquire more YAG seeds for TEM analysis and increase the reliability of the DLS analysis, the wash step was altered to a one time wash with enhanced centrifugal force as well as the residence time in the centrifuge as presented in Figure 63 (TEM analysis) and 64 (DLS analysis). The centrifuge condition was increased to 25,000 RPM (75,600g) for 2 hour. From the TEM analysis, the number of observed YAG seeds was increased and the size distribution indicated a desired crystallite size but no comparable size distribution was acquired from the DLS analysis. The presence of larger particles and aggregates dominated the DLS analysis when considering the relation of the particle size with the intensity but the number weighted distribution showed the presence of more aggregates than small particles. It is therefore difficult to ensure a system with a low polydispersity.

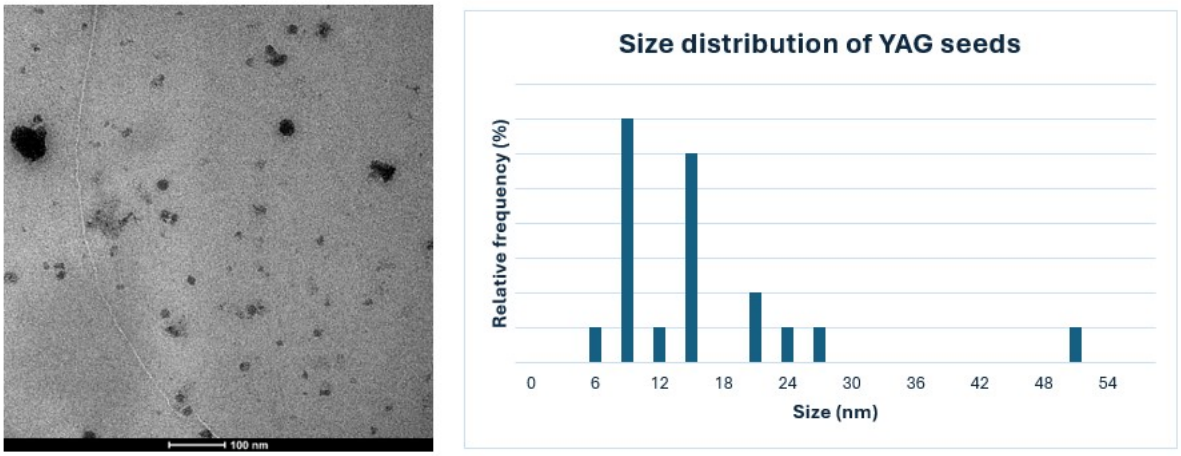

Figure 63: TEM analysis of YAG using washing step at 25,000 RPM (75,600g) for 2 hour.

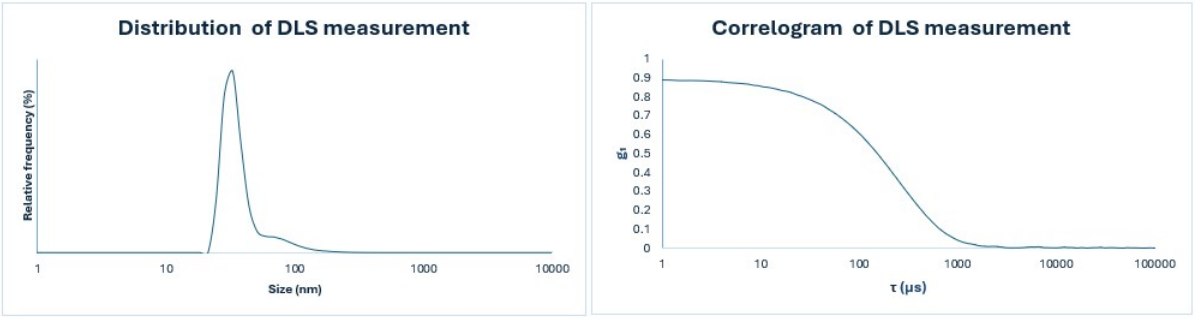

Figure 64: DLS analysis of YAG seeds (number distributed) using a wash step at stronger centrifuge condition.

The addition of an ice-bath to increase the crystallization rate and limit the seeded growth was analyzed as shown for the TEM and DLS analysis in Figure 65 and 66, respectively. The TEM and DLS analysis showed comparable results regarding the size distribution but the correlogram of the DLS indicated flaws due to the low g_1 values along the y-axis. This value represented the reliability of the experiment and was denoted as reliable if $g_1 > 0.8$. The correlogram showed low g_1 values due to the high dilution of the dispersion. The high dilution lowers the number density of the assumed small particles and therefore the g_1 values. Another argument is the absence of particles that brought unreliability in the observed correlograms and therefore the correlograms represented noise.

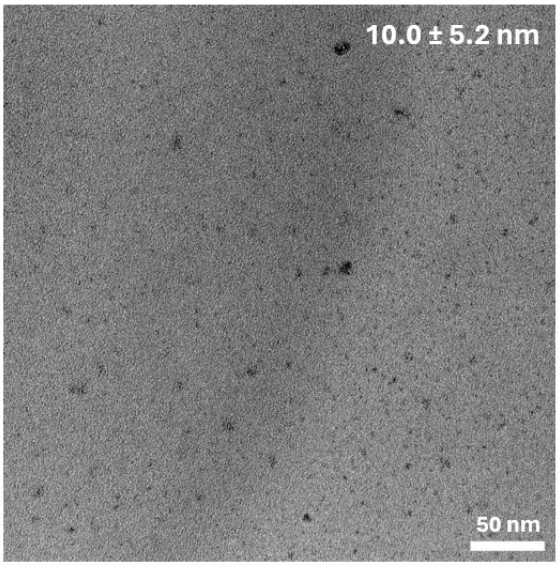

Figure 65: TEM analysis of YAG using an ice-bath. Since the number of particles was low, the addition of a histogram was unnecessary.

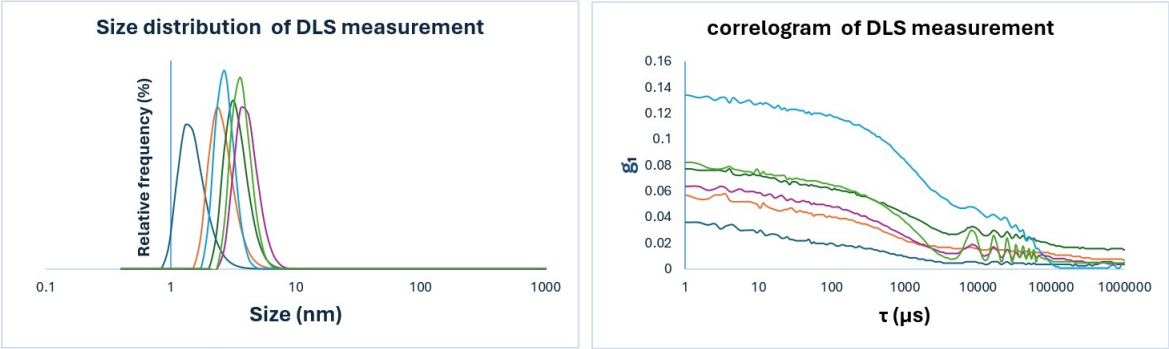

Figure 66: DLS analysis of YAG seeds (number distributed) using an ice-bath.

4.2.2 YIG nanoparticles

Since the size control of the YAG seeds was difficult manage, the crystallite size of the YIG-NPs were affected. Less measurements were taken therefore. The relation of the different TEM images of YIG-NPs by altering the concentration of YAG seeds were illustrated in Figure 67 - 70. The addition of concentration YAG seeds to form the YIG dispersion was executed by taking the desired fraction from a single YAG seed batch to observe a relation in the concentration YAG seeds with the crystallite size of the YIG-NPs. The TEM images of YIG-NPs containing 1% and 2% YAG seeds showed similarities when observing the products macroscopically (color and magnetic behaviour) and the crystallite sizes are in the same range. The TEM image that corresponds to 0.5% YAG seeds the presence of particle with a small crystallite size as expected since the magnetic behaviour was not observed macroscopically. This indicated that the large particle were centrifuged along with the aggregates as discussed in synthesis part. Figure 70 showed aggregates as expected since the dispersion was considered to be bulk YIG from which the green color appeared as discussed in the synthesis part as well. Overall, the crystallite size decreased when decreasing the mass concentration YAG. Increasing the mass concentration to 1% and 2% yielded a comparable crystallite size and the increase of the reaction volume decreases the size but causes aggregates.

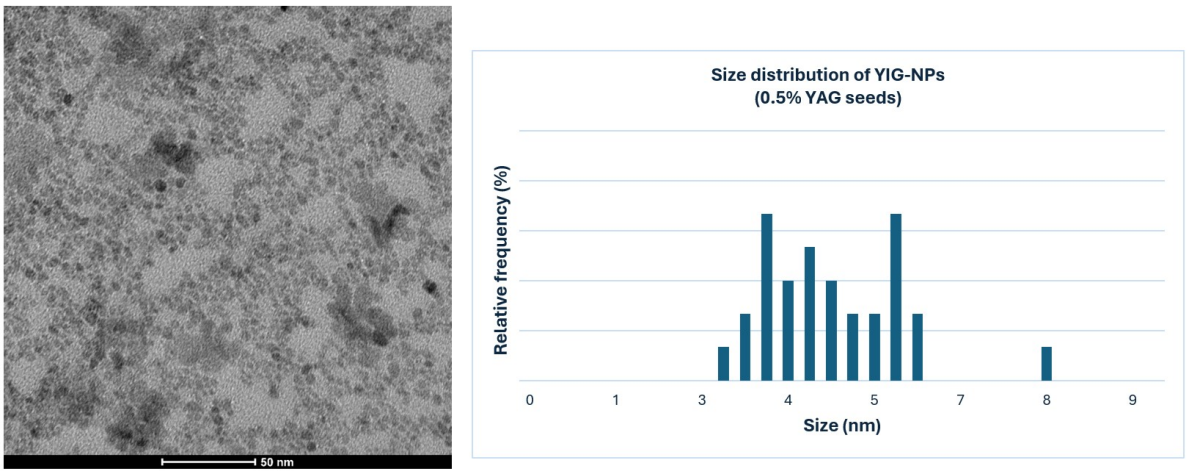

Figure 67: TEM analysis of YIG with 0.5% YAG seeds.

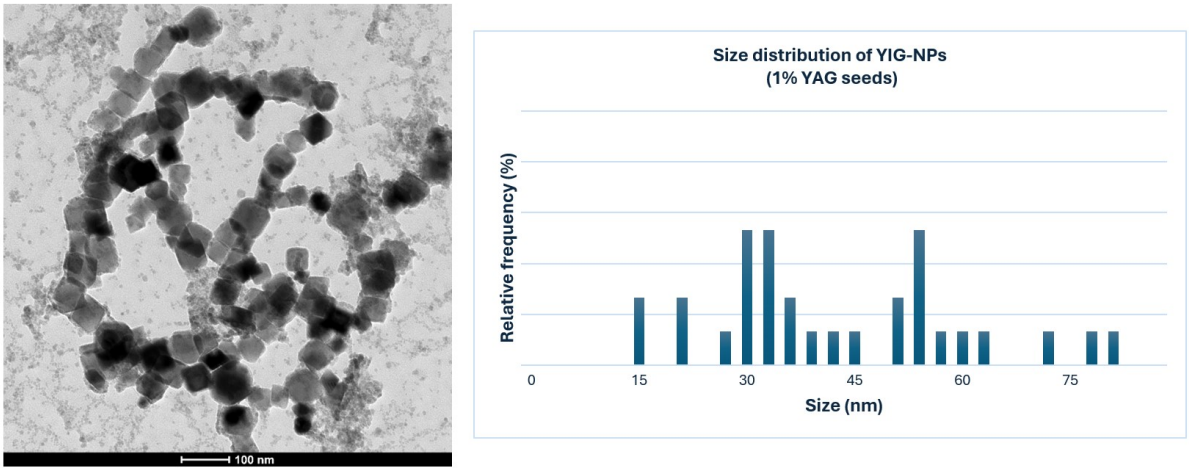

Figure 68: TEM analysis of YIG with 1% YAG seeds.

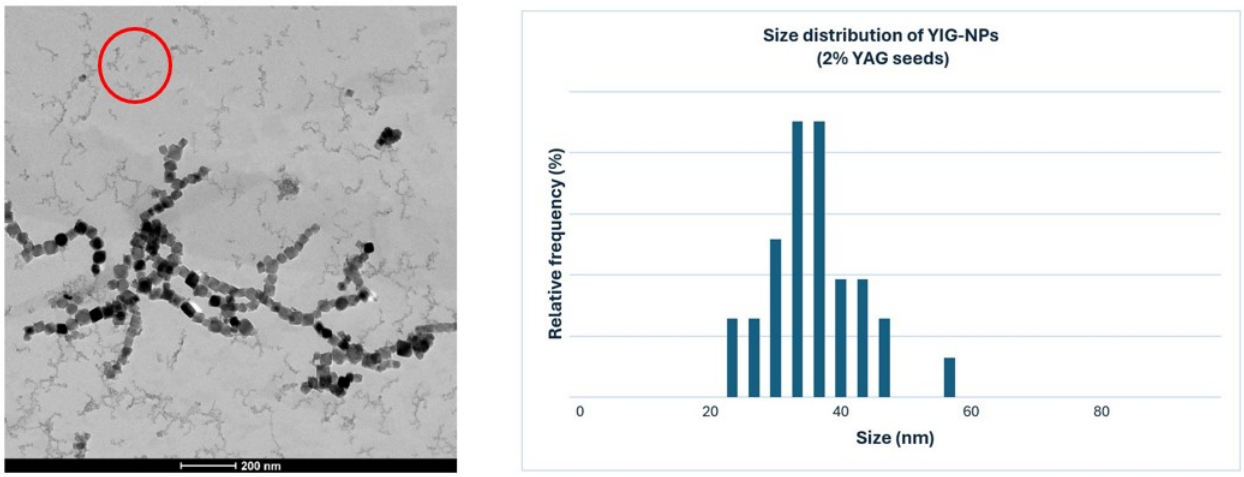

Figure 69: TEM analysis of YIG with 2% YAG seeds. Populations of small particles were not taken in the size distribution and therefore not considered in the histogram since the diameter of the small particles were not measurable (marked with red circle).

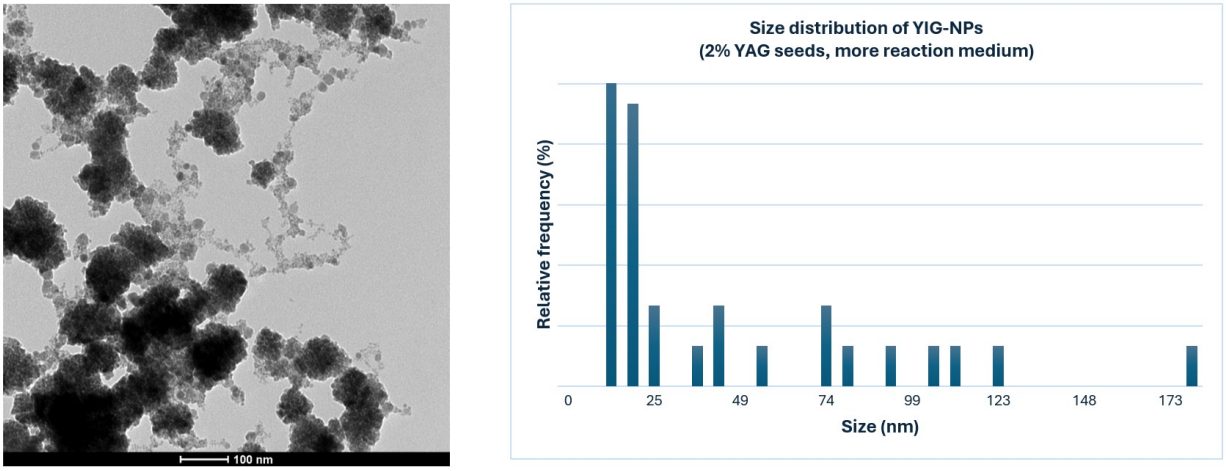

Figure 70: TEM analysis of YIG with 2% YAG seeds and more reaction medium.

4.2.3 Magnetite and maghemite ferrofluid

For maghemite-citrate and magnetite-citrate ferrofluid, DLS measurements were taken and resulted in the Figure 71 and 72. Both ferrofluids showed a size distribution in a comparable range but several measurements of the magnetite-citrate ferrofluid showed more polydispersity, whereas the maghemite-citrate ferrofluid showed consistency in the DLS measurement from which a single size distribution was taken in the results. In addition, the correlogram of the maghemite-citrate ferrofluid indicated a curve for small particles, whereas the correlogram of the magnetite-citrate ferrofluid became broader which showed the presence of polydispersion. An explanation is the absence of a salt that selectively sediment larger particles in the magnetite-citrate ferrofluid which was applied for the maghemite-citrate ferrofluid.

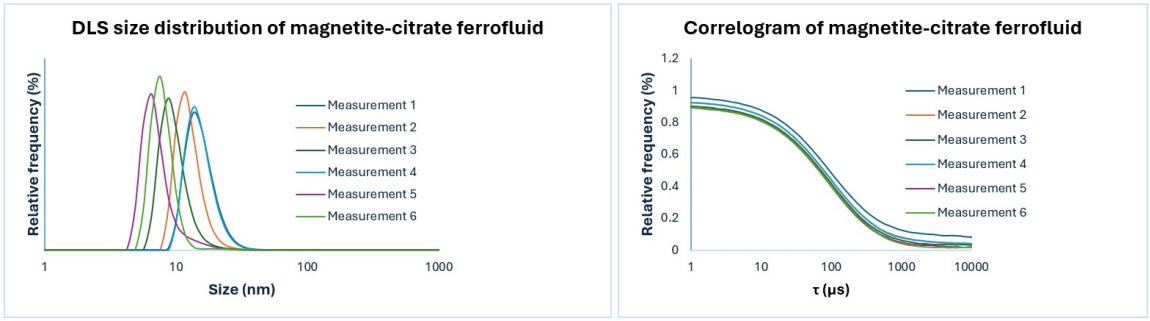

Figure 71: DLS measurement of magnetite-citrate ferrofluid (number distributed).

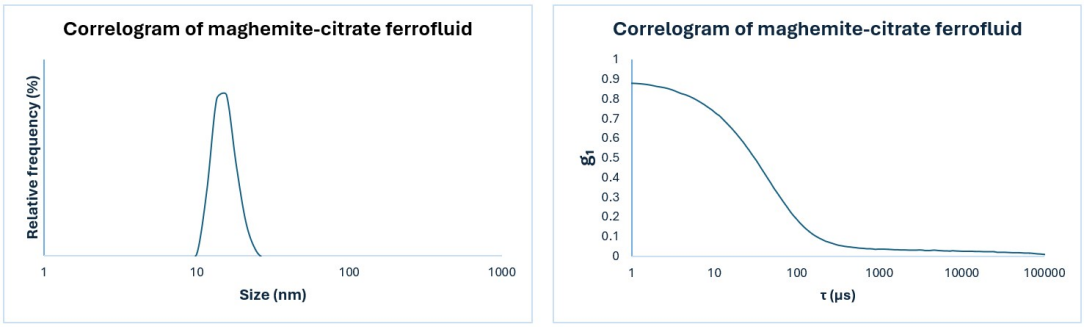

Figure 72: DLS measurement of maghemite-citrate ferrofluid (number distributed).

Since no TEM images were taken for maghemite-citrate and magnetite-citrate ferrofluids, magnetometry was used as a complementary technique to compare the obtained size distribution with the DLS measurements.

4.3 Magnetometry

4.3.1 Magnetite-citrate and maghemite-citrate ferrofluid

The magnetization curves of magnetite-citrate and maghemite-citrate ferrofluid are shown in Figure 73. The black and the red curves indicate the duplo measurements of the samples from the same batch. It was expected that the size distribution of the magnetometry were smaller than the DLS measurement since magnetometry only considered the size of the magnetic part, whereas DLS measured the hydrodynamic size. An explanation is the possible formation of agglomerations that contribute as a single large magnetic volume resulting in an increase of the size distribution. When comparing the magnetite-citrate ferrofluid with the maghemite-citrate ferrofluid, the size distribution of magnetite is broader than the size distribution of maghemite-citrate ferrofluid. The same results were observed from the DLS measurements. Therefore, the magnetometry indicated polydispersion of magnetite-citrate ferrofluid as well compared to maghemite-citrate ferrofluid that showed less polydispersity due to the smaller size distribution.

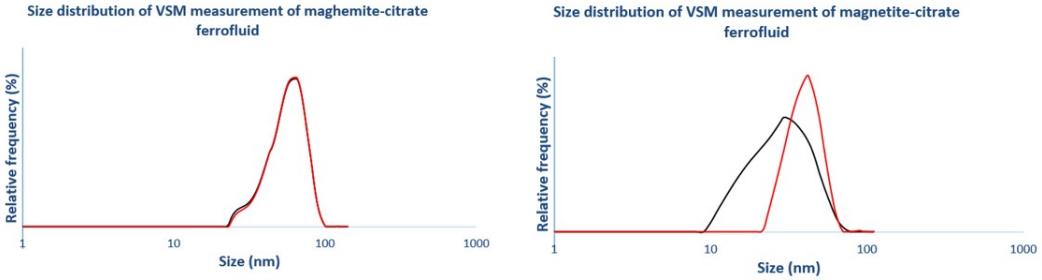

Figure 73: Size distribution of citrate ferrofluid using magnetometry. The black and red curve are duplo measurements from the same batch.

The corresponding magnetization curves of the citrate ferrofluids are shown in Figure 74. The magnetization curves of the citrate-ferrofluids showed superparamagnetic behaviour since the magnetization became strong in an external field, without any hysteresis. The magnetization curves of the maghemite-citrate ferrofluids was stronger than the magnetite-citrate ferrofluids even though the bulk magnetization of bulk magnetite is stronger than bulk maghemite theoretically. This appearance was explained by the difference in concentration since the concentration of the maghemite ferrofluid was higher than magnetite ferrofluid.

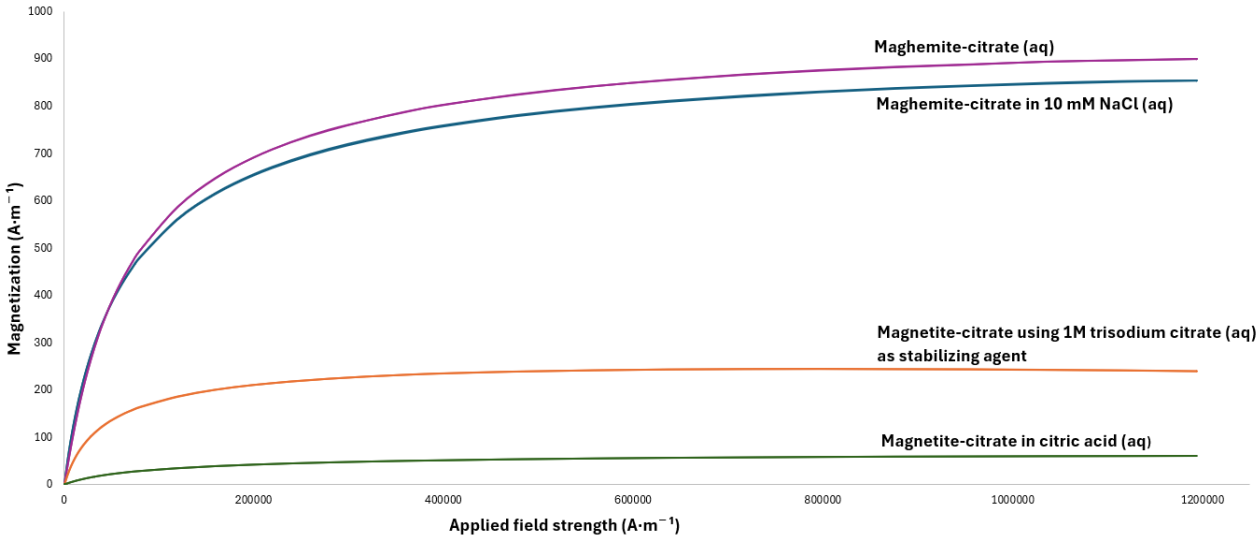

Figure 74: Magnetization curves of the citrate ferrofluids.

By normalizing the magnetization curves, comparisons between the citrate-ferrofluids were made as shown in Figure 75. The data points to form the magnetization curves were extracted from the computer program MINORIM[90]. The curves showed the magnetic strength of the sample as the magnetic dipole moment when altering the magnetic field strength. From the magnetic dipole moment, the magnetization was determined by applying Eq. 43 (next page). In addition, the saturation magnetization, M_{sat}, was determined using MINORIM and used to normalize the magnetization curves (M/Msat) as shown in Figure 75. As expected, Figure 75 showed the magnetization curve to be the strongest for magnetite using 1 M trisodium citrate (aq) as the stabilizing agent due to the higher bulk magnetization. In addition, the shape of the curve implied the presence of large magnetic volume of the magnetite particles using 1 M trisodium citrate (aq) as the stabilizing agent since the saturation magnetization was reached faster at lower applied magnetic field compared to the other citrate-ferrofluids. When observing the magnetization curve at 800 $kA \cdot m^{-1}$, a decrease in the magnetization curve was observed which indicated the presence of diamagnetic material. This diamagnetic contribution affected saturation magnetization and makes the magnetic strength of the magnetite particles using 1 M trisodium citrate (aq) as the stabilizing agent questionable compared to the other ferrimagnetic compounds. The comparable citrate-ferrofluids of the maghemite ferrofluid and magnetite ferrofluid in citric acid indicated a similar magnetic volume. The size distribution of DLS measurement showed similarities between the three citrate ferrofluids as well.

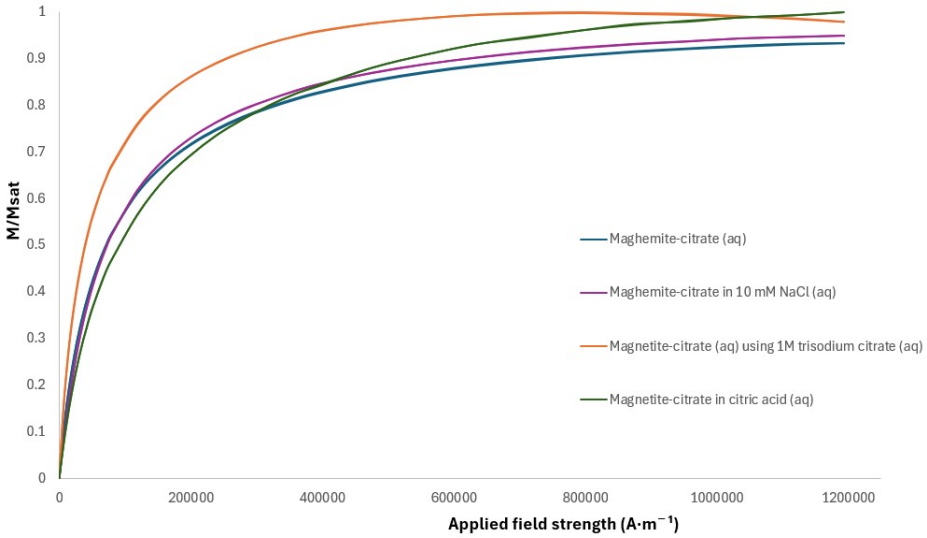

Figure 75: Normalized magnetization curves of the citrate ferrofluids.

$$M_x = \ m_{d,x} \cdot \frac{\rho_x}{m_x} \tag{43}$$

- M_x is the Magnetization of component x $(A \cdot m^{-1})$.
- $m_{d,x}$ is the dipole moment of component x $(A \cdot m^2)$.
- ρ_x is the density of component x $(kg \cdot m^{-3})$.
- m_x is the mass of component x (kg).

4.3.2 YIG ferrofluid

Figure 76 shows the magnetization of dried YIG-NPs before coating. The magnetization curves showed superparamagnetic behaviour since the magnetization became strong in an external field, without any hysteresis. The same approach of normalizing the magnetization curves was applied to compare the magnetization curves. As expected, the dried YIG dispersion with the strongest magnetization corresponded to the sample containing 2% YAG seeds and more reaction medium due to the presence of aggregates that acted as a combined magnetic volume and therefore enhanced the magnetization. The form of the curve also implied the presence of particles with a large magnetic volume since a low applied field strength was needed to obtain strong magnetization. The magnetization curve corresponded to 2 % YAG seeds showed a similar curve with the 2 % YAG seeds where more reaction medium was added regarding the form. The similar curve indicated the presence of particles with a large magnetic volume but the low magnetization showed that the applied concentration for the VSM analysis of 2 % YAG seeds was lower than for the applied concentration containing concentration which was lower for the 2 % YAG seeds containing more reaction medium.
The magnetization that corresponded to the 0.5 % YAG seeds was near the magnetization of containing 1 % YAG seeds indicating that the concentration and shape of YIG-NPs were similar. The small difference between the curves can be explained using the obtained TEM images. For the 1 % YAG seeds, particles with a large colloidal object size was observed whereas 0.5 % YAG seeds consisted mainly of small particles. An explanation is the possibility that a low number of large particles were present and detected with magnetometry that affected the magnetization curve but the large particles were not detected upon TEM analysis. The size distributions of the dried YIG-NPs are shown in Figure 77. The black and the red curves indicate the duplo measurements of the samples from the same batch. Only the sample containing 2 % YAG seeds met the expectations since the result corresponded with the TEM image.

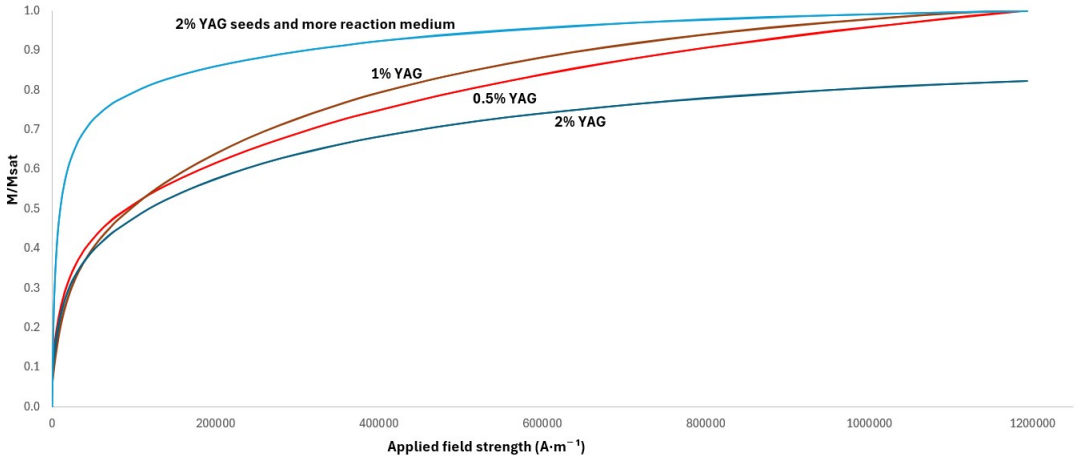

Figure 76: Normalized magnetization curves of the dried YIG-NPs before coating. The black and red curve are duplo measurements from the same batch.

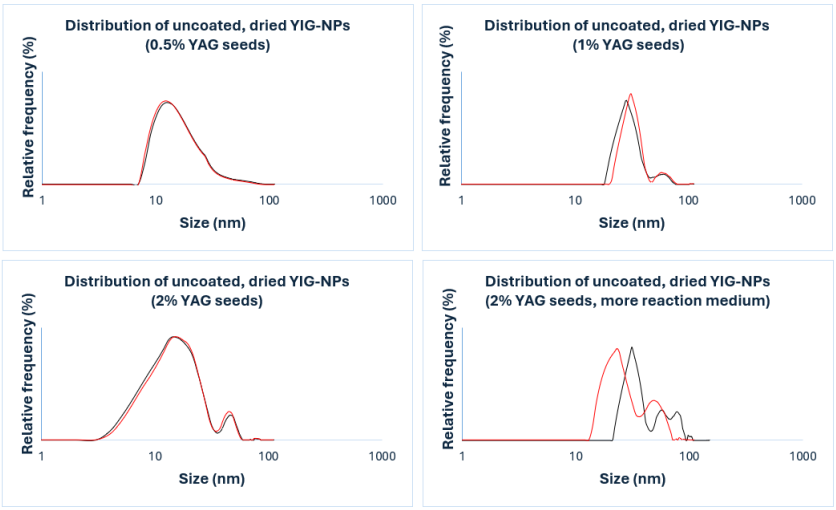

Figure 77: Size distributions of the dried YIG dispersions before coating.

Figure 78 and 79 show the magnetization curves of coated YIG ferrofluids using oleic acid as the stabilizing agent and cyclohexane and n-dodecane. The magnetization curves were different when comparing the YIG-NPs before and after coating. The difference of the magnetization curves were explained by the type of sample that were measured since the coated YIG-NPs were measured as dispersions and not as dry material. In addition, no correction of the diamagnetic contribution was taken for the dispersions which affected the magnetic strength and therefore the magnetization curves. In Figure 78, the curve corresponded to 2 % YAG seeds containing more reaction medium did show a decrease in magnetization which indicated the presence of non-magnetic materials (impurities from the solvothermal synthesis) and therefore affected the magnetization. Both curves showed the presence of magnetic particles with a large magnetic volume due to the observed steepness at low applied field strength but the difference in concentration altered the shape of the curve. Since the concentration of YIG-NPs in n-dodecane is lower, the dispersant affected the magnetization curve and as a result, the saturation magnetization of the YIG ferrofluid in n-dodecane was reached at higher magnetic field strength than the YIG ferrofluid in cyclohexane.
In Figure 79, the magnetization curves indicated no appearance of superparamagnetic behaviour since the magnetization became proportional with the applied magnetic field. The samples with a linear relation

showed paramagnetic behaviour. It was unlikely to observe paramagnetic behaviour of the curves since no data showed the consequences of an altered magnetization curve when coating was applied on YIG-NPs. An explanation for these results was the absence of YIG-NPs and therefore the possibility that another magnetic compound caused the paramagnetic appearance such as unreacted yttrium oxide regarding the solvothermal treatment.

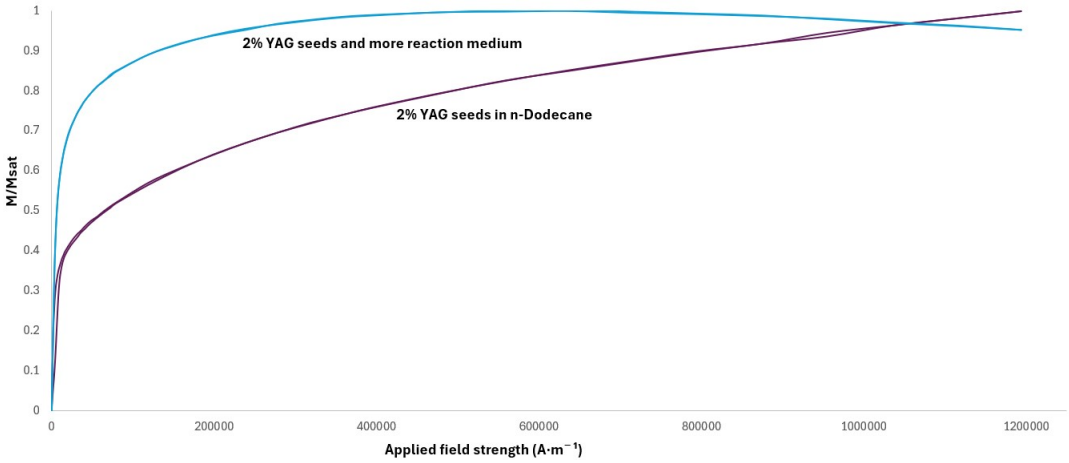

Figure 78: Normalized magnetization curves of the YIG-oleate ferrofluids after coating. 2 % YAG seeds containing more reaction was dispersed in cyclohexane.

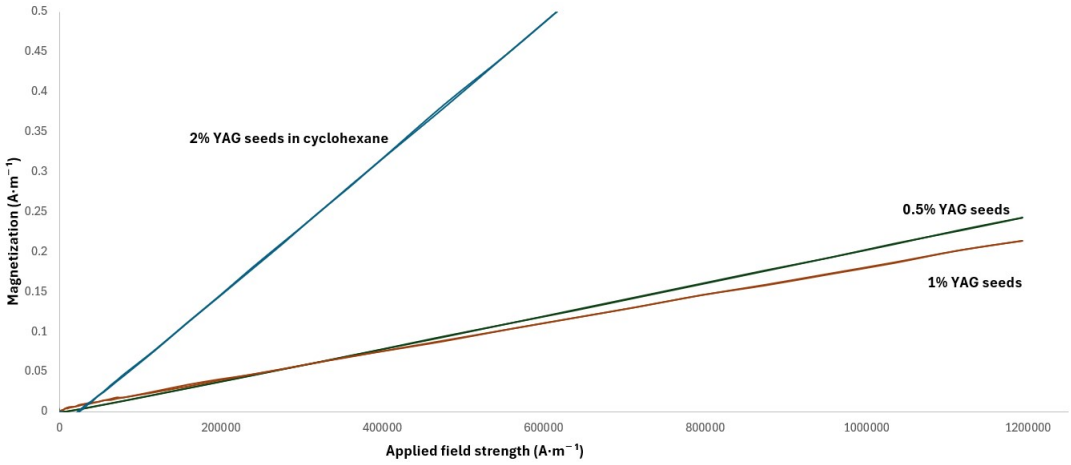

Figure 79: Magnetization curves of the YIG-oleate ferrofluids after coating. The YIG-NPs were dispersed in cyclohexane.

For the corresponding size distributions in Figure 80, the shape is altered in the width when comparing with the size distributions of the YIG-NPs. The fact that the coated YIG-NPs were measured as dispersion caused the distribution whereas the dried YIG-NPs were aggregated which resulted in a broader size distribution.

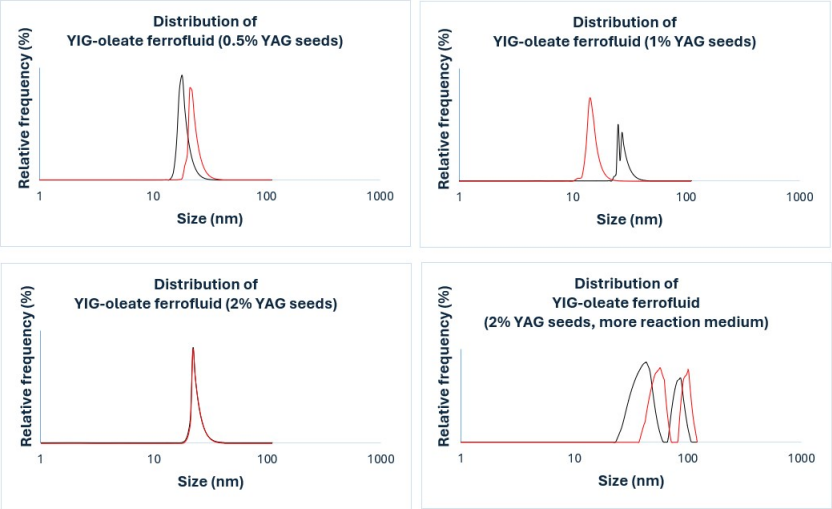

Figure 80: Size distributions of the YIG-oleate ferrofluids. The black and the red curves indicate the duplo measurements of the samples from the same batch.

Overall, the magnetization of the YIG-oleate ferrofluids are not in the same order of magnitude as the citrate-ferrofluids. The difference in order of magnitude was explained by the inconsistency upon the coating procedure of YIG-oleate ferrofluid. The volume of dispersant determined the magnetic behaviour of the ferrofluid but this step was considered by observation of the experiment meaning that there was no fixed dispersant volume involved to obtain the YIG-oleate ferrofluid.

4.4 UV-Vis spectroscopy: optical density of ferrofluids

The optical properties of the ferrofluids were investigated using UV-Vis measurements. The results are shown below for the spectra at the near-infrared range and a close-up at the wavelength range of 400 - 1000 nm. Fluctuations were observed at wavelengths lower than 400 nm for the YIG-oleate ferrofluid in oleic acid and the magnetite-citrate ferrofluid which was explained by the noise of the equipment. The optical density profiles higher than 400 nm showed a exponential decay and therefore agreed with the theory regarding the analysis technique except for the maghemite-citrate ferrofluid. Maghemite-citrate ferrofluid showed a exponential decay when 550 nm was exceeded. An explanation was the stability of the maghemite-citrate ferrofluid and the unaffected behaviour of the optical density in the specific wavelength range between 500-550 nm.
In addition, intersects were observed between the optical density profiles. These intersects denoted the similar, optical density of the ferrofluids at certain wavelengths. According to the literature, the specific wavelength at which the total optical density of the sample did not change during physical change of the sample was denoted as the isobestic point.[3] For magnetite and maghemite ferrofluid, the isobestic point was observed at 400 nm meaning that the ferrofluids absorbed equally strongly at 400 nm. The isobestic point of YIG ferrofluid was assumed to be the similar regarding the comparable optical properties but in Figure 81, no presence of isobestic points was observed at 400 nm since due to the difference in extinction coefficient indicating that the optical density of the ferrofluids is not similar. When comparing the YIG-oleate in cyclohexane with the coated YIG-NPs in oleic acid, a difference in optical density profile was observed and was explained by the desorption of the ligands from the magnetic particles when considering the desorption study.[91] The addition of more dispersant caused a disturbance in the ligand-nanoparticle stabilization. The oleate molecules have more affinity to the bulk phase and therefore resulted in detachment of the ligand.

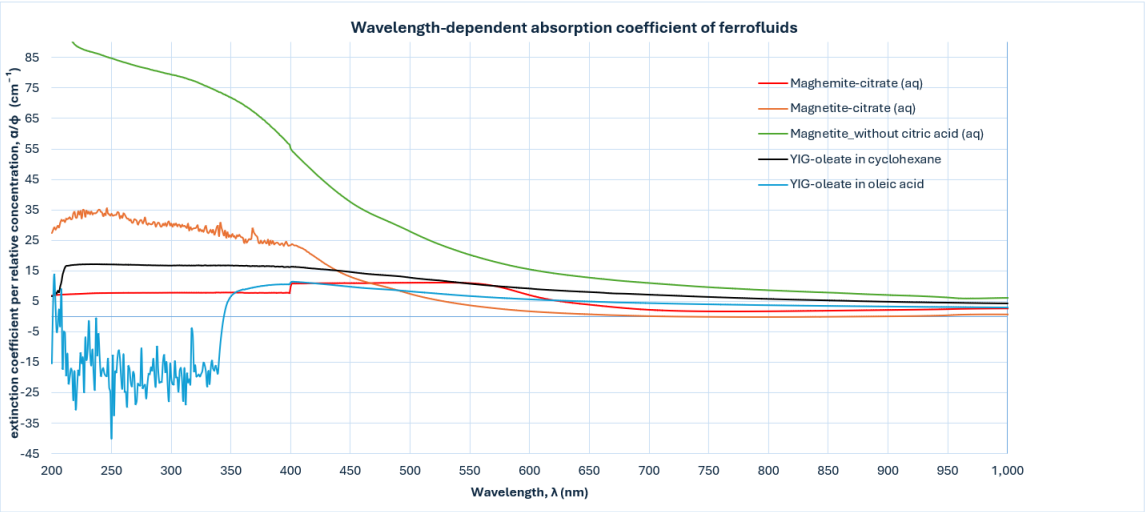

Figure 81: Wavelength-dependent extinction coefficient of ferrofluids. Wavelength-dependent absorption coefficient, α, divided by the relative concentration of the material (transmittance, $T = 10^{-\alpha x}$, with $x =$ optical path length of 1 cm).

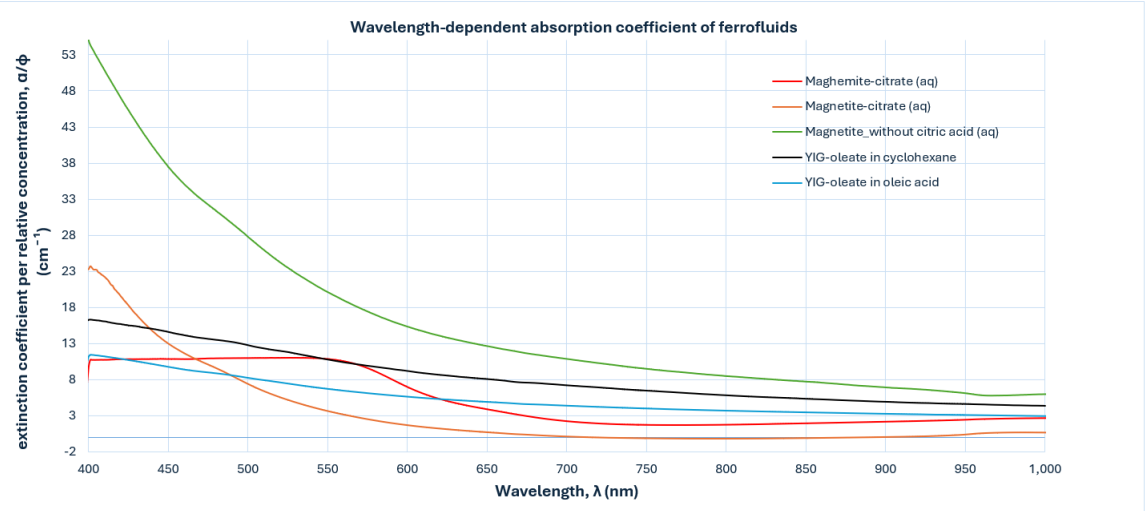

Figure 82: Wavelength-dependent extinction coefficient of ferrofluids (400-1000 nm). Wavelength-dependent absorption coefficient, α, divided by volume fraction of material (transmittance, $T = 10^{-\alpha x}$, with $x =$ optical path length of 1 cm).

When comparing the optical-density profiles with the absorption coefficient per volume fraction of maghemite and yttrium iron garnet in wavelength range from near infrared (NIR) to ultraviolet in 30 (also shown below as Figure 83), the measured optical absorption of the YIG ferrofluids did not agree with the lower optical behaviour and therefore, the transparency in the NIR was not achieved due to the higher optical absorbance profile of the YIG ferrofluid than magnetite and maghemite ferrofluid. This appearance was explained by the the failure of the coating that caused the presence of aggregates in the system and therefore increased the extinction of the YIG-ferrofluids regarding the scattering intensity.

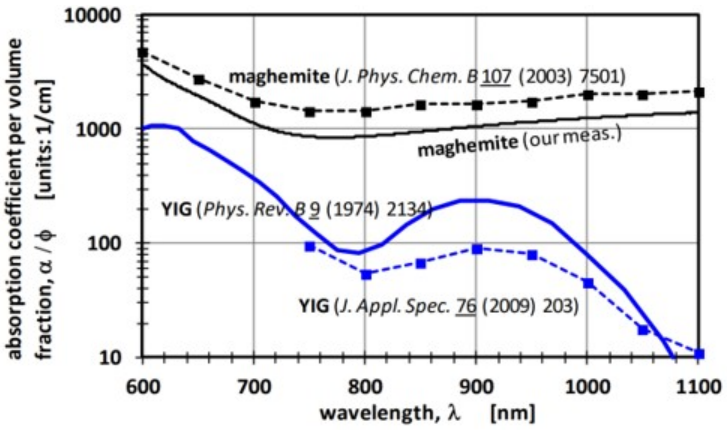

Figure 83: The absorption coefficient per volume fraction of maghemite and yttrium iron garnet in wavelength range from near infrared (NIR) to ultraviolet.[3, 4, 5, 54]

4.5 Magnetic sedimentation: Magnetophoresis of ferrofluids

4.5.1 Magnetite-citrate and maghemite-citrate ferrofluid

Snapshots of 1 mL of ferrofluid sample were taken in magnetic field by placing the cuvette containing the ferrofluid on the magnetic. Figure 84 shows the snapshots of the diluted maghemite ferrofluid in a cuvette with a factor of 10 at the initial time (A) and at a final time (B).

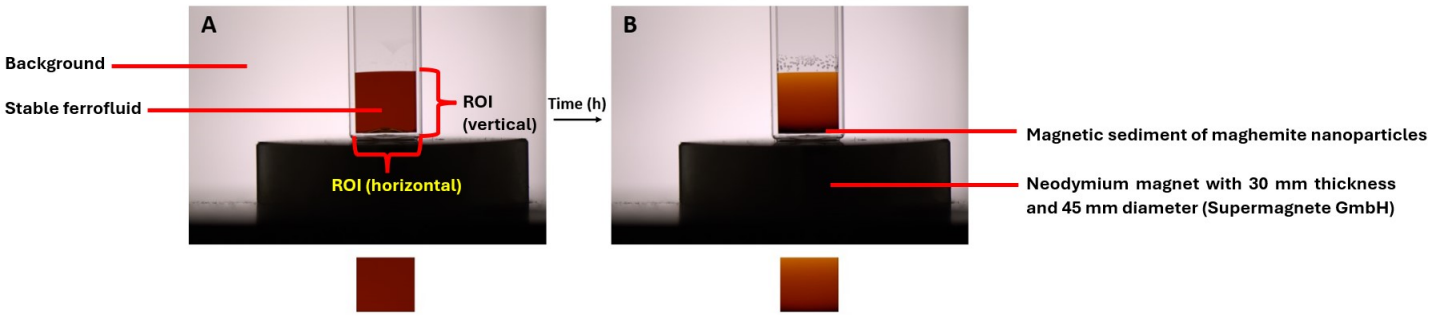

Figure 84: Snapshots of a cuvette containing maghemite ferrofluid in magnetic field at an initial time (A) and final time (B). The region of interest (ROI) is computed for analysing the magnetophoretic flow of the maghemite particles.

By capturing several images of the citrate-ferrofluid in the cuvette at a region of interest (ROI) selectively, Red-Green-Blue-values (RGB-values) were determined as represented in Figure 85. For the maghemite-citrate ferrofluid, a ROI of [[1062,1900](x-axis), [2635,3480]](y-axis) was taken to focus the measurements on the sample only and the irrelevant data which considered the ambient was left out.

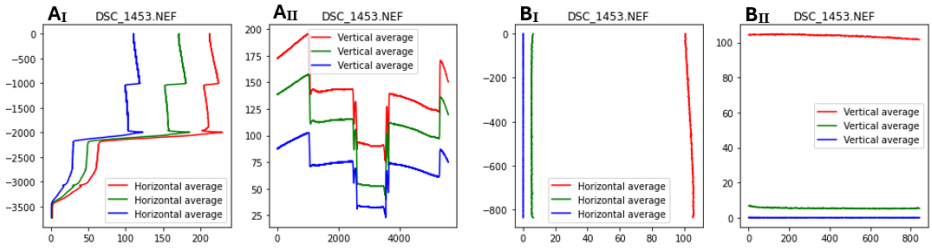

Figure 85: Horizontal (A_I) and vertical (A_{II}) average total overview and the Horizontal (B_I) and vertical (B_{II}) at ROI = [[1062,1900],[2635,3480]] for maghemite-citrate ferrofluid.

By computing the RGB-values at the chosen ROI, the time-dependent absorbance profiles were plotted for a specific channel height of 8 mm from which the magnetophoretic velocity profile was plotted. The average magnetophoretic velocity indicated the order of magnitude regarding the average particle size. The average particle size was determined by equalizing the magnetic force with the frictional force to obtain the expression as discussed in section 2.8 (Eq. 42). The results for the citrate ferrofluids are shown in Figure 86. The different color channel yielded different absorbance profiles due to the properties macroscopically. The formed maghemite-citrate ferrofluid was red in color. The absorbance for the red channel is therefore the most reasonable and the corresponding magnetophoretic velocity indicated a reasonable order of magnitude which was equal to a average diameter of 4.9 nm.

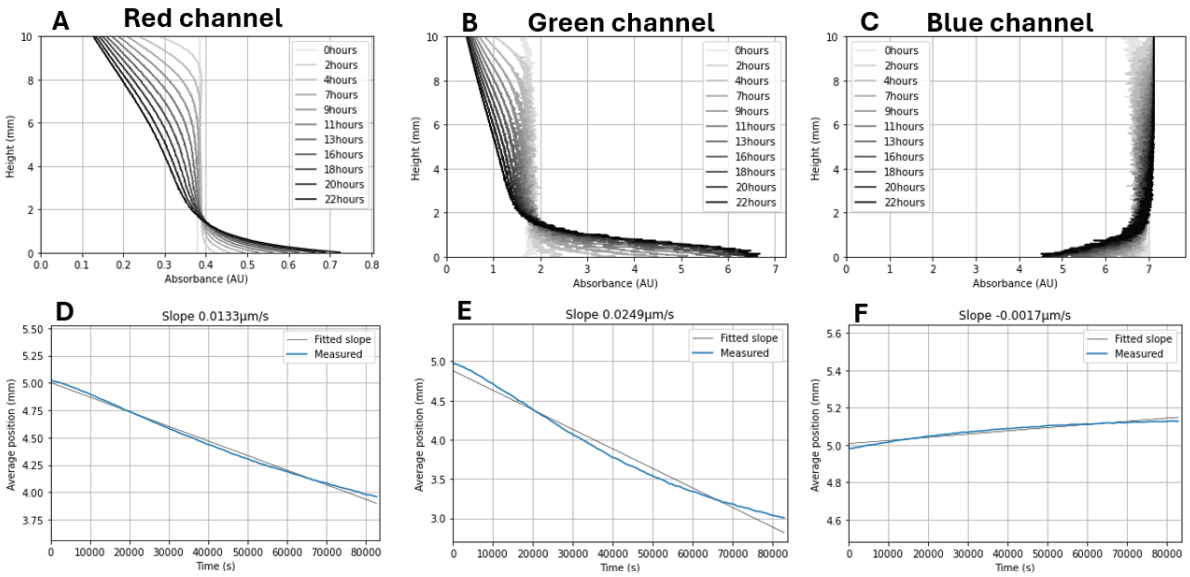

Figure 86: Time-dependent absorbance profile and the corresponding magnetophoretic velocity profiles for red, green and blue channel of maghemite-citrate ferrofluid from left to right.

The results that corresponded to the green channel showed deformation of the absorbance profile and the absorbance value was increased with one order of magnitude. The order of magnitude corresponded to an average particle size of 7.1 nm which was a reasonable value compared to the DLS analysis but the reliability of the data came into question regarding the linearity of the equipment (CCD camera) according to Zheng.[92] The results of the blue channel showed a flip of the absorbance profile and as a consequence yielded an average magnetophoretic velocity value from which the average particle could not be determined. That's why the CCD linearity of maghemite was plotted. Figure 87 shows the CCD linearity of the equipment. The plot showed if the concentrated-dependent profiles were in agreement with the law Lambert-Beer. The profiles

showed different intersection points with the y-axis and indicated the accuracy of the measurement where the intersect close to the origin behaves the law of Lambert-Beer. The accuracy of the CCD camera was therefore independent of the type of sample and its absorbance ability.

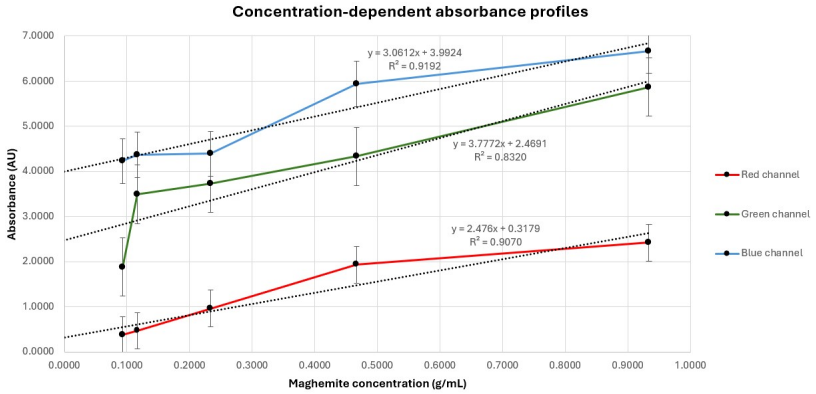

Figure 87: Measured absorbance vs. concentration for red, green and blue channels.

Magnetite-citrate ferrofluid was analyzed as well and showed a comparable magnetophoretic behaviour as maghemite-citrate ferrofluid. In Figure 88, the time-dependent absorbance profiles of magnetite showed reliable results for the red and green channel due to the reasonable absorbance values (less than 1). The profile of the blue channel was one order of magnitude higher and showed no distinction between the profiles at certain time intervals. Like for the results of maghemite-citrate ferrofluid, an explanation was the light environment that affected the sample at a prolonged exposure time.

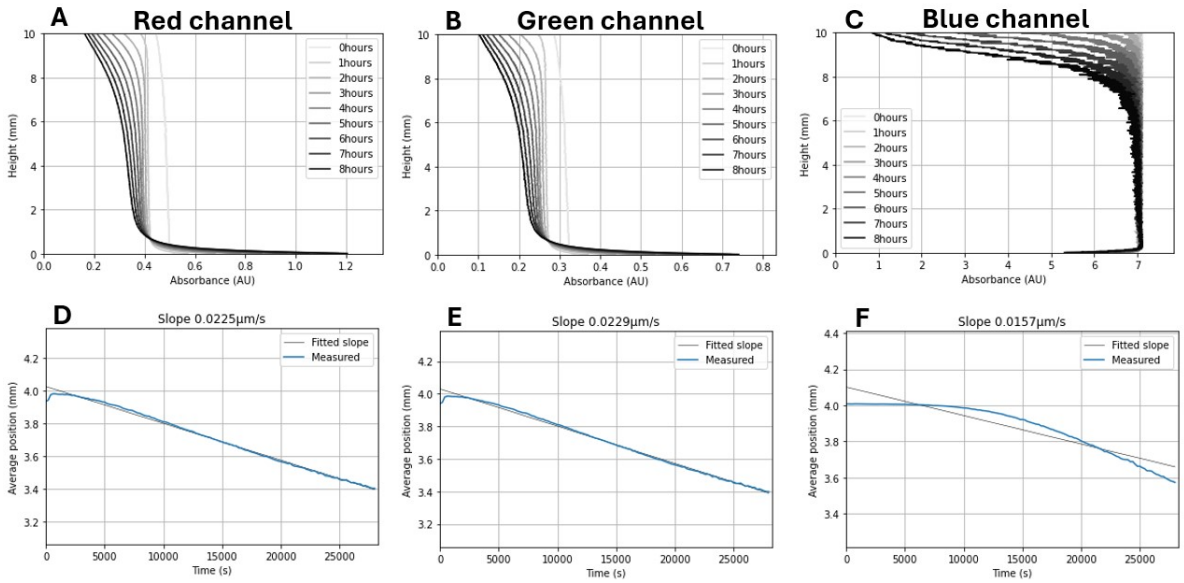

Figure 88: Time-dependent absorbance profile and the corresponding magnetophoretic velocity profiles for red, green and blue channel of magnetite-citrate ferrofluid from left to right.

4.5.2 YIG-oleate ferrofluid

YIG-oleate ferrofluids were observed in their time-dependent absorbance profile. The magnetophoretic behaviour of the oleate ferrofluids showed a higher migration rate compared to the citrate-ferrofluids and was explained due to the stability of the oleate ferrofluid. The insufficient coating and so the presence of

aggregates increased the migration rate and resulted in a decreased absorbance profile at a smaller time interval than the citrate-ferrofluids. As for the oleate-ferrofluid, the absorbance values are reliable for the red and green channel. For the blue channel the data is unreliable due to the absorbance values and rough appearance of the profile. In addition, the irregular appearance of the magnetophoretic velocity plots did not make the determination of the average particle size. An explanation for the positive slopes near 200 seconds indicated the presence of non-magnetic compounds that, due to the diamagnetic behaviour, opposes the external field and flow in opposite direction. This interrupted the migration of the magnetic particles and led to a combined velocity profile where migration took place before 200 seconds but some magnetic nanoparticles were blocked by diamagnetic compounds. By altering the position of the fit-slope to the time interval were magnetic migration occurred, an order of magnitude was determined 89 but as expected indicated the presence of aggregates due to the steep slope. The average particle size of the red, green and blue channel corresponded to 152, 180 and 224 nm, respectively.

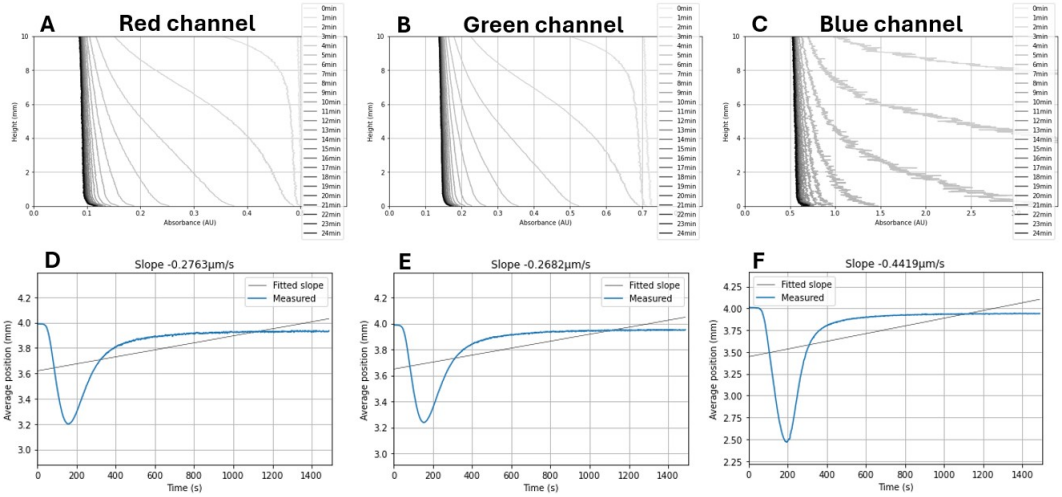

Figure 89: Time-dependent absorbance profile and the corresponding magnetophoretic velocity profiles for red, green and blue channel of YIG-oleate ferrofluid from left to right.

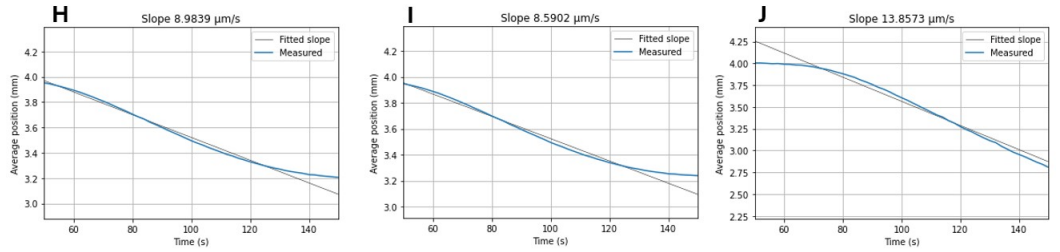

Figure 90: Corrected magnetophoretic velocity profiles for red, green and blue channel of YIG-oleate ferrofluid from left to right.

Furthermore, the stability of the ferrofluid and the influence of scattering light was explained by the optical density measurements of the ferrofluid at different concentrations and was corrected for the dilution. Figure 91 shows the wavelength-dependent optical density profiles at different dilution factors. The Figure showed differences in profiles when the maghemite was diluted with a factor of 100 and was explained by the decreased number concentration which was related to the osmotic pressure gradient using Van 't Hoff law (Eq. 5) and the expression that relates Brownian motion and diffusion (Eq. 7). A decrease in the number concentration lowers the osmotic pressure gradient and therefore limited the diffusion of the maghemite nanoparticles. Magnetic interactions between the nanoparticles dominated the behaviour of the maghemite ferrofluid and

resulted in aggregation indicating that the stability affected the optical density measurements in the presence due to the presence of scattering light.

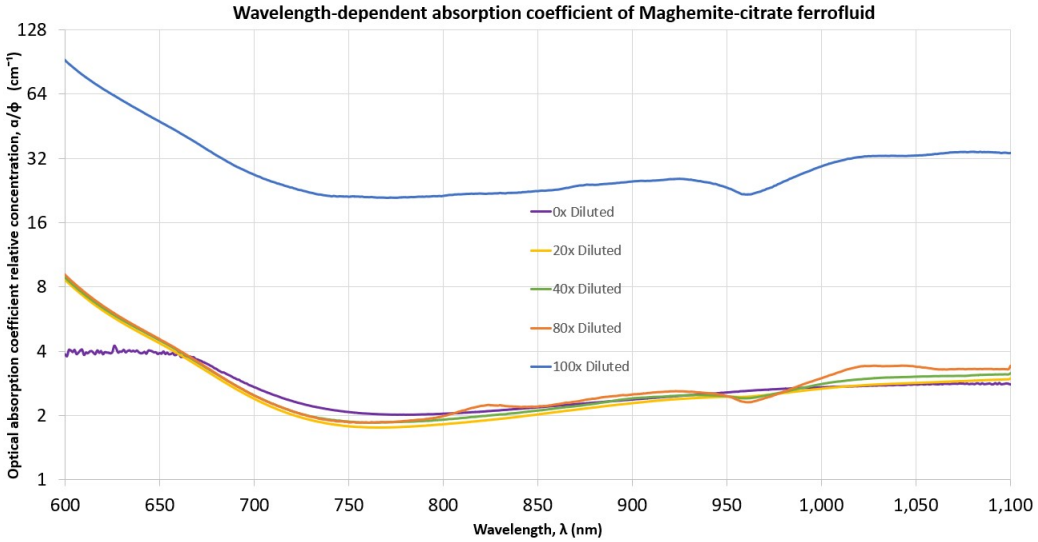

Figure 91: Wavelength-dependent optical density profiles at different dilution factors. Wavelength-dependent absorption coefficient, α, divided by the relative concentration of the material (transmittance, $T = 10^{-\alpha x}$, with x = optical path length of 1 cm).

5 Conclusion

YIG nanoparticles on YAG seeds have been made via the autoclave method, in a certain solvent at a certain temperature. Size control was not achieved since the YAG seeds turned out to be unexpectedly difficult to obtain the desired, small particles of YAG seeds, for which there are certain possible causes and certain approaches have been taken as a remedy. YIG on YAG was created, but these particles were also highly aggregated and no size control was feasible. With loosening by sonication and certain chemical post-treatment, the colloidal stability has been significantly improved, although the exceptionally high stability of conventional ferrofluids has not yet been achieved. This is because the particles were still too close together and/or too large. The stabilization part of the maghemite ferrofluid synthesis was not applicable to obtain stable YIG and magnetite ferrofluid in the water phase. A coating procedure was formed to obtain YIG-ferrofluid in the oil phase. The addition of citric acid as stabilizing agent showed improvement of the stability for magnetite ferrofluid. Optical transmission was not improved by making YIG, probably due to optical scattering by large aggregates seen by DLS and magnetic sedimentation. The characterization techniques clarified the stability of ferrofluids to be explained by the presence of aggregates.

6 Outlook

Since it appears difficult to make dispersions of YIG nanoparticles with good colloidal stability, which has probably not yet led to better transparency than maghemite dispersions, it is recommended that future research be limited to maghemite dispersions illuminated with NIR light. This probably has the advantage that it has demonstrably worked the best so far, while achieving even better results with YIG seems uncertain. If synthesis of YIG nanoparticles is continued, it is recommended to focus on the synthesis with 2% YAG seeds due to the high probability of obtaining a stable ferrofluid. Different surface modification methods can applied by considering the choice of dispersant and stabilizing agent. In addition, it is recommended to remove the centrifuge step. Instead, perform the coating procedure since the washing steps using a handheld magnet should be sufficient to separate the magnetic particles from the impurities. For the magnetic sedimentation experiment, it is recommended to construct a cuvette holder to position the cuvette at the same spot. This improves the accuracy of the measurements and makes it possible to capture pictures of a cuvette containing the solvent only as the blank measurements.

7 Acknowledgements

I would like to thank my supervisors Alex and Ben for overseeing my thesis. They gave me the responsibility to work on my project and their experience helped me a lot developing my research skills on academic level. I appreciated their feedback during our meetings and they showed me how I could approach the practical challenges from a different perspective. Of course, there are many steps to go for what I want to become, but their guidance will be noted for the challenges I will be facing in the future. In addition, I would like to thank the master students who attended the weekly RVV (Rendez-Vous du Vendredi) meetings for their input. Sam Bastiaan, Bram Bemelmans and Tijs Bitter, it was great to receive your thoughts on my research and these thoughts were taken in my research process as well.
Finally, I would like to thank my fellow master students for giving me a unforgettable time that variates in the nice discussions we have had while enjoying deliciously baked cookies and some funny quotes in between. These students Alex Nijland, Ffion Steenvoorden, Anouk van der Meer, Suzan de Vocht, Rogier van den Bosch, Michelle de Dood, Cas Jansen, Luuk Schoenmakers, Lisa Eij, Romy van den Heuvel, Maira Kim and Ariane Berthet gave me a memorable time to cherish. I wish everyone the best of luck in their research process. I could not have done my personal development without the support of the PCC group (Physical & Colloid Chemistry). Therefore, my gratitude to everyone with whom I have experienced the nice work environment in my thesis time.

8 References

[1] R. E. Rosensweig, "Magnetic fluids," *Scientific American*, vol. 247, no. 4, pp. 136–145, 1982.

[2] A. M. Van Silfhout, H. Engelkamp, and B. H. Erné, "Magnetic sedimentation velocities and equilibria in dilute aqueous ferrofluids," *The Journal of Physical Chemistry B*, vol. 124, no. 36, pp. 7989–7998, 2020.

[3] J. Tang, M. Myers, K. A. Bosnick, and L. E. Brus, "Magnetite fe3o4 nanocrystals: spectroscopic observation of aqueous oxidation kinetics," *The Journal of Physical Chemistry B*, vol. 107, no. 30, pp. 7501–7506, 2003.

[4] S. Wemple, S. Blank, J. Seman, and W. Biolsi, "Optical properties of epitaxial iron garnet thin films," *Physical Review B*, vol. 9, no. 5, p. 2134, 1974.

[5] V. Sobol, T. Volchik, S. Arabei, B. Korzun, and N. Kalanda, "Optical constants of yttrium–iron garnet single-crystal film structures," *Journal of Applied Spectroscopy*, vol. 76, pp. 203–208, 2009.

[6] J. Rongjin, Y. Wenhui, F. Caixiang, and Z. Yanwei, "Glycothermal synthesis of heavily ce-doped yig nanocrystals and their microstructures and magnetic properties," *J. Mater. Chem. C*, vol. 1, pp. 1763–1770, 2013.

[7] L. B. Kong, L. Liu, Z. Yang, S. Li, T. Zhang, and C. Wang, "Theory of ferrimagnetism and ferrimagnetic metal oxides," in *Magnetic, Ferroelectric, and Multiferroic Metal Oxides*, pp. 287–311, Elsevier, 2018.

[8] P. Zhao, D. Tang, J. Xie, and C. Zhang, "Magnetism and magnetic materials," in *Magnetic Levitation: Innovation of Density-Based Applications*, pp. 1–15, Springer, 2024.

[9] B. Erné, "Magnetometry," in *Colloidal Analysis Techniques, lecture notes*, pp. 144–158, Utrecht University, 2023.

[10] S. Palagummi and F.-G. Yuan, "Magnetic levitation and its application for low frequency vibration energy harvesting," in *Structural Health Monitoring (SHM) in Aerospace Structures*, pp. 213–251, Elsevier, 2016.

[11] V. Iacovacci, G. Lucarini, L. Ricotti, A. Menciassi, *et al.*, "Magnetic field-based technologies for lab-on-a-chip applications," *Lab-on-a-Chip Fabrication and Application*, pp. 1–56, 2016.

[12] Z. Liu, H. Wu, W. Ren, and Z.-G. Ye, "4.05 - piezoelectric and ferroelectric materials: Fundamentals, recent progress, and applications," in *Comprehensive Inorganic Chemistry III (Third Edition)* (J. Reedijk and K. R. Poeppelmeier, eds.), pp. 135–171, Oxford: Elsevier, third edition ed., 2023.

[13] V. Reichel and D. Faivre, *Magnetite Nucleation and Growth*, pp. 275–291. Cham: Springer International Publishing, 2017.

[14] M. A. Musa, R. S. Azis, N. H. Osman, J. Hassan, and T. Zangina, "Structural and magnetic properties of yttrium iron garnet (yig) and yttrium aluminum iron garnet (yalg) nanoferrite via sol-gel synthesis," *Results in Physics*, vol. 7, pp. 1135–1142, 2017.

[15] A. Z. Arsad, A. W. M. Zuhdi, N. B. Ibrahim, and M. A. Hannan, "Recent advances in yttrium iron garnet films: Methodologies, characterization, properties, applications, and bibliometric analysis for future research directions," *Applied Sciences*, vol. 13, no. 2, pp. 1–36, 2023.

[16] W. F. F. W. Ali, M. Othman, M. F. Ain, N. S. Abdullah, and Z. A. Ahmad, "Studies on the formation of yttrium iron garnet (yig) through stoichiometry modification prepared by conventional solid-state method," *Journal of the European Ceramic Society*, vol. 33, no. 7, pp. 1317–1324, 2013.

[17] V. Marghussian, "4 - magnetic properties of nano-glass ceramics," in *Nano-Glass Ceramics* (V. Marghussian, ed.), pp. 181–223, Oxford: William Andrew Publishing, 2015.

[18] M. Mehrmohammadi, K. Yoon, M. Qu, K. Johnston, and S. Emelianov, "Enhanced pulsed magnetomotive ultrasound imaging using superparamagnetic nanoclusters," *Nanotechnology*, vol. 22, no. 4, p. 045502, 2010.

[19] N. Sezer, İ. Arı, Y. Bicer, and M. Koc, "Superparamagnetic nanoarchitectures: Multimodal functionalities and applications," *Journal of Magnetism and Magnetic Materials*, vol. 538, p. 168300, 2021.

[20] D. Jiles, *Introduction to magnetism and magnetic materials*. CRC press, 2015.

[21] R. E. Rosensweig, "Magnetic fluids," *Annual review of fluid mechanics*, vol. 19, no. 1, pp. 437–461, 1987.

[22] T. A. Franklin, *Ferrofluid flow phenomena*. PhD thesis, Massachusetts Institute of Technology, 2003.

[23] B. Luigjes, D. M. E. Thies-Weesie, B. H. Erné, and A. P. Philipse, "Sedimentation equilibria of ferrofluids: Ii. experimental osmotic equations of state of magnetite colloids," *Journal of Physics: Condensed Matter*, vol. 24, p. 245104, May 2012.

[24] S. Laurent, D. Forge, M. Port, A. Roch, C. Robic, L. Vander Elst, and R. Muller, "Magnetic iron oxide nanoparticles: Synthesis, stabilization, vectorization, physicochemical characterizations, and biological applications," *Chemical reviews*, vol. 110, 07 2009.

[25] O. Oehlsen, S. I. Cervantes-Ramírez, P. Cervantes-Avilés, and I. A. Medina-Velo, "Approaches on ferrofluid synthesis and applications: current status and future perspectives," *ACS omega*, vol. 7, no. 4, pp. 3134–3150, 2022.

[26] M. Stoia, R. Istratie, and C. Păcurariu, "Investigation of magnetite nanoparticles stability in air by thermal analysis and FTIR spectroscopy," *Journal of Thermal Analysis and Calorimetry*, vol. 125, pp. 1185–1198, 2016.

[27] A. R. Trifoi, E. Matei, M. Râpă, A.-C. Berbecaru, C. Panaitescu, I. Banu, and R. Doukeh, "Coprecipitation nanoarchitectonics for the synthesis of magnetite: A review of mechanism and characterization," *Reaction Kinetics, Mechanisms and Catalysis*, vol. 136, no. 6, pp. 2835–2874, 2023.

[28] J. Winsett, A. Moilanen, K. Paudel, S. Kamali, K. Ding, W. Cribb, D. Seifu, and S. Neupane, "Quantitative determination of magnetite and maghemite in iron oxide nanoparticles using mössbauer spectroscopy," *SN Applied Sciences*, vol. 1, pp. 1–8, 2019.

[29] G. Gnanaprakash, S. Mahadevan, T. Jayakumar, P. Kalyanasundaram, J. Philip, and B. Raj, "Effect of initial ph and temperature of iron salt solutions on formation of magnetite nanoparticles," *Materials Chemistry and Physics*, vol. 103, no. 1, pp. 168–175, 2007.

[30] C. Blanco-Andujar, D. Ortega, Q. A. Pankhurst, and N. T. K. Thanh, "Elucidating the morphological and structural evolution of iron oxide nanoparticles formed by sodium carbonate in aqueous medium," *Journal of Materials Chemistry*, vol. 22, no. 25, pp. 12498–12506, 2012.

[31] J.-P. Jolivet, C. Froidefond, A. Pottier, C. Chanéac, S. Cassaignon, E. Tronc, and P. Euzen, "Size tailoring of oxide nanoparticles by precipitation in aqueous medium. a semi-quantitative modelling," *J. Mater. Chem.*, vol. 14, pp. 3281–3288, 2004.

[32] F. Yazdani and M. Seddigh, "Magnetite nanoparticles synthesized by co-precipitation method: The effects of various iron anions on specifications," *Materials chemistry and physics*, vol. 184, pp. 318–323, 2016.

[33] T. Iwasaki, N. Mizutani, S. Watano, T. Yanagida, and T. Kawai, "Size control of magnetite nanoparticles by organic solvent-free chemical coprecipitation at room temperature," *Journal of Experimental Nanoscience*, vol. 5, no. 3, pp. 251–262, 2010.

[34] A. Abedini, A. R. Daud, M. A. Abdul Hamid, and N. Kamil Othman, "Radiolytic formation of fe3o4 nanoparticles: influence of radiation dose on structure and magnetic properties," *PLoS One*, vol. 9, no. 3, p. e90055, 2014.

[35] S. Ebnesajjad, "4 - surface and material characterization techniques," in *Surface Treatment of Materials for Adhesion Bonding* (S. Ebnesajjad, ed.), pp. 43–75, Norwich, NY: William Andrew Publishing, 2006.

[36] I. Nurdin, Ridwan., and Satrianananda, "The effect of temperature on synthesis and stability of superparamagnetic maghemite nanoparticles suspension," *Journal of Materials Science and Chemical Engineering*, vol. 4, pp. 35–41, 2016.

[37] G. Zhao, X. Zhang, and F. Morvan, "Theory for the coercivity and its mechanisms in nanostructured permanent magnetic materials," *Reviews in Nanoscience and Nanotechnology*, vol. 4, no. 1, pp. 1–25, 2015.

[38] S. Singamaneni, V. N. Bliznyuk, C. Binek, and E. Y. Tsymbal, "Magnetic nanoparticles: recent advances in synthesis, self-assembly and applications," *Journal of Materials Chemistry*, vol. 21, no. 42, pp. 16819–16845, 2011.

[39] A. Akbarzadeh, M. Samiei, and S. Davaran, "Magnetic nanoparticles: preparation, physical properties, and applications in biomedicine," *Nanoscale research letters*, vol. 7, pp. 1–13, 2012.

[40] A. O. Ivanov and A. Zubarev, "Chain formation and phase separation in ferrofluids: The influence on viscous properties," *Materials*, vol. 13, no. 18, p. 3956, 2020.

[41] M. Klokkenburg, R. P. A. Dullens, W. K. Kegel, B. H. Erné, and A. P. Philipse, "Quantitative real-space analysis of self-assembled structures of magnetic dipolar colloids," *Phys. Rev. Lett.*, vol. 96, p. 037203, Jan 2006.

[42] M. Klokkenburg, B. H. Erné, J. D. Meeldijk, A. Wiedenmann, A. V. Petukhov, R. P. A. Dullens, and A. P. Philipse, "In situ imaging of field-induced hexagonal columns in magnetite ferrofluids," *Phys. Rev. Lett.*, vol. 97, p. 185702, Nov 2006.

[43] Y. Wu, D. Wang, and Y. Li, "Understanding of the major reactions in solution synthesis of functional nanomaterials," *Sci. China Mater*, vol. 59, no. 11, pp. 938–996, 2016.

[44] S. Karthika, T. Radhakrishnan, and P. Kalaichelvi, "A review of classical and nonclassical nucleation theories," *Crystal Growth & Design*, vol. 16, no. 11, pp. 6663–6681, 2016.

[45] Y. Xia, Y. Xiong, B. Lim, and S. E. Skrabalak, "Shape-controlled synthesis of metal nanocrystals: simple chemistry meets complex physics?," *Angewandte Chemie International Edition*, vol. 48, no. 1, pp. 60–103, 2009.

[46] K. Sudhakar, N. N. Reddy, T. Jayaramudu, J. Jayaramudu, A. B. Reddy, B. Manjula, and E. R. Sadiku, "Aerogels and foamed nanostructured polymer blends," in *Design and Applications of Nanostructured Polymer Blends and Nanocomposite Systems*, pp. 75–99, Elsevier, 2016.

[47] M. Inoue, "Glycothermal synthesis of metal oxides," *Journal of Physics: Condensed Matter*, vol. 16, p. S1291, march 2004.

[48] E. Edinach, D. Kramushchenko, A. Gurin, Y. A. Uspenskaya, R. Babunts, H. Asatryan, A. Badalyan, N. Romanov, and P. Baranov, "Evidence of the excitation of mn 2+ spin-dependent photoluminescence in manganese-doped yttrium aluminum garnets," *Applied Magnetic Resonance*, vol. 50, pp. 1315–1324, 2019.

[49] V. M. Masalov, N. S. Sukhinina, E. A. Kudrenko, and G. A. Emelchenko, "Mechanism of formation and nanostructure of stöber silica particles," *Nanotechnology*, vol. 22, p. 275718, may 2011.

[50] M. Inoue, H. Kominami, and T. Inui, "Reaction of aluminium alkoxides with various glycols and the layer structure of their products," *J. Chem. Soc., Dalton Trans.*, pp. 3331–3336, 1991.

[51] M. Inoue, H. Kominami, and T. Inui, "Synthesis of large pore-size and large pore-volume aluminas by glycothermal treatment of aluminium alkoxide and subsequent calcination," *Journal of materials science*, vol. 29, pp. 2459–2466, 1994.

[52] N. Z., N. K., and I. Y., "Room temperature ferromagnetism in dilute iron-doped yttrium aluminum garnet polycrystals," *The Journal of Physical Chemistry C*, vol. 113, pp. 20044–20049, 10 2009.

[53] W. Fontijn, P. Van der Zaag, M. Devillers, V. Brabers, and R. Metselaar, "Optical and magneto-optical polar kerr spectra of Fe_3O_4 and Mg^{2+} or Al^{3+} substituted Fe_3O_4," *Physical Review B*, vol. 56, no. 9, p. 5432, 1997.

[54] E. Dubois, V. Cabuil, F. Boué, and R. Perzynski, "Structural analogy between aqueous and oily magnetic fluids," *The Journal of chemical physics*, vol. 111, no. 15, pp. 7147–7160, 1999.

[55] T. Overton, J. Rourke, and F. A. Armstrong, *Inorganic Chemistry*. Oxford University Press, 2018.

[56] W. Fontijn, P. Van der Zaag, L. Feiner, R. Metselaar, and M. Devillers, "A consistent interpretation of the magneto-optical spectra of spinel type ferrites," *Journal of Applied Physics*, vol. 85, no. 8, pp. 5100–5105, 1999.

[57] J. Chen, H.-S. Hsu, Y.-H. Huang, and D.-J. Huang, "Spin-dependent optical charge transfer in magnetite from transmitting optical magnetic circular dichroism," *Physical Review B*, vol. 98, no. 8, p. 085141, 2018.

[58] D. Wood and J. Remeika, "Effect of impurities on the optical properties of yttrium iron garnet," *Journal of Applied Physics*, vol. 38, no. 3, pp. 1038–1045, 1967.

[59] B. Gizhevskiĭ, Y. P. Sukhorukov, E. Gan'Shina, N. Loshkareva, A. Telegin, N. Lobachevskaya, V. Gaviko, and V. Pilyugin, "Optical and magneto-optical properties of nanostructured yttrium iron garnet," *Physics of the solid state*, vol. 51, pp. 1836–1842, 2009.

[60] A. Kumar, R. Kumar, N. Verma, A. Anupama, H. K. Choudhary, R. Philip, and B. Sahoo, "Effect of the band gap and the defect states present within band gap on the non-linear optical absorption behaviour of yttrium aluminium iron garnets," *Optical Materials*, vol. 108, p. 110163, 2020.

[61] C. Tang and Z. Yang, "Chapter 8 - transmission electron microscopy (tem)," in *Membrane Characterization* (N. Hilal, A. F. Ismail, T. Matsuura, and D. Oatley-Radcliffe, eds.), pp. 145–159, Elsevier, 2017.

[62] S. Amelinckx, D. Van Dyck, J. Van Landuyt, and G. van Tendeloo, *Electron microscopy: principles and fundamentals*. John Wiley & Sons, 2008.

[63] J. Stetefeld, S. A. McKenna, and T. R. Patel, "Dynamic light scattering: a practical guide and applications in biomedical sciences," *Biophysical reviews*, vol. 8, pp. 409–427, 2016.

[64] J. Lim, S. P. Yeap, H. X. Che, and S. C. Low, "Characterization of magnetic nanoparticle by dynamic light scattering," *Nanoscale research letters*, vol. 8, pp. 1–14, 2013.

[65] P. A. Hassan, S. Rana, and G. Verma, "Making sense of brownian motion: colloid characterization by dynamic light scattering," *Langmuir*, vol. 31, no. 1, pp. 3–12, 2015.

[66] M. R. Zamani Kouhpanji and B. J. Stadler, "A guideline for effectively synthesizing and characterizing magnetic nanoparticles for advancing nanobiotechnology: A review," *Sensors*, vol. 20, no. 9, p. 2554, 2020.

[67] J. F. Leary, *Characterizing Nanoparticles*, p. 122–142. Cambridge: Cambridge University Press, 2022.

[68] E. C. Devi and S. D. Singh, "Tracing the magnetization curves: a review on their importance, strategy, and outcomes," *Journal of Superconductivity and Novel Magnetism*, vol. 34, pp. 15–25, 2021.

[69] M. Frenea-Robin and J. Marchalot, "Basic principles and recent advances in magnetic cell separation," *Magnetochemistry*, vol. 8, no. 1, p. 11, 2022.

[70] A. Adeyeye and G. Shimon, "Chapter 1 - growth and characterization of magnetic thin film and nanostructures," in *Magnetism of Surfaces, Interfaces, and Nanoscale Materials* (R. E. Camley, Z. Celinski, and R. L. Stamps, eds.), vol. 5 of *Handbook of Surface Science*, pp. 1–41, North-Holland, 2015.

[71] N. Morton, "Induced electromotive forces," *European Journal of Physics*, vol. 5, p. 251, oct 1984.

[72] P. Kinsler, "Faraday's law and magnetic induction: Cause and effect," 2019.

[73] I. Waqar, Z. Azizi, P. Nikmal, R. Rafi, W. Ulfat, O. Abid, M. J. Niazi, and Z. Khan, "Comparison between electromotive force and electric potential difference," *Turkish Journal of Computer and Mathematics Education (TURCOMAT)*, vol. 14, no. 1, pp. 236–242, 2023.

[74] S. Foner, "Versatile and sensitive vibrating-sample magnetometer," *Review of Scientific Instruments*, vol. 30, no. 7, pp. 548–557, 1959.

[75] E. Liu, "Materials and designs of magnetic tunnel junctions with perpendicular magnetic anisotropy for high-density memory applications," 2018.

[76] I. Suryata, H. G. Svavarsson, S. Einarsson, Á. Brynjólfsdóttir, and G. Maliga, "Geothermal co2 biomitigation techniques by utilizing microalgae at the blue lagoon, iceland," in *Proceedings, 34th Workshop on Geothermal Reservoir Engineering. Stanford University, Stanford*, 2010.

[77] F. Cuppo, S. Gomez, and A. M. Figueiredo Neto, "Effect of the concentration of magnetic grains on the linear-optical-absorption coefficient of ferrofluid-doped lyotropic mesophases: Deviation from the beer-lambert law," *The European Physical Journal E*, vol. 13, pp. 327–333, 2004.

[78] A. Alekseev, E. Nepomnyashchaya, E. Velichko, and E. Shan, "The uv-vis transmission spectra of ferromagnetic fluids," in *International Youth Conference on Electronics, Telecommunications and Information Technologies: Proceedings of the YETI 2020, St. Petersburg, Russia*, pp. 327–334, Springer, 2021.

[79] Z. Said, M. Sajid, R. Saidur, G. Mahdiraji, and N. Rahim, "Evaluating the optical properties of tio2 nanofluid for a direct absorption solar collector," *Numerical Heat Transfer, Part A: Applications*, vol. 67, no. 9, pp. 1010–1027, 2015.

[80] A. Zekry, *properties of dielectric materials BY abdelhalim zekry*. 04 2019.

[81] M. I. Mishchenko, L. D. Travis, and A. A. Lacis, *Scattering, absorption, and emission of light by small particles*. Cambridge university press, 2002.

[82] C. F. Bohren and D. R. Huffman, *Absorption and scattering of light by small particles*. John Wiley & Sons, 2008.

[83] Z. Dogic, A. Philipse, S. Fraden, and J. Dhont, "Concentration-dependent sedimentation of colloidal rods," *The Journal of chemical physics*, vol. 113, no. 18, pp. 8368–8380, 2000.

[84] M. Odziomek, F. Chaput, F. Lerouge, C. Dujardin, M. Sitarz, S. Karpati, and S. Parola, "From nanoparticle assembly to monolithic aerogels of yag, rare earth fluorides, and composites," *Chemistry of Materials*, vol. 30, no. 15, pp. 5460–5467, 2018.

[85] W. Q. Wang Qiang, C. K. Chen KeFu, L. J. Li Jun, Y. G. Yang GuiHua, L. S. Liu ShanShan, and X. J. Xu Jun, "The solubility of lignin from bagasse in a 1, 4-butanediol/water system.," 2011.

[86] M. Sethu Raman, M. Kesavan, K. Senthilkumar, and V. Ponnuswamy, "Ultrasonic, dft and ft-ir studies on hydrogen bonding interactions in aqueous solutions of diethylene glycol," *Journal of Molecular Liquids*, vol. 202, pp. 115–124, 2015.

[87] M. Odziomek, F. Chaput, F. Lerouge, M. Sitarz, and S. Parola, "Highly luminescent yag: Ce ultra-small nanocrystals, from stable dispersions to thin films," *Journal of Materials Chemistry C*, vol. 5, no. 47, pp. 12561–12570, 2017.

[88] E. Mallmann, A. Sombra, J. Goes, and P. Fechine, "Yttrium iron garnet: properties and applications review," *Solid State Phenomena*, vol. 202, pp. 65–96, 2013.

[89] M. O. Besenhard, A. P. LaGrow, A. Hodzic, M. Kriechbaum, L. Panariello, G. Bais, K. Loizou, S. Damilos, M. M. Cruz, N. T. K. Thanh, *et al.*, "Co-precipitation synthesis of stable iron oxide nanoparticles with naoh: New insights and continuous production via flow chemistry," *Chemical Engineering Journal*, vol. 399, p. 125740, 2020.

[90] J. van Rijssel, B. W. Kuipers, and B. H. Erné, "Non-regularized inversion method from light scattering applied to ferrofluid magnetization curves for magnetic size distribution analysis," *Journal of Magnetism and Magnetic Materials*, vol. 353, pp. 110–115, 2014.

[91] M. Klokkenburg, J. Hilhorst, and B. Erné, "Surface analysis of magnetite nanoparticles in cyclohexane solutions of oleic acid and oleylamine," *Vibrational spectroscopy*, vol. 43, no. 1, pp. 243–248, 2007.

[92] Z. Li, X. Chen, L. Ren, J. Song, Y. Li, B. Zheng, and H. Liu, "Simultaneous dual-color fluorescence microscope: A characterization study," *Analytical Cellular Pathology*, vol. 36, no. 5-6, pp. 163–172, 2013.

9 Appendix

The documents are stored as hyperlink. When clicking the link, the documents can be viewed. Please note that when clicking the link, the current document disappears. In advance, the link can be selected and copied to open the relevant document in a new tab.

9.1 Synthesis

9.1.1 Protocol maghemite ferrofluid

URL: https://1drv.ms/b/s!AiVaGjkrCn_jiTbTUqJFHILmibfE?e=8SGuZx

9.1.2 Protocol magnetite ferrofluid

URL: https://1drv.ms/b/s!AiVaGjkrCn_jiTcMPkOLKDDoJ154?e=IHk9d2

9.1.3 Protocol YIG ferrofluid

URL: https://1drv.ms/b/s!AiVaGjkrCn_jiThGQDrisQ0W7gxw?e=AH26dB

9.1.3.1 Vacuum distillation Aluminium isopropoxide

URL: https://1drv.ms/b/s!AiVaGjkrCn_jiTk_sypyEXDaZJd9?e=QO8oG3

9.2 TEM and DLS

9.2.1 Protocol TEM preparation

URL: https://1drv.ms/b/s!AiVaGjkrCn_jiTokuWitLYVSzehh?e=wb65wS

9.2.2 TEM and DLS analysis of maghemite, magnetite, YAG and YIG dispersions

URL: https://1drv.ms/b/s!AiVaGjkrCn_jiTtLJYh-JIY019Rl?e=dsNvlK

9.3 Magnetometry

9.3.1 Protocol VSM preparation

URL: https://1drv.ms/b/s!AiVaGjkrCn_jiTzFWFVzhxBFfmqQ?e=9TsRjg

9.3.2 VSM analysis of maghemite, magnetite and YIG dispersions

URL: https://1drv.ms/b/s!AiVaGjkrCn_jiT3ai0lT9QbX85mc?e=hFEl9u

9.4 Magnetic sedimentation

9.4.1 Protocol data processing

URL: https://1drv.ms/b/s!AiVaGjkrCn_jiT4Ycs0hgU4SHryM?e=rHT0Zo

9.4.2 Analysis of ferrofluids

URL: https://1drv.ms/b/s!AiVaGjkrCn_jiT_uh-aHO902ECN3?e=Ab2wVW

9.5 UV-Vis spectroscopy

9.5.1 Optical density measurements of ferrofluids

URL: https://1drv.ms/b/s!AiVaGjkrCn_jiUBXRDCeCSEU-zpT?e=NNPho3